

UC Riverside

UC Riverside Electronic Theses and Dissertations

Title

Acoustic Phonons in Ultra-Wide-Band-Gap Semiconductors Investigated With Brillouin-Mandelstam Spectroscopy

Permalink

<https://escholarship.org/uc/item/1cv3r1hg>

Author

Guzman, Erick A

Publication Date

2024

Copyright Information

This work is made available under the terms of a Creative Commons Attribution-NonCommercial-ShareAlike License, available at <https://creativecommons.org/licenses/by-nc-sa/4.0/>

Peer reviewed|Thesis/dissertation

UNIVERSITY OF CALIFORNIA
RIVERSIDE

Acoustic Phonons in Ultra-Wide-Band-Gap Semiconductors Investigated
With Brillouin - Mandelstam Spectroscopy

A Dissertation submitted in partial satisfaction
of the requirements for the degree of

Doctor of Philosophy

in

Electrical Engineering

by

Erick A. Guzman

March 2025

Dissertation Committee:

Dr. Alexander Balandin, Co-Chairperson

Dr. Xi Chen, Co-Chairperson

Dr. Richard Wilson

Copyright by
Erick A. Guzman
2025

The Dissertation of Erick A. Guzman is approved:

Committee Co-Chairperson

Committee Co-Chairperson

University of California, Riverside

ACKNOWLEDGEMENTS

First and foremost, I would like to begin by thanking my doctoral advisor, Dr. Alexander A. Balandin for giving me the opportunity to join his lab back in the fall of 2020 and continue my journey through higher education. He showed me support, guidance, and patience through that uncertain time and throughout my time in the group, as I was able to let my curiosity for knowledge flourish freely. His insight and expertise was invaluable, and his influence shows in my research. His mentorship and guidance shaped how I conduct and present my research, allowed me to grow as a person, and opened many opportunities for the next step in my career and for that I am forever thankful.

Next, I would like to thank Dr. Fariborz Kargar who was the acting lab manager during my time at UCR. I was fortunate enough to follow in his footsteps and conduct research with his direct support. I worked closely with him throughout my time in the group and I learned a great deal about Brillouin spectroscopy and acoustic phonon phenomena. He always pushed me to put out excellent work and instilled in me a great work ethic. I am grateful for his expertise and mentorship.

Next I would like to thank all my group members from my time at UCR and as a UCLA affiliate: Dr. Zahra Bahrani, Dr. Subhajit Ghosh, Dr. Sriharsha Sudhindra, Dr. Tekwam Geremew, Dylan Wright, Maedah Taheri, Jordan Teeter, Jonas Brown, Zahra Ebrahim Nataj, Lokesh Ramesh, Xuke Fu, and Sashank Sriram. They are all extremely dedicated and I am lucky to have collaborated and learned from them as well.

I would also like to thank my master's thesis advisor Dr. Gang Lu who motivated me to learn and ask questions, and a very important collaborator from that time Dr. Mahesh Neupane. I interned with him at ARL for over a year, and that work was incorporated into my master's thesis. He motivated me to continue my education at a time when I was unsure about my future, and without his push I would not be where I am today.

Finally, I would like to acknowledge my family who showed me unwavering support not only during my time at UC Riverside, but throughout my education. Without their love and support my journey would have been much more difficult.

I would like to acknowledge the collaborators that made the work in this dissertation possible: Dr. Wilson's Group (UCR), refractive index measurements done by Frank Angeles; Dr. Grotjohn's Group (MSU), provided boron-doped diamond samples; Dr. Goodnick's Group (ASU), theoretical modeling of phonon dispersion done by Reza Vatan Meidanshahi; Dr. Smith's Group (ASU), provided *c*-BN and *t*-BN samples with support from Avani Patel and Saurabh Vishwakarma who also provided TEM images.

The text and figures of this dissertation, in full, is a reprint of the material as it appears in the following journals:

Erick Guzman, Fariborz Kargar, Frank Angeles, Reza Meidanshahi, Timothy Grotjohn, Aaron Hardy, Matthias Muehle, Richard Wilson, Stephen Goodnick, & Alexander A. Balandin (2022). “Effects of boron doping on the bulk and surface acoustic phonons in single-crystal diamond.” *ACS Applied Materials & Interfaces*, 14(37) 42223-42231 <https://doi.org/10.1021/acsami.2c10879>. Copyright © 2024, American Chemical Society.

Erick Guzman, Fariborz Kargar, Avani Patel, Saurabh Vishwakarma, Dylan Wright, Richard B. Wilson, David J. Smith, Robert J. Nemanich, & Alexander A. Balandin (2023). “Optical and acoustic phonons in turbostratic and cubic boron nitride thin films on diamond substrates”. *Diamond and Related Materials*, 140, 110452 <https://doi.org/10.1016/j.diamond.2023.110452> Copyright © 2024, Elsevier B.V.

ABSTRACT OF THE DISSERTATION

Acoustic Phonons in Ultra-Wide-Band-Gap Semiconductors Investigated
With Brillouin - Mandelstam Spectroscopy

by

Erick A. Guzman

Doctor of Philosophy, Graduate Program in Electrical Engineering
University of California, Riverside, March 2025
Dr. Alexander Balandin, Chairperson

This dissertation describes the study of acoustic phonons in ultra-wide-band gap semiconductor materials using the Brillouin – Mandelstam and Raman light scattering spectroscopies. Acoustic phonons are the main heat carriers in this type of semiconductor materials and the knowledge of the phonon frequencies and group velocities is important for fundamental science and future practical applications. The Brillouin – Mandelstam spectroscopy allows the probing of both bulk and surface acoustic phonons. In the first part of the dissertation, I describe the investigation of bulk and surface acoustic phonons in the undoped and boron-doped diamond films. It was found that the frequency and the group velocity of acoustic phonons decrease non-monotonically with the increasing boron doping concentration, revealing pronounced phonon softening. The change in the velocity of the shear horizontal and the high-frequency pseudo-longitudinal acoustic phonons in the

degenerately doped diamond, as compared to the undoped diamond, was as large as ~15% and ~12%, respectively. As a result of boron doping, the velocity of the bulk longitudinal and transverse acoustic phonons decreased correspondingly. As a result of boron doping, the velocity of the bulk longitudinal and transverse acoustic phonons decreased correspondingly. The frequency of the optical phonons was unaffected at low boron concentration but experienced a strong decrease at the high doping level. In the second part of the dissertation, I will describe the results of our investigation of the bulk optical, bulk acoustic, and surface acoustic phonons in thin films of turbostratic boron nitride (*t*-BN) and cubic boron nitride (*c*-BN) grown on B-doped polycrystalline and single-crystalline diamond (001) and (111) substrates. It was found that while visible Raman spectroscopy provided information for characterizing the *t*-BN phase, it faced challenges in differentiating the *c*-BN phase either due to the presence of high-density defects or the overlapping of the Raman features with those from the B-doped diamond substrates. In contrast, Brillouin-Mandelstam spectroscopy clearly distinguishes the bulk longitudinal and surface acoustic phonons of the *c*-BN thin films grown on diamond substrates. These findings provide valuable insights into the phonon characteristics of the *c*-BN and diamond interfaces.

TABLE OF CONTENTS

TITLE PAGE -----	i
COPYRIGHT PAGE -----	ii
ACKNOWLEDGEMENTS -----	iv
ABSTRACT -----	1
TABLE OF CONTENTS -----	ix
LIST OF FIGURES -----	4
LIST OF TABLES -----	7
CHAPTER 1 – INTRODUCTION -----	8
1.1 Outline -----	8
1.2 Motivation-----	9
1.3 Experimental Setup for Brillouin Spectroscopy-----	14
CHAPTER 2 – EFFECTS OF BORON DOPING ON THE BULK AND SURFACE ACOUSTIC PHONONS IN SINGLE – CRYSTAL DIAMOND -----	17
2.1 Introduction-----	17
2.2 Methods-----	19
2.2.1 Diamond Growth -----	19
2.2.2 Brillouin-Mandelstam Spectroscopy-----	20
2.2.3 Refractive Index Measurements -----	20
2.2.4 Density-Functional-Theory (DFT) Calculations-----	21
2.3 Results-----	22
2.3.1 Measurements-----	22
2.3.2 Modeling -----	44
2.4 Discussion-----	49
2.5 Conclusions-----	54
2.6 References -----	55
CHAPTER 3 – OPTICAL AND ACOUSTIC PHONONS IN TURBOSTRATIC AND CUBIC BORON NITRIDE THIN FILMS ON DIAMOND SUBSTRATES --	61
3.1 Introduction-----	61
3.2 Materials & Methods-----	66
3.3 Results and Discussion -----	69
3.3.1 TEM Analysis -----	69
3.3.2 Raman Analysis-----	74
3.3.3 BMS Results -----	73
3.4 Conclusions-----	96
3.5 References -----	97
CHAPTER 4 – CONCLUSION -----	102

LIST OF FIGURES

Figure 1 – Image of the BLS experimental setup	8
Figure 2 – Schematic of the BLS optical path including TFP interferometer	9
Figure 3 – Raman spectra of undoped and boron doped diamond under 633 nm excitation	16
Figure 4 – Raman spectra of the ZCP peak in undoped and boron doped diamond under 633 nm excitation	17
Figure 5 – Spectral position and FWHM of the ZCP in undoped and boron doped diamond.....	18
Figure 6 – Normalized Raman spectra of the ZCP undoped and boron doped diamond under 325 nm excitation	20
Figure 7 – Normalized Raman spectra of the ZCP undoped and boron doped diamond under 488 nm excitation.....	21
Figure 8 – Normalized Raman spectra of the ZCP undoped and boron doped diamond under 633 nm excitation.....	22
Figure 9 – BLS spectra of the bulk phonons in undoped and boron doped diamond.....	24
Figure 10 – Fitted BLS spectra of the bulk phonons in undoped diamond	25
Figure 11 – Fitted BLS spectra of the bulk phonons in the doped diamond with boron concentration of 10^{16} cm^{-3}	26
Figure 12 – Fitted BLS spectra of the bulk phonons in the doped diamond with boron concentration of 10^{17} cm^{-3}	27

Figure 13 – Fitted BLS spectra of the bulk phonons in the doped diamond with boron concentration of $3 \times 10^{20} \text{ cm}^{-3}$	28
Figure 14 – BLS spectra of the surface phonons in undoped and doped diamond	33
Figure 15 – Spectral position and velocity of surface phonons in doped and undoped diamond	35
Figure 16 – Calculated phonon dispersion of undoped diamond and experimental neutron scattering.....	38
Figure 17 – Supercell structure of undoped and doped diamond	40
Figure 18 – Phonon group velocity of bulk phonon modes as a function of boron concentration.....	40
Figure 19 – Calculated phonon dispersion of undoped and doped diamond.....	41
Figure 20 – TEM images of the t-BN film on B-doped polycrystalline diamond.....	63
Figure 21 – TEM images of the c-BN-1 film on (001) single crystal diamond.....	65
Figure 22 –TEM images of the c-BN-2 film on (111) single crystal diamond.....	66
Figure 23 – Raman spectra of the t-BN film under 488 nm excitation.....	68
Figure 24 – Raman spectra of the bulk single crystal c-BN under 488 nm excitation	69
Figure 25 – Raman spectra of the c-BN-1 film under 488 nm excitation	71
Figure 26 – Raman spectra of the c-BN-2 film under 488 nm excitation.....	72
Figure 27 – BLS spectra of the bulk phonon modes in the t-BN film.....	74
Figure 28 – BLS spectra of the bulk phonon modes in the bulk c-BN.....	75
Figure 29 – BLS spectra of the bulk phonon modes in the c-BN-1 film.....	77
Figure 30 – BLS spectra of the bulk phonon modes in the c-BN-2 film.....	79

Figure 31 – BLS spectra of the surface phonon modes in the c-BN-1 film.....	82
Figure 32 – BLS spectra of the surface phonon modes in the c-BN-2 film.....	83
Figure 33 – Spectral position and phase velocity of the surface phonon modes in the c-BN-1 film.....	85
Figure 34 – Spectral position and phase velocity of the surface phonon modes in the c-BN-2 film.....	87

LIST OF TABLES

Table 1 – ZCP peak position and FWHM from 633 nm Raman	23
Table 2 – Position, FWHM, and relative intensity of BMS peaks in BDD	29
Table 3 – Index of refraction and group velocity of fundamental phonon modes	32
Table 4 – Calculated and reported values of boron nitride and diamond films	88

CHAPTER 1 – INTRODUCTION

1.1 Outline

In the first chapter, I introduce the motivation for the work. Followed by the Brillouin light scattering technique and the experimental BLS setup which is the main technique used in the studies. In the second chapter, I will describe the results of our study on the effects of boron doping on the bulk and surface acoustic phonons of single crystal diamond. It was found that the frequency and group velocity of the bulk and surface acoustic phonons decrease as the boron concentration increases. The phonon softening observed is important information to consider when the diamond is used as a material for thermal management. In the third chapter, I introduce the results of our study of the optical and acoustic phonons of boron nitride thin films on diamond substrates. Studies of the surface acoustic waves in the cubic boron nitride films revealed higher Rayleigh wave velocities on (111) diamond substrates. A higher acoustic phonon velocity denotes a relatively higher quality film and holds important implications for evaluating thermal conductance across interfaces. In the final chapter, I will summarize the work and findings of my two published papers and provide concluding remarks about the research of acoustic phonons in UWBG materials.

1.2 Motivation

Current research is focused on UWBG semiconductors as replacements for conventional technology such as silicon in many aspects of electronics [1-3]. The UWBG moniker is given to materials with a bandgap higher than Gallium Nitride (GaN) which is 3.2 eV. Specifically, UWBG semiconductors are seen as promising materials for use in high-power electronics due to properties that are suited for this type of application, some of the properties include high thermal conductivity, breakdown field, and current density [4,5]. The most promising material in this category is diamond followed by *c*-BN, these two materials have the first and second highest thermal conductivity, respectively. Purely looking at material properties, diamond holds the record for many physical properties suited for high-power applications, it can move large amounts of heat and current and sustain large voltages as an insulator [4,6]. *c*-BN has the benefit of having a high thermal conductivity and breakdown field, and it is only bested by diamond [7]. Both materials have their respective drawbacks, such as the difficulty of doping diamond successfully with a deep donor to make it n-type [8,9] and the difficulty of growing single crystal of *c*BN because, during growth it favors other phases such as the turbostratic or hexagonal phase [10,11]. However, insight into thermal properties or material quality can still be gained in the materials by studying their phonon properties.

Utilizing various spectroscopic techniques, information can be gained on the phonons in these materials. Raman spectroscopy gives us information on the optical phonons while Brillouin spectroscopy gives information on the acoustic phonons. Analyzing the optical phonon frequencies allows us to determine different phases, sample purity, and defect concentration in the sample. However, the optical phonon dispersion bands are flat compared to acoustic phonon dispersion bands which are linear and allow us to calculate the group velocity. Performing studies of the bulk acoustic phonons give the group velocity which is an important piece of information. The group velocity is a physical property which is present in the thermal conductivity equation. The bulk acoustic phonons are the main carriers of heat in materials like diamond and being able to connect this finding to doping concentration for example, can give us insight into thermal properties of these materials. BLS studies allow you to probe both the bulk and surface acoustic phonons [12]. The calculated group velocity of surface phonons can help qualitatively compare materials to determine surface quality which is important for interface thermal conductivity. Combining both spectroscopic techniques can give us a wider understanding of the thermal properties of a material through their phonon propagation. The main technique used in this work is Brillouin spectroscopy, which is similar to Raman spectroscopy but with key differences. Firstly, both techniques measure the inelastic scattering of photons, and follow momentum and energy conservation rules. However, the measured Brillouin scattering is many times weaker than the Raman scattering. Both techniques measure the frequency of vibrations with wavevectors that are extremely close to the gamma point, but Raman spectroscopy measures frequencies in the THz range, on the other hand Brillouin

spectroscopy measures frequencies in the GHz range. Also, the implementation of Brillouin spectroscopy instrumentation is much more complicated as there is no off the shelf experimental setup. In the next section the BLS experimental setup used is explained in more detail.

References

- (1) Mazumder, S. K.; Voss, L. F.; Dowling, K. M.; Conway, A.; Hall, D.; Kaplar, R. J.; Pickrell, G.; Flicker, J.; Binder, A.; Chowdhury, S.; Veliadis, V.; Luo, F.; Khalil, S.; Aichinger, T.; Bahl, S.; Meneghini, M.; Charles, A. Overview of Wide/Ultrawide Bandgap Power Semiconductor Devices for Distributed Energy Resources. *IEEE J. Emerg. Sel. Top. Power Electron.* **2023**, 11 (4), 3957–3982. <https://doi.org/10.1109/JESTPE.2023.3277828>
- (2) Bader, S.; Lee, H.; Chaudhuri, R.; Huang, S.; Hickman, A.; Molnar, A.; Xing, H.; Jena, D.; Then, H.; Chowdhury, N.; Palacios, T. Prospects for Wide Bandgap and Ultrawide Bandgap CMOS Devices. *IEEE Trans. Electron Devices* **2020**, 67 (10), 4010–4020. <https://doi.org/10.1109/TED.2020.3013932>
- (3) Qin, Y.; Albano, B.; Spencer, J.; Lundh, J. S.; Wang, B.; Buttay, C.; Tadjer, M.; DiMarino, C.; Zhang, Y. Thermal Management and Packaging of Wide and Ultra-Wide Bandgap Power Devices: A Review and Perspective. *J. Phys. D: Appl. Phys.* **2023**, 56 (12), 123003 <https://doi.org/10.1088/1361-6463/acb4ff>
- (4) Woo, K.; Bian, Z.; Noshin, M.; Perez Martinez, R.; Malakoutian, M.; Shankar, B.; Chowdhury, S. From Wide to Ultrawide-Bandgap Semiconductors for High Power and High Frequency Electronic Devices. *J. Phys. Mater.* **2024**, 6, 015002. <https://doi.org/10.1088/2515-7639/ad218b>
- (5) Wong, M. H.; Bierwagen, O.; Kaplar, R. J.; Umezawa, H. Ultrawide-Bandgap Semiconductors: An Overview. *J. Mater. Res.* **2021**, 36, 4601–4615. <https://doi.org/10.1557/s43578-021-00458-1>
- (6) Anthony, T. R.; Banholzer, W. F.; Fleischer, J. F.; Wei, L.; Kuo, P. K.; Thomas, R. L.; Pryor, R. W. Thermal Diffusivity of Isotopically Enriched ^{12}C Diamond. *Phys. Rev. B* **1990**, 42 (2), 1104–1111. <https://doi.org/10.1103/PhysRevB.42.1104>
- (7) Tsao, J. Y.; Chowdhury, S.; Hollis, M. A.; Jena, D.; Johnson, N. M.; Jones, K. A.; Kaplar, R. J.; Rajan, S.; van de Walle, C. G.; Bellotti, E.; Chua, C. L.; Collazo, R.; Coltrin, M. E.; Cooper, J. A.; Evans, K. R.; Graham, S.; Grotjohn, T. A.; Heller, E. R.; Higashiwaki, M.; Islam, M. S.; Juodawlkis, P. W.; Khan, M. A.; Koehler, A. D.; Leach, J. H.; Mishra, U. K.; Nemanich, R. J.; Pilawa-Podgurski, R. C. N.; Shealy, J. B.; Sitar, Z.; Tadjer, M. J.; Witulski, A. F.; Wraback, M.; Simmons, J. A. Ultrawide-Bandgap Semiconductors: Research Opportunities and Challenges. *Advanced Electronic Materials* **2018**, 4 (1), 1600501. <https://doi.org/10.1002/aelm.201600501>.
- (8) Lyons, J. L.; Wickramaratne, D.; Janotti, A. Dopants and Defects in Ultra-Wide Bandgap Semiconductors. *Curr. Opin. Solid State Mater. Sci.* **2024**, 28 (1), 101148. <https://doi.org/10.1016/j.cossms.2024.101148>

- (9) Liu, S.; Li, H.; Bai, X.; Zhang, X.; Liao, J. Lightly Phosphorus-Doped Homoepitaxial Diamond Films Grown by Chemical Vapor Deposition. *J. Cryst. Growth* **2000**, 218 (1–2), 159–163. [https://doi.org/10.1016/S0925-9635\(00\)00217-X](https://doi.org/10.1016/S0925-9635(00)00217-X)
- (10) Zhang, W. J.; Chong, Y. M.; Bello, I.; Lee, S. T. Nucleation, Growth, and Characterization of Cubic Boron Nitride (cBN) Films. *J. Phys. D: Appl. Phys.* **2007**, 40 (20), 6159. <https://doi.org/10.1088/0022-3727/40/20/S03>
- (11) Han, Y.; Ma, D.; Gu, C.; Fu, Y.; Zhao, Y.; Wang, S. New Insights into the Mechanism for Growing Cubic Boron Nitride Crystals under High Pressure. *Cryst. Growth Des.* **2024**, 24 (12), 5089–5096. <https://doi.org/10.1021/acs.cgd.4c00313>
- (12) Kargar, F.; Balandin, A. A. Advances in Brillouin–Mandelstam Light-Scattering Spectroscopy. *Nature Photonics* **2021**, 15 (10), 720–731. <https://doi.org/10.1038/s41566-021-00836-5>.

1.3 Experimental Setup for Brillouin Spectroscopy

In Brillouin experiments a vertically polarized 532 nm excitation laser capable of outputting 300mW is utilized. The laser beam is attenuated immediately at the output to keep the laser power under 10mW and avoid laser heating. The laser heating experienced per sample is dependent on factors such as the beam diameter of the laser and thermal conductivity of the sample. A beam splitter passes low intensity reference light directly to the Fabry Perot (FP) interferometer which is used in the alignment mode to calibrate the system. After the beam splitter, a series of mirrors, pinholes, and lens are used to redirect the laser light to the sample. Before the sample there is a partially blocked mirror to redirect the laser to the sample in the incident path meanwhile blocking the strong laser light along the scattered path, basically highlighting the weak Brillouin scattered light. This scattered light is collected using another series of mirrors and lens and refocused into the entrance pinhole of the FP interferometer. Before the scattered light continues into the interferometer, the laser path is checked for proper alignment. The laser is aligned so that it is parallel to the plane of the optical table, and the alignment is tested by using a mirror at the entrance pinhole. The light should redirect back through itself as far back into the light path as possible. In the tandem mode of the FP interferometer, the scattered light passes through two sets of plane mirrors referred to as etalons, in conjunction with the reference light. The etalon spacing determines the free spectral range of your measurement allowing you to probe in the MHz to GHz range. The unique interferometer light path establishes differences between the reference light and the scattered light using wave

interference, which is sent to the photodetector. The detector converts the light signal to an electrical signal with information about the frequency shift with respect to the wavelength of the reference light of the measured acoustic phonons. An image of one of the group's Brillouin spectroscopy setups is shown in Figure 1, followed by a schematic of the optical path and internal TFP in Figure 2

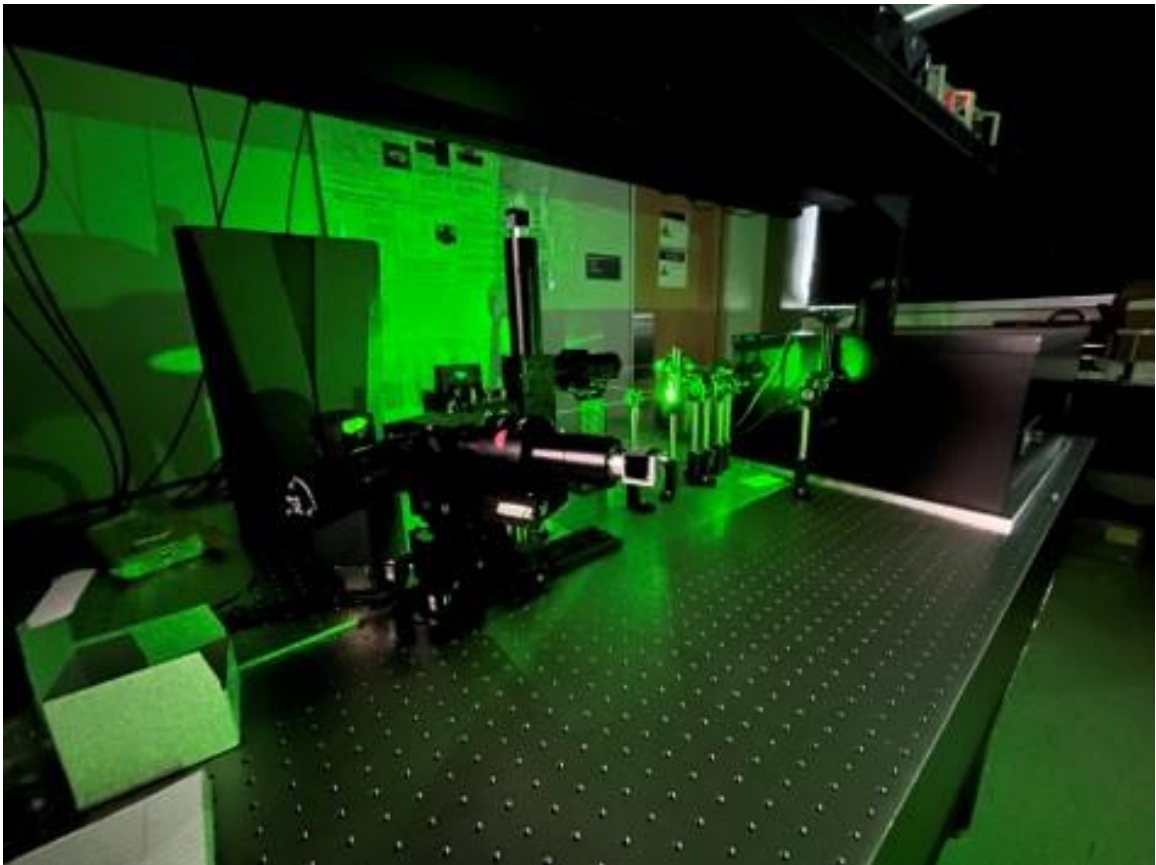


Figure 1: Image of Brillouin setup on optical table at UCR. From left to right is the cryocooler capable of 4K temperatures, optical microscope, beam path shown with 532 nm laser, and the TFP-2 from Tablestable. Image courtesy of Dylan Wright.

FP Interferometer (Inside View)

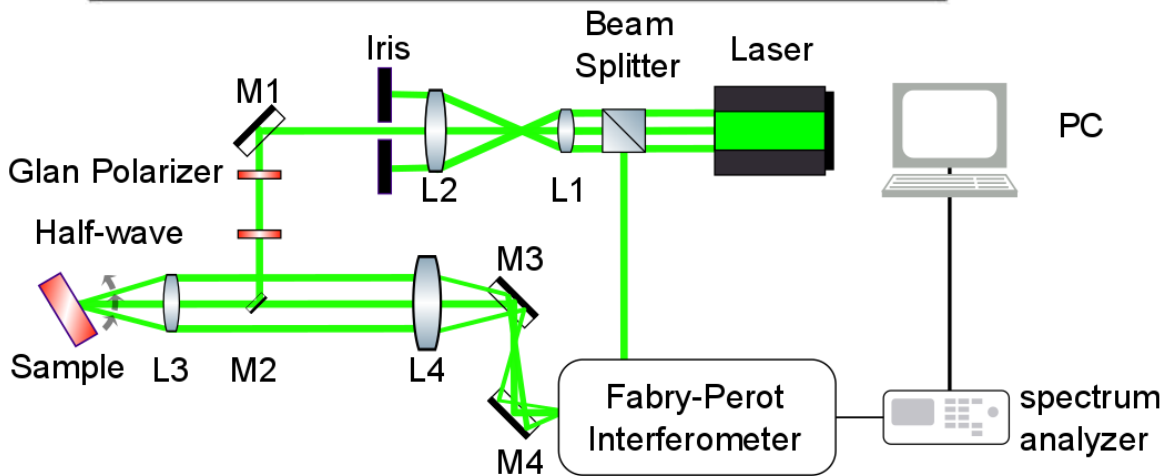
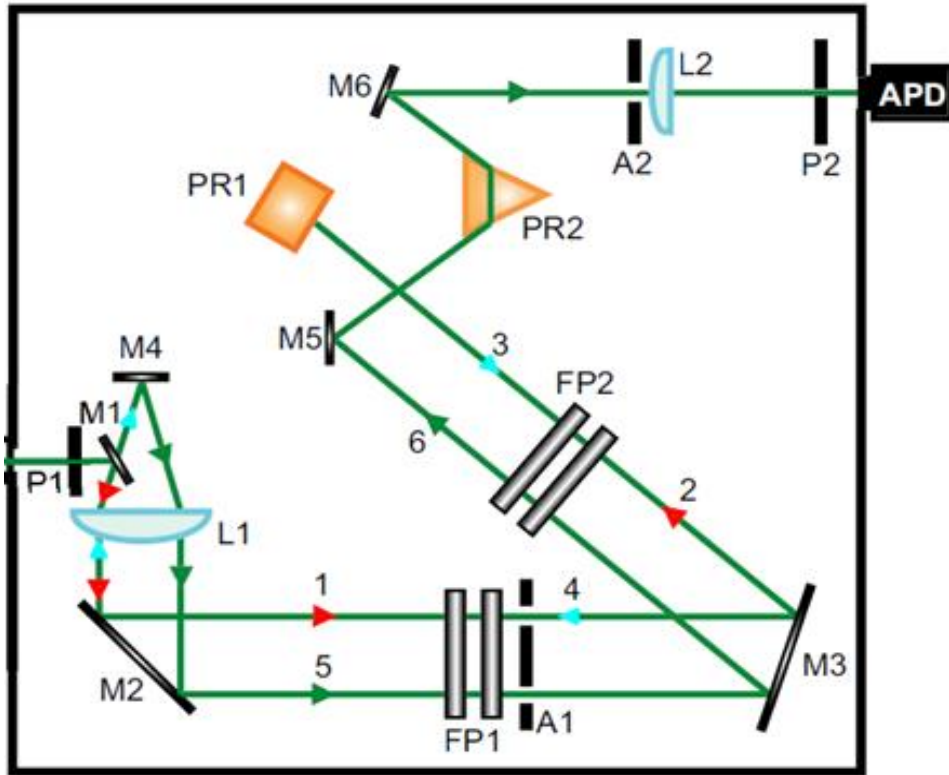


Figure 2: Schematic of the inside of the Fabry Perot interferometer (TFP1) and the setup of the external optics used in this work used to perform BLS experiments. Image courtesy of Dr. Fariborz Kargar

CHAPTER 2 – EFFECTS OF BORON DOPING ON THE BULK AND SURFACE ACOUSTIC PHONONS IN SINGLE – CRYSTAL DIAMOND

2.1 Introduction

Recent years witnessed a rapid growth of interest in ultra-wide bandgap (UWBG) semiconductors for applications in power electronics[1–4]. The materials, which belong to the UWBG group, include semiconductors such as AlN and diamond, with an electronic bandgap ranging from 3 eV to 6 eV[3]. Among UWBGs, diamond attracts the most attention as it holds a record-high current density, thermal conductivity, mechanical stiffness, chemical stability, and the critical electric field [5-9]. Intrinsic diamond is an electrical insulator; it is doped by boron (B) to become a *p*-type semiconductor, suitable for electronic applications [10]. In diamond, the bulk acoustic phonons, *i.e.*, quanta of crystal lattice vibrations, are the main heat carriers. They have high group velocities and long lifetimes [7-9]. These characteristics are responsible for the diamond's high thermal conductivity of $\sim 2200 \text{ Wm}^{-1}\text{K}^{-1}$ at room temperature (RT) and excellent thermal interface conductance [1,7-9,11]. The frequency and dispersion of acoustic phonons are also related to the elastic and mechanical properties of the material. While boron substitutional doping improves the electrical conductivity of diamond, it adversely affects its phonon heat conduction characteristics [12-14]. Boron atoms act as point defects, scattering acoustic phonons, shortening their lifetime, and thus reducing the thermal conductivity of the material [12-15]. Although the phonons in diamond have been investigated extensively,

the data on the surface and bulk acoustic phonons in doped diamond are scarce and rather controversial. An important open question is “Do boron atoms only act as the scattering centers for acoustic phonons, which retain the frequency and velocity of intrinsic diamond, or do the dopant atoms alter the phonon characteristics of the material themselves?” The effect of doping on the surface acoustic phonons in diamond has also not been addressed. The properties of the surface phonons are important for understanding the thermal transport across interfaces in the device structures.

Brillouin-Mandelstam light scattering (BMS), also referred to as Brillouin light spectroscopy (BLS), is a nondestructive optical technique that has been used extensively to study acoustic phonons in different types of materials [16]. This technique has been employed to examine the mechanical properties of different types of diamond, *e.g.*, polycrystalline, smooth fine-grained, and single-crystal diamond grown by chemical vapor deposition (CVD) method [17-20]. The prior studies reported the characteristics of bulk longitudinal acoustic (LA) and transverse acoustic (TA) phonons as well as the traveling surface acoustic phonons (SAWs) along the high-symmetry crystallographic directions [19,20]. The elasticity coefficients of diamond were extracted from BMS data [17-20]. A recent detailed study has used the angle-resolved BMS to find the properties of SAWs along different crystallographic directions in diamond [21]. No BMS data on the effect of boron on bulk and surface acoustic phonons in boron-doped diamond have been reported to date. In this work, the BMS technique was used to investigate the bulk and surface acoustic phonons in the low, medium, and highly boron-doped CVD-grown diamond films

and compared the results to that of the undoped high-pressure high temperature (HPHT) diamond. The evolution of optical phonons in the same samples was monitored with Raman spectroscopy. It was found that the frequency and group velocity of acoustic phonons decrease non-monotonically with the increasing boron doping concentration, revealing pronounced *phonon softening*. The phonon modification with the introduction of dopant atoms appears to be stronger than previously believed. The observed changes in the characteristics of acoustic phonons in diamond because of doping have important broad implications for heat conduction in UWBG materials and for the thermal management of UWBG-based electronic devices [22].

2.2 Methods

2.2.1 Diamond Growth

The boron-doped diamond samples were provided by the Timothy Grotjohn group at Michigan State University and were grown by microwave plasma-assisted chemical vapor deposition using hydrogen and methane feed gases, with the boron added during the homoepitaxial growth using diborane feed gas. The substrates used were HPHT seeds that were prepared with an off-cut angle of the growth surface of $\sim 3^\circ$ from the (001) crystal plane. The boron concentrations were estimated based on similarly grown samples grown with equivalent conditions that were measured by secondary ion mass spectroscopy (SIMS) at EAG.

2.2.2 Brillouin-Mandelstam Spectroscopy

BMS experiments were conducted in the conventional backscattering configuration using a 532 nm laser excitation wavelength at several different incident angles. The light source was a solid-state diode-pumped continuous-wave laser (Spectra Physics). The laser beam was focused on the sample using a lens with NA=0.34. The scattered light was collected via the same lens and directed to the high-contrast high-resolution 3 + 3 pass tandem Fabry-Perot interferometer (TFP-1, JRS Optical Instruments, Switzerland) and spectrometer. For bulk and surface acoustic phonon measurements, the mirror spacing of the TFP interferometer was adjusted to 0.5 and 2 mm, respectively.

2.2.3 Refractive Index Measurements

The refractive index measurements of the diamond thin films were performed by Frank Angeles in Dr. Wilson's group at the University of California, Riverside and determined by measuring the Fresnel reflectance coefficients for s- and p-polarized 515 nm lights. For the reflectance measurements, a linearly polarized laser beam was used with a polarization of 45° from the vertical. The light was focused on the sample using a 10× objective lens. The angle of incidence of the beam with the sample was kept at 45°. Light reflected from the sample was collected by another 10× objective lens. The light that reflected from the

sample's back surface was spatially separated from the primary reflected beam with an aperture. The intensity and polarization of the reflected probe beam were measured by a calibrated power meter and a polarimeter. A multilayer optical calculation was used to analyze the reflectance data. The index of refraction of the diamond film was treated as a fitting parameter until the model predictions matched the experimental observations for the polarization and intensity of the reflected laser beam.

2.2.4 Density-Functional-Theory (DFT) Calculations

The ultra-soft pseudopotential and the generalized gradient approximation (GGA) of the Perdew–Burke–Ernzerhof (PBE) [60] functional were employed to describe the core–valence electron interaction and exchange– correlation energy, respectively. The kinetic energy cutoff of 25 Ry was chosen for plane-wave basis sets. A cube supercell containing eight atoms was used in our DFT calculations. For boron-doped diamond, one of the C atoms was replaced by B, which was equivalent to the $\sim 2 \times 10^{22} \text{ cm}^{-3}$ doping concentration. Both supercell size and atomic positions were relaxed using the BFGS quasi-Newton algorithm within DFT until the force on each atom was smaller than 0.001 Ry/Bohr. In the self-consistent ground-state calculations, an $8 \times 8 \times 8$ Monkhorst–Pack k-point setting was used in the reciprocal space integration. After obtaining the self-consistent ground state, the density functional perturbation theory (DFPT) [61] calculations were performed with a uniform $4 \times 4 \times 4$ grid of q-point setting. Then, dynamical matrix

Fourier transformations were performed to obtain force constants and calculated the phonon dispersions. To benchmark our method of calculations, the phonon dispersion of pure diamond was calculated using an FCC unit cell containing two carbon atoms with an experimental lattice constant of 3.57 Å (Figure 17) and was compared with experimental data [42].

2.3 Results

2.3.1 Measurements

The single-crystal diamond films for this study have been grown by the CVD method on the HPHT diamond substrate synthesized via the high-pressure high-temperature method. The details of the growth and boron doping procedures have been reported by some of us elsewhere [23,24]. The quality of the CVD diamond and characteristics of optical phonons were assessed with Raman spectroscopy. The samples with the boron doping concentrations of 10^{16} , 10^{17} , and $3 \times 10^{20} \text{ cm}^{-3}$ were referred to as the low-doped, medium-doped, and highly doped diamond, respectively. Systematic Raman measurements were conducted using a 633 nm wavelength excitation laser in a conventional backscattering configuration. The laser power was kept low at $\sim 60 \text{ } \mu\text{W}$ all the time to eliminate any possible laser-induced heating effects. Measurements were also performed with 325 nm and 488 nm wavelength excitation lasers using 1mW and 900 μW laser power respectively.

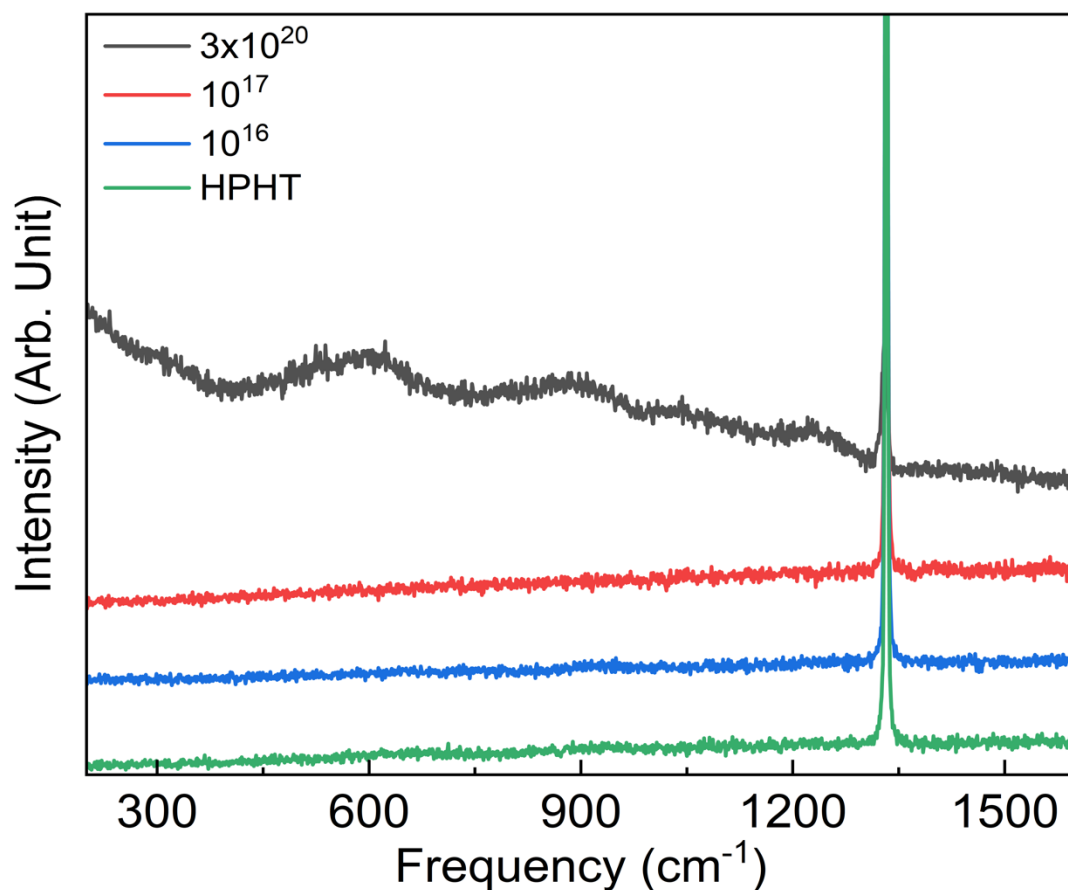


Figure 3: Raman spectra of the boron-doped diamond samples and a reference undoped HPHT diamond recorded under a 633-nm excitation laser. The figure is adapted from E. Guzman *et al.*, “Effects of Boron Doping on the Bulk and Surface Acoustic Phonons in Single-Crystal-Diamond”, ACS Appl. Mater. Interfaces 14(37) (2022) 42223-42231. Reprinted with permission from the American Chemical Society, Copyright © 2024

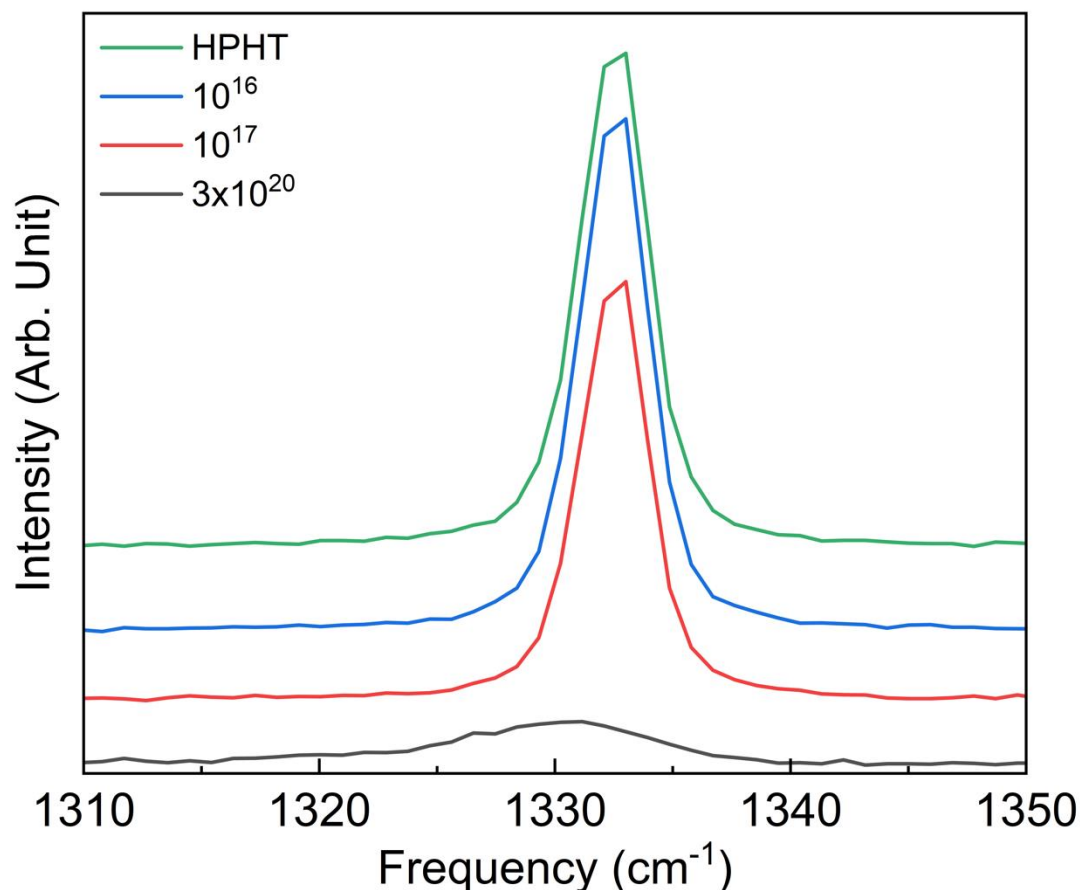


Figure 4: Raman spectra for the boron doped diamond samples and the reference undoped HPHT diamond in the vicinity of the diamond’s zone-center optical phonon peak at $\sim 1332\text{ cm}^{-1}$. The figure is adapted from E. Guzman *et al.*, “Effects of Boron Doping on the Bulk and Surface Acoustic Phonons in Single-Crystal-Diamond”, ACS Appl. Mater. Interfaces 14(37) (2022) 42223-42231. Reprinted with permission from the American Chemical Society, Copyright © 2024

In Figure 3, the typical Raman spectra is presented for all types of diamond films and the reference HPHT diamond. Comparing the data, one finds additional Raman features appearing as broad peaks in the range of $300\text{--}1300\text{ cm}^{-1}$ in the sample with the highest boron doping concentration. These broad bands at $\sim 550, 900, 1050,$ and 1200 cm^{-1} tend to

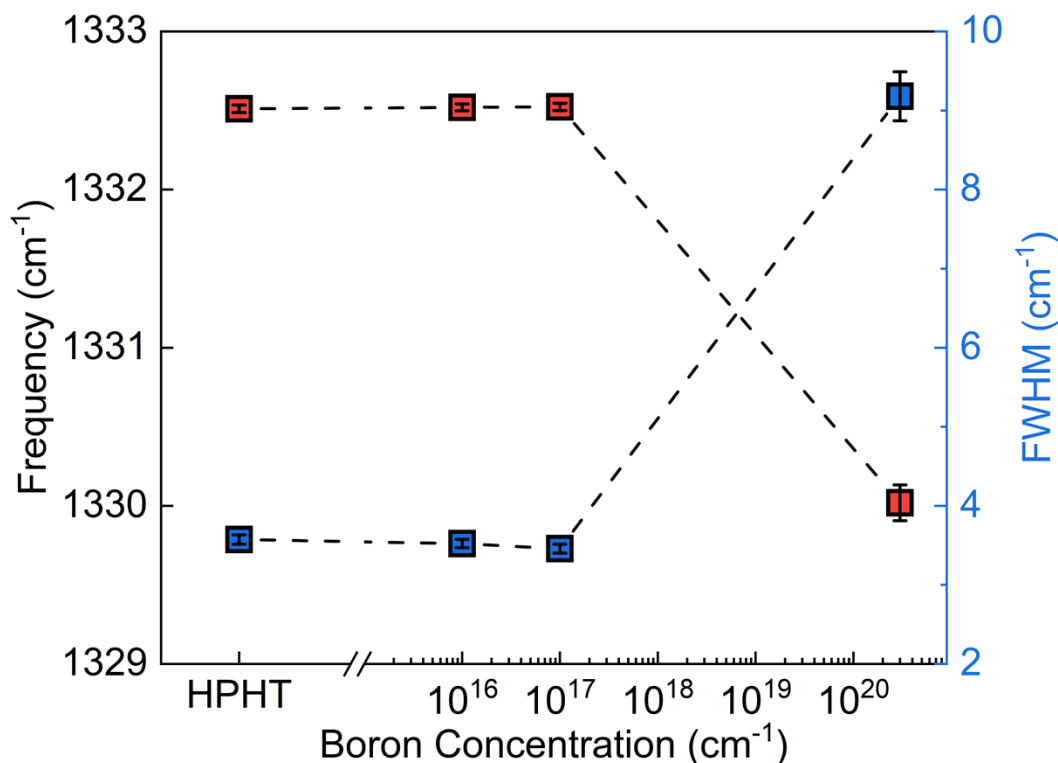


Figure 5: Spectral position (red squares) and FWHM (blue squares) of the ZCP as a function of the boron concentration. The spectral position of the peak decreases by 2 cm^{-1} while its FWHM increases significantly for the highly doped diamond. Reprinted with permission from Guzman et al., “Effects of Boron Doping on the Bulk and Surface Acoustic Phonons in Single-Crystal-Diamond”, ACS Appl. Mater. Interfaces 14(37) (2022) 42223-42231. Copyright © 2024, American Chemical Society

appear in boron-doped diamond samples. Their intensity and spectral position can differ at concentrations close to the insulator-to-metal transition [25]. The transition occurs at high boron doping similar to our highly B-doped sample. These peaks are activated in diamond as a result of some structural disorder induced by high boron inclusion [26,27]. The broad bands near 1200 and 550 cm^{-1} are generally attributed to the forbidden Raman peaks that correspond to the maximum phonon density of states and the maximum density of states of the acoustic phonons in diamond, respectively [28]. More detailed discussions of these

peaks are provided in Ref [26,28] In all spectra, the intense peak at $\sim 1332 \text{ cm}^{-1}$ originates from the Brillouin zone (BZ) center optical phonons of diamond, referred to here as the zone-center phonons (ZCP) [26,28].

Figure 4 shows the details of the ZCP Raman signatures. The intensity of the ZCP peak is lower in the highly doped diamond compared to that of other samples. The peak is symmetric for all types of samples, and the experimental data is fit accurately using a single Lorentzian function. Several prior Raman studies have reported that boron doping induces an asymmetry in the ZCP peak, which changes its shape from a Lorentzian-like to a Fano-like peak [26,28]. The latter is explained by an increased contribution of scattering by free charge carriers in the highly doped samples [28]. This change is also observed in Raman spectra collected under 325 nm and 488 nm wavelength laser excitation (see Figure 6 and 7). Since no changes in the symmetry of the ZCP peak were seen in Raman spectra accumulated under the 633 nm laser excitation, the conclusion is that the behavior of the ZCP peak depends strongly on the wavelength of the excitation laser.

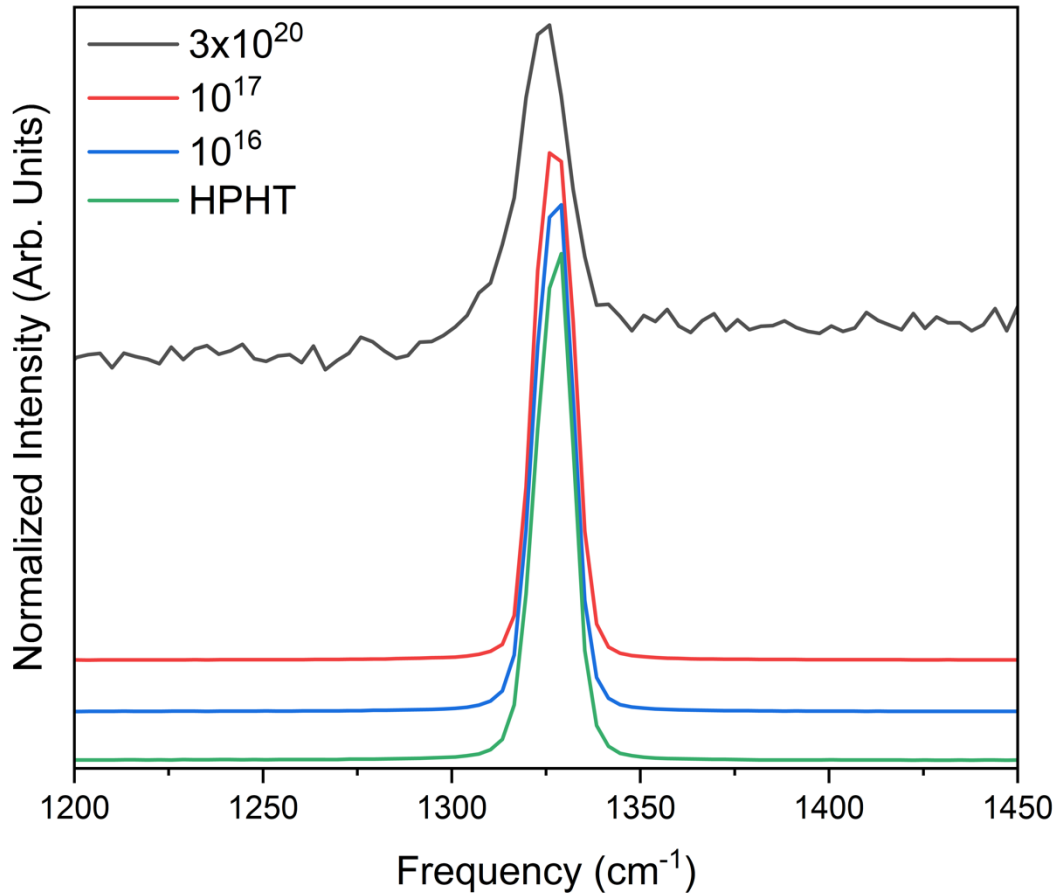


Figure 6: Normalized Raman spectra of the boron doped diamond samples and reference HPHT diamond performed using 325 nm excitation laser.

In Figure 5, the spectral position and the full width at half-maximum (FWHM) of this Raman peak determined using the Lorentzian fittings is shown. The exact data are also provided in Table 1. The spectral position and the FWHM of the optical phonons remain unchanged for the low and medium boron-doped samples compared to those for the undoped HPHT reference sample. In the highly doped diamond, however, the ZCP peak red-shifts by $\sim 2 \text{ cm}^{-1}$, exhibiting the *optical phonon softening* behavior. The change in the

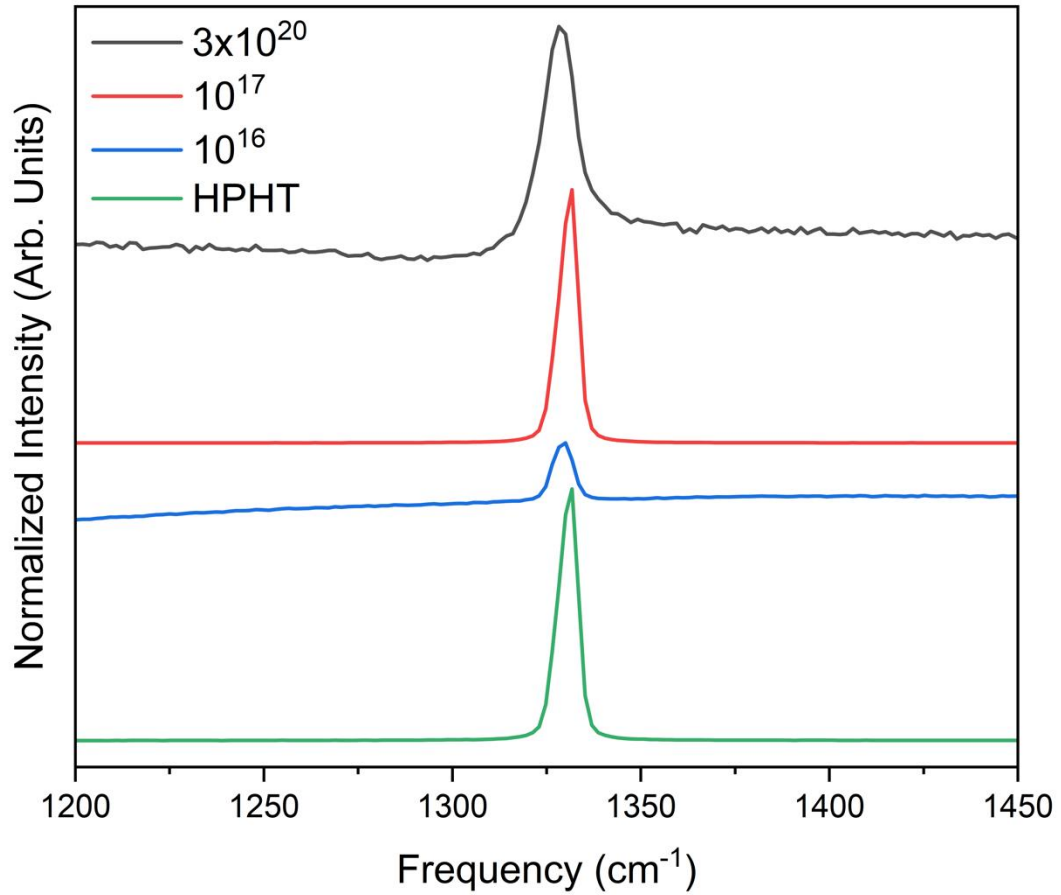


Figure 7: Normalized Raman spectra of the boron doped diamond samples and reference HPHT diamond performed using 488 nm excitation laser.

spectral position of the ZCP Raman peak is higher than the hardware resolution of our Raman system, which is $\sim 1 \text{ cm}^{-1}$. Moreover, its FWHM, which inversely relates to the phonon lifetime [29], increases by a factor of ~ 3 compared to the undoped HPHT and low and medium-doped samples. This is consistent with the observation that structural disorder can also make FWHM wider [30]. If the structural disorder has a length scale L , phonons with the wavelength $q \sim 1/L$ will contribute to the scattering and, as a result, broaden the energy spectrum and lower the average energy of the first-order Raman peak [31]. Figures

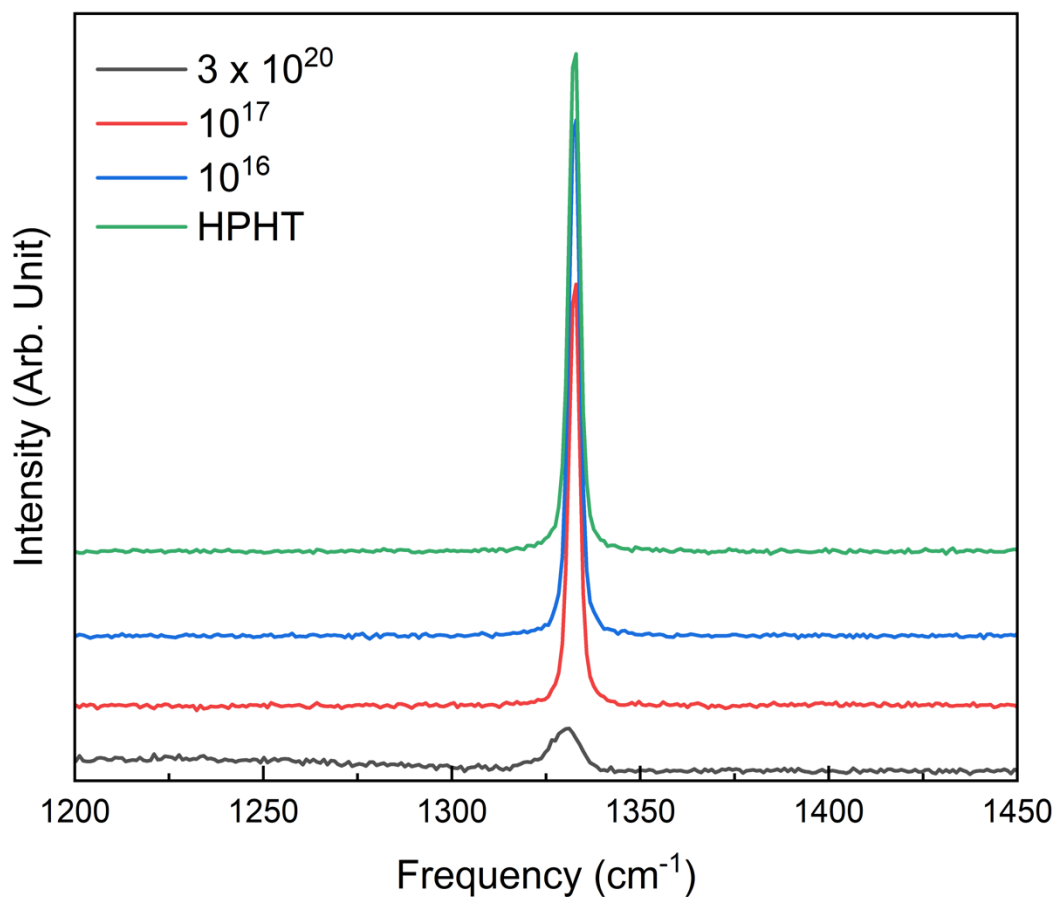


Figure 8: Normalized Raman spectra of the boron doped diamond samples and reference HPHT diamond performed using 633 nm excitation laser.

6-8 shows Raman spectra using 325 nm, 488 nm, and 633 nm wavelength excitation laser zoomed in to show the details of the ZCP in all the boron doped diamond samples. The spectra have been normalized to better portray the Fano effect. Asymmetry of the ZCP peak can be seen in the highest concentration boron doped diamond sample (black line) compared to the other samples. Possible implications of the optical phonon softening on thermal transport in diamond are discussed below.

Table 1: Spectral position and FWHM of the ZCP of pristine HPHT and BDD samples including error values from Lorentzian fitting in 633 nm Raman measurements.

	HPHT Substrate	10^{16} (cm ⁻³)	10^{17} (cm ⁻³)	3×10^{20} (cm ⁻³)
Frequency (cm ⁻¹)	1332.5	1332.5	1332.5	1330.1
Frequency Error	0.02754	0.02774	0.02735	0.11771
FWHM (cm ⁻¹)	3.04	2.97	2.92	9.07
FWHM Error	0.09137	0.09228	0.09119	0.51027

Now to the main element of this work – BMS investigation of the boron-doped diamond films. The BMS measurements were conducted in the backscattering configuration using a 532 nm excitation laser at a fixed light incident angle $\theta = 20^\circ$. The incident light was p-polarized; no specific polarization selection was used for the collection of the scattered light. The details of our BMS procedures are provided in the Methods section and prior reports for other material systems [16,32,33]. The top surfaces of the samples were the diamond's (001) crystallographic plane with an off-cut plane angle of $\sim 3^\circ$. This small off-cut angle had a negligible effect on the light scattering and did not affect the interpretation of BMS data. Figure 9 shows the results of the BMS measurements of the three boron-doped diamond samples and the HPHT diamond substrate in the frequency range of

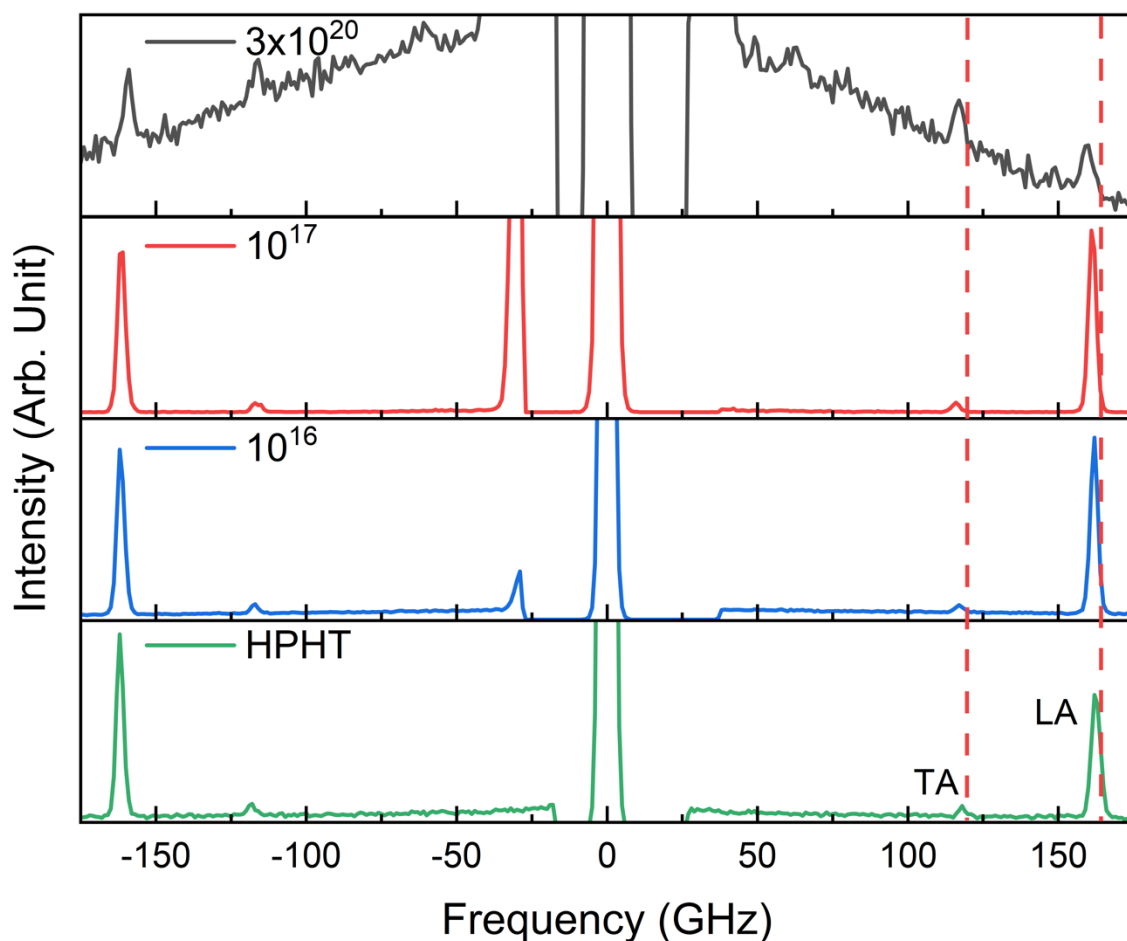


Figure 9: Brillouin light scattering spectra of the boron-doped diamond samples in the backscattering geometry performed at a 20° incidence angle. The dashed lines are guides to the eye to illustrate the decrease in the acoustic phonon frequency as the doping level increases. The peaks labeled as LA and TA correspond to the longitudinal acoustic and the transverse acoustic bulk phonons. The figure is adapted from E. Guzman *et al.*, “Effects of Boron Doping on the Bulk and Surface Acoustic Phonons in Single-Crystal-Diamond”, ACS Appl. Mater. Interfaces 14(37) (2022) 42223-42231. Reprinted with permission from the American Chemical Society, Copyright © 2024

25–175 GHz. Two sharp peaks on each side of the spectra are associated with the Stokes and anti-Stokes scattering processes by the LA and TA bulk phonons. The spectral position of the observed peaks, f , was determined accurately by fitting the experimental with individual Lorentzian functions. The details of the fitting procedures are provided in

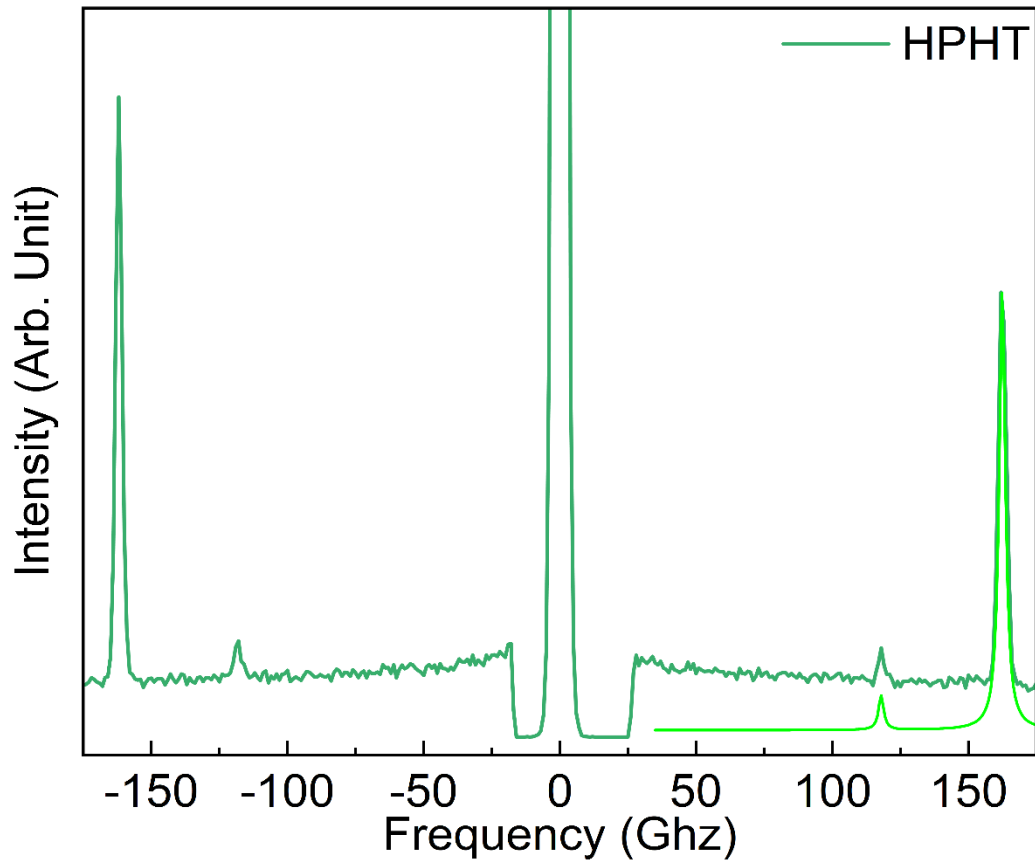


Figure 10: Lorentzian fitting of bulk Brillouin light spectra of the undoped HPHT diamond sample. The Lorentzian fitting is shown as a green overlay on the spectra.

Figures 10-13. The phonon wavevector of these bulk modes is, $q_B = 4\pi n / \lambda$, where λ is the wavelength of the excitation laser and n is the refractive index of the medium [16,34].

Table 2 summarizes the peak frequency, FWHM, and the relative intensity of LA to TA modes for all diamond samples.

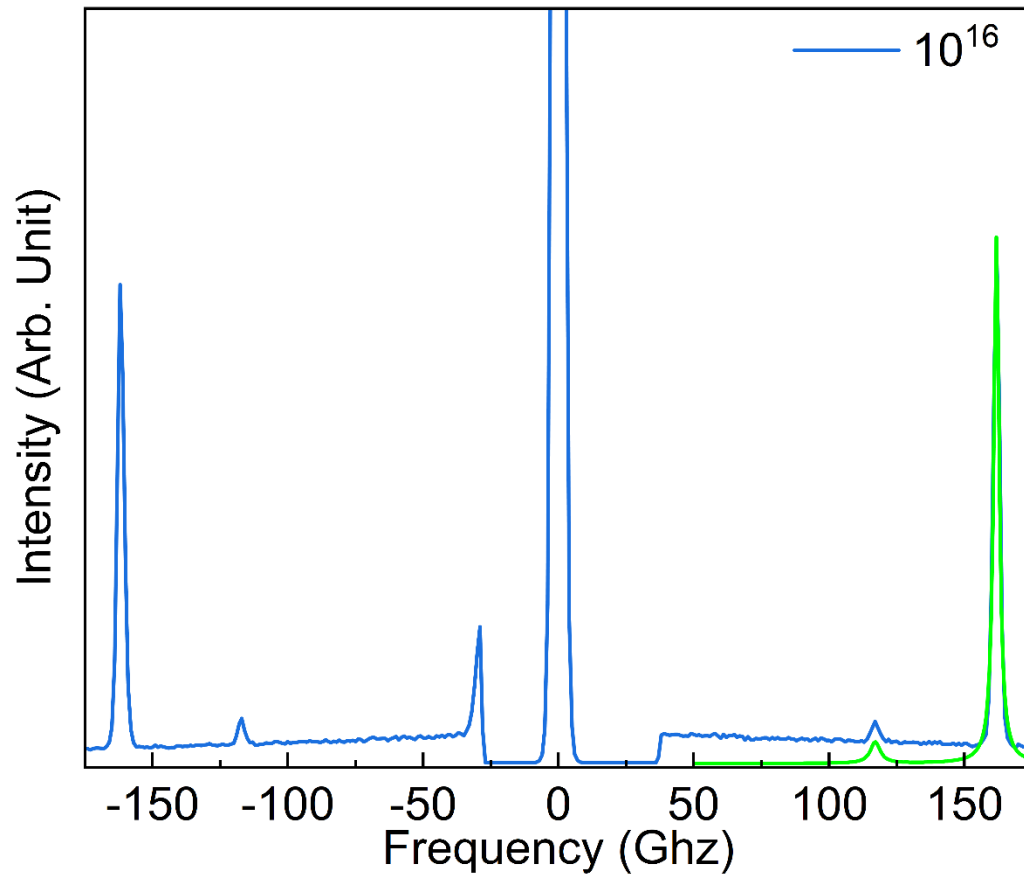


Figure 11: Lorentzian fitting of the bulk Brillouin light spectra of the boron-doped diamond samples with boron concentration of 10^{16} cm^{-3} . The Lorentzian fitting is shown as a green overlay on the spectra.

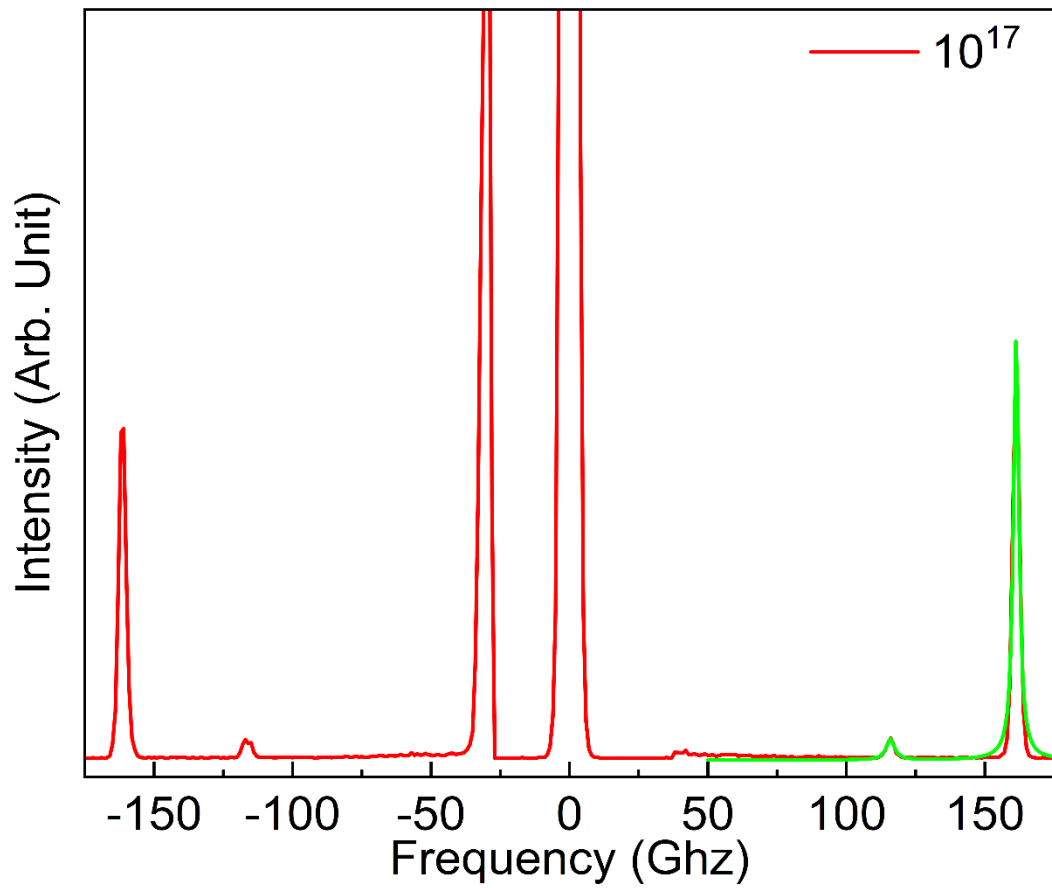


Figure 12: Lorentzian fitting of the bulk Brillouin light spectra of the boron-doped diamond samples with boron concentration of 10^{17} cm^{-3} . The Lorentzian fitting is shown as a green overlay on the spectra.

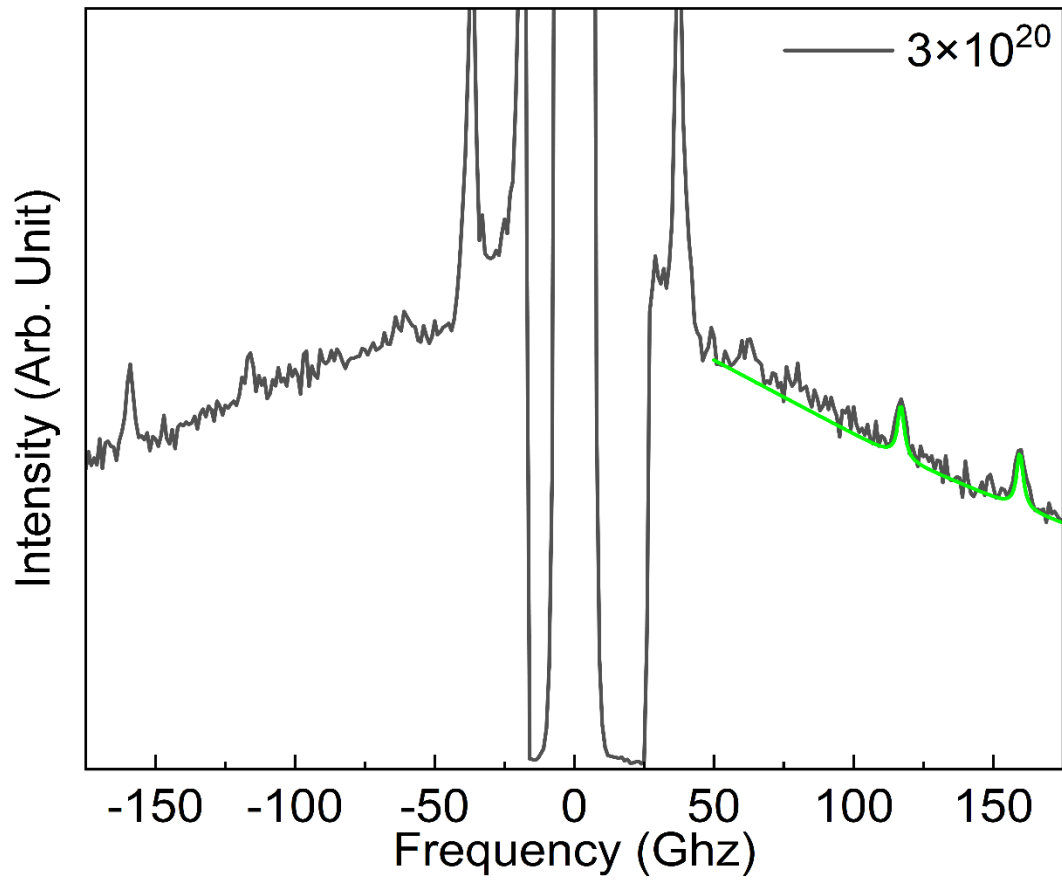


Figure 13: Lorentzian fitting of the bulk Brillouin light spectra of the boron-doped diamond samples with boron concentration of $3 \times 10^{20} \text{ cm}^{-3}$. The Lorentzian fitting is shown as a green overlay on the spectra.

Table 2: Spectral position, FWHM, and relative intensity of BMS peaks in undoped diamond and in the three boron doped diamond samples

Boron Doping (cm^{-3})	f_{TA} (GHz)	FWHM_{TA} (GHz)	f_{LA} (GHz)	FWHM_{LA} (GHz)	I_{LA}/I_{TA}
HPHT	117.9	2.3	162.4	2.7	16.7
10^{16}	117.1	4.4	161.9	2.4	24.8
10^{17}	115.9	3.5	161.3	2.3	20.5
3×10^{20}	116.9	2.9	159.5	2.6	1.0

It follows from the data in Table 2 that the LA and TA phonon modes experience softening with an increase in the boron doping level. The LA phonons have a frequency of 162.4 GHz in the undoped HPHT sample. It decreases to 159.5 GHz in the diamond with the highest boron concentration. The frequency of the TA phonons decreases from 117.9 to 116.9 GHz as the boron concentration increases. The FWHM of the peaks does not reveal a clear trend. The latter could be attributed to large experimental uncertainty in determining FWHM. An intriguing observation is that the relative intensity of the LA phonon peak with respect to the TA phonon, I_{LA}/I_{TA} , decreases substantially for the highest-doped diamond. In optically isotropic materials and in the backscattering BMS configuration, the spectral power scattered by TA phonons falls to zero and therefore the spectrum is dominated by the LA peak [34]. In our results, this is the case for the low and medium doped diamond samples. However, in high-boron-doped diamond, the scattering intensity of the LA peaks is suppressed significantly, becoming even weaker than the associated TA peak. Given that

the I_{LA}/I_{TA} ratio in the BMS strongly depends on the boron concentration, one can use this parameter to determine the local boron doping with a spatial resolution of 25 μm and 1 μm using the regular- and micro-BMS systems, respectively.

Knowing the frequency of the phonon modes, f , and the probed phonon wavevector, q_B , one can also obtain the phase velocity, v_p , of the phonons as $v_p = 2\pi f/q_B$. Note that since the dispersion of acoustic phonons close to the Brillouin zone center is linear, i.e., $\omega = qv_p$, the phase velocity, $v_p = \omega/q$, and the group velocity, $v_g = \partial\omega/\partial q$, of the fundamental LA and TA acoustic phonons are essentially the same, i.e., $v_p = v_g$. In our experiments, the direction of the examined phonon wavevector lies close to the [001] real-space crystallographic direction with a deviation angle of θ^* from the [001] direction. The deviation angle can be calculated using Snell's law, as $\sin(\theta^*) = \sin(\theta)/n$, in which n is the diamond's index of refraction and $\theta = 20^\circ$ is the incident angle fixed for all measurements. The characteristics of acoustic phonons depend on the crystallographic direction, and thus possible changes due to θ^* should be considered. The change in the refractive index of the boron-doped diamond samples due to the boron dopants was measured to account for this effect (see the Methods section). For the low- and medium-doped samples, the refractive index, measured at a 515 nm wavelength, was 2.43, whereas for the highest-doped sample, it reduced slightly to 2.41. The measured values of n and the respective deviation angle and the calculated group velocity of TA and LA phonons are summarized in Table 3. The calculated values for the reference HPHT sample are in good agreement with the reported data in the literature [18,21]. Note that the calculated values

of v_g may inherit some error due to the measurement of n at a wavelength slightly different from that used in BMS experiments. A similar variation in n is expected at the laser excitation wavelength used in BMS. From these data, one can see that the group velocity of TA and LA phonons decreases with the boron incorporation. To further support our conclusions and reduce the uncertainty due to measurements of n , θ^* and Lorentzian fitting, which are always present in experiments with bulk phonons, the characteristics of the surface acoustic phonons were examined closely in the undoped and doped diamond samples.

Table 3: The index of refraction at 515 nm, deviation angle, and group velocity of the TA and LA modes in undoped diamond and boron doped diamond samples

Boron Doping (cm^{-3})	n @ 515 nm	θ^* (degrees)	$v_{g,TA}$ (ms^{-1})	$v_{g,LA}$ (ms^{-1})
HPHT	2.3812*	8.26	13170.42	18141.44
10^{16}	2.43	8.09	12844.56	17713.95
10^{17}	2.43	8.09	12678.35	17650.52
3×10^{20}	2.41	8.17	12683.75	17651.62
* Ref. ³⁵				

In BMS experiments, light can also be scattered by the propagating surface ripples caused by the displacement fields of surface phonons or reflected bulk phonons from the interfaces [16,34,36]. In this scattering mechanism, the phonon wavevector, defined as $q_{\parallel} = 4\pi \sin(\theta)/\lambda$, lies parallel to the surface of the sample. This wavevector only depends on the light incident angle, θ , and the wavelength of the excitation laser in vacuum, λ . The change in the incidence angle, θ , changes the frequency of the surface phonons owing to the variation in the phonon wavevector; the frequency of the bulk phonons remains almost constant. It is important to note that in the case of the surface phonons, the probing phonon wavevector is no longer a function of the refractive index, n . For this reason, all of the uncertainties, associated with the calculation of the velocities for bulk phonons and deviation angles from the high-symmetry [001] crystallographic direction, are eliminated. Figure 14 presents the results of the surface Brillouin scattering measurements performed at a constant incident angle of $\theta = 75^\circ$. The calculated in-plane phonon wavevector is $q_{\parallel} =$

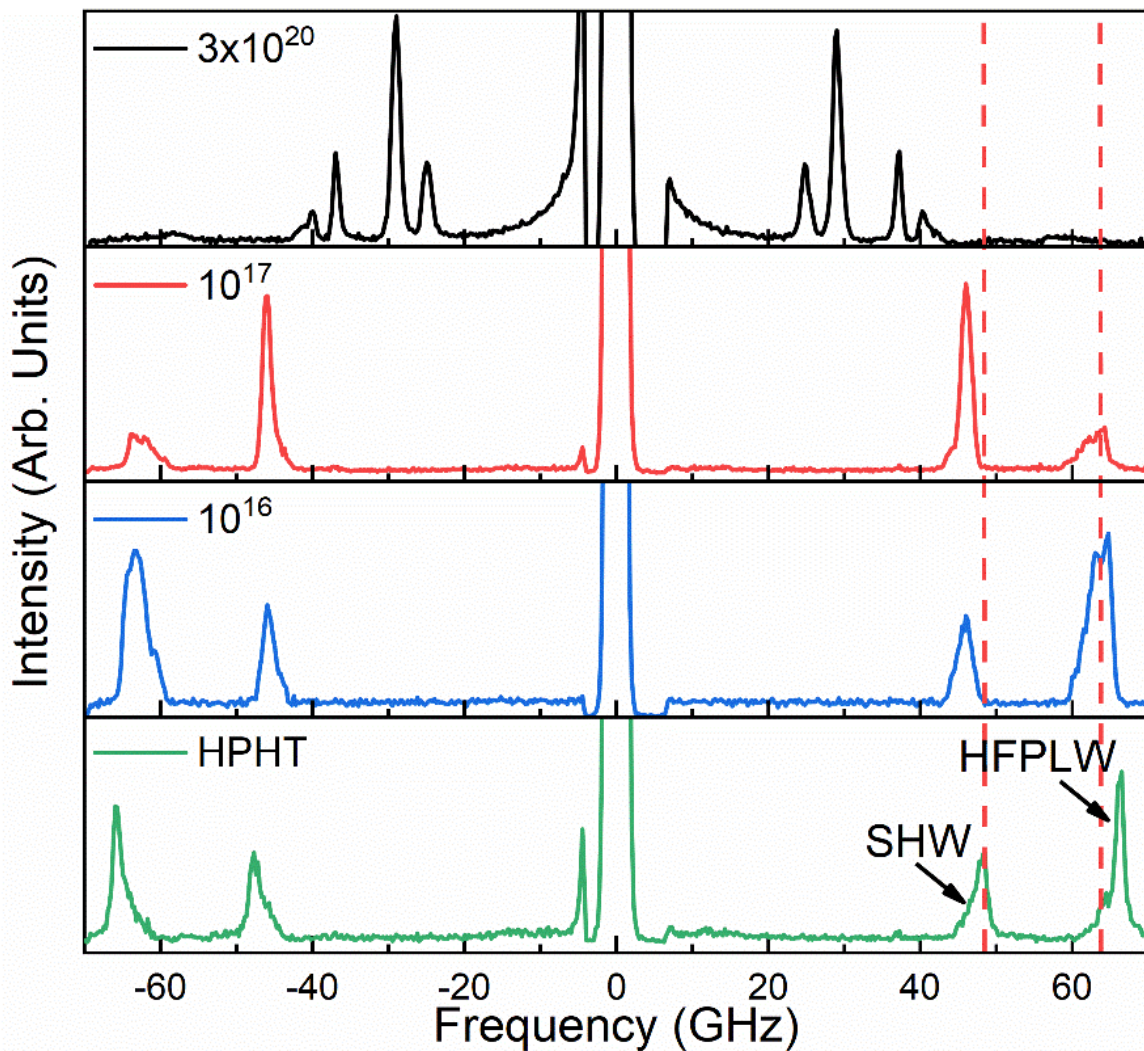


Figure 14: Brillouin light scattering spectra of the boron-doped diamond samples and a reference HPHT diamond substrate accumulated at $\theta=75^\circ$. The shear-horizontal surface wave and high-frequency pseudo-longitudinal wave are labeled as SHW and HFPLW, respectively. The frequency of types of phonons decreases as the boron concentration increases. The figure is adapted from E. Guzman et al., “Effects of Boron Doping on the Bulk and Surface Acoustic Phonons in Single-Crystal-Diamond”, ACS Appl. Mater. Interfaces 14(37) (2022) 42223-42231. Reprinted with permission from the American Chemical Society, Copyright © 2024

0.0228 nm⁻¹. Two pronounced peaks are attributed to the shear-horizontal surface wave (SHW) and high-frequency pseudo-longitudinal wave (HFPLW) [17,21]. The important observation is that the frequencies of these peaks decrease with an increasing boron doping concentration in diamond. The latter provides solid evidence for the phonon softening in the acoustic polarization branches.

The frequency, f , and the phase velocity of the SAW phonons, $v_p = 2\pi f/q_{\parallel}$, are presented as the functions of the boron concentration in Figure 15. One can see that doping the diamond with boron at a low concentration of 10^{16} cm⁻³ makes the phase velocity of both phonon branches to decrease as compared to that of the undoped reference HPHT diamond. Additional doping of the diamond sample up to 10^{17} cm⁻³ does not strongly affect the phonon velocity. However, for the heavily doped diamond, with a boron concentration of 3×10^{20} cm⁻³, another strong decrease in the phase velocity is observed. This nonmonotonic trend is similar to what has been reported previously by some of us for the phonon softening in the doped alumina samples [37]. In the alumina, the low mass and small radius aluminum (Al) atoms were substituted with the heavy and large radius neodymium (Nd) atoms. In the boron-doped diamond, the situation is different. On the atomic scale, boron is slightly lighter than carbon, i.e., $m_B/m_C \sim 0.91$, and therefore, the variation in mass cannot explain the observed phonon softening. However, boron's radius is slightly bigger than that of carbon, $R_B/R_C \sim 1.3$. Therefore, a possible mechanism for the phonon softening is the lattice distortion induced by the boron atoms. This distortion, especially in the heavily doped sample, causes an increase in the “effective” crystal lattice

parameter and the atomic plane separation. This agrees well with the red shift observed in the Raman ZCP peak of diamond (see Figure 3). An independent study confirms that the lattice constant of diamond slightly increases with the boron dopant concentration and starts to vary at a higher rate as the concentration surpasses $\sim 2.7 \times 10^{20} \text{ cm}^{-3}$ [38]. Comparing the phonon phase velocity of the highly doped sample with that of the undoped HPHT diamond, one can see that the phonon velocity of the SHW and HFPLW polarization branches decreases by more than ~ 15 and $\sim 11.7\%$, respectively.

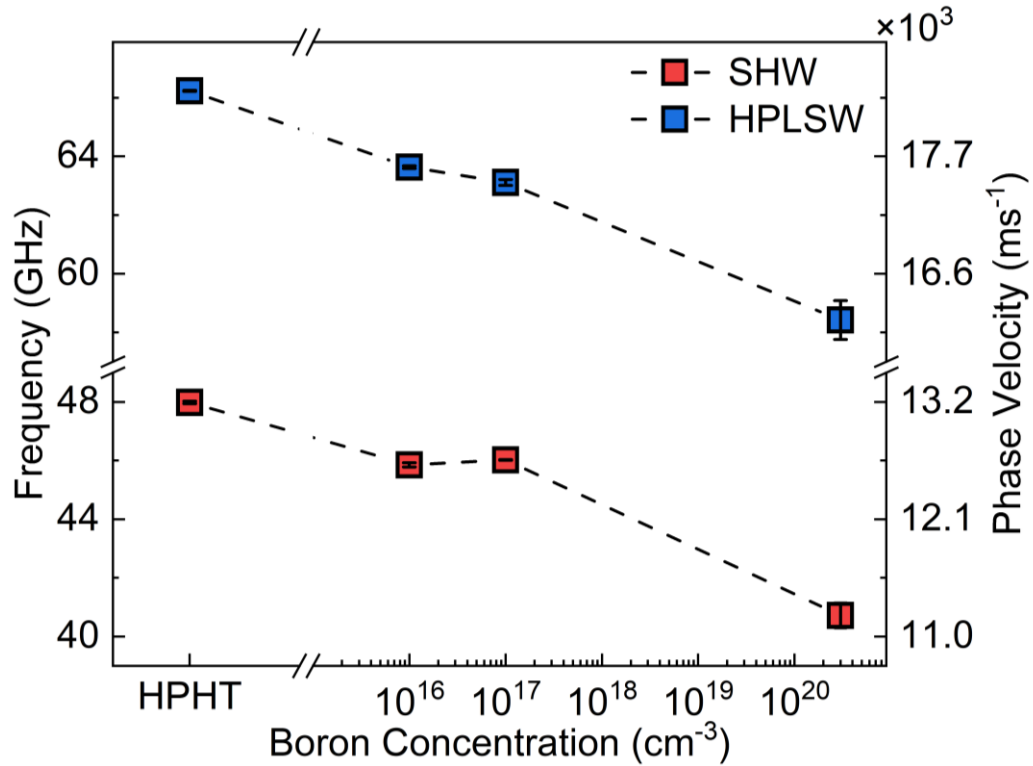


Figure 15: Frequency and velocity of surface phonons in diamond as a function of the boron doping concentration. The data for the SHW and HPLSW phonon polarization branches are shown at $q_{\parallel} = 0.0228 \text{ nm}^{-1}$. The figure is adapted from E. Guzman *et al.*, “Effects of Boron Doping on the Bulk and Surface Acoustic Phonons in Single-Crystal-Diamond”, ACS Appl. Mater. Interfaces 14(37) (2022) 42223-42231. Reprinted with permission from the American Chemical Society, Copyright © 2024

In diamond, the phase velocity of the HFPLW is negligibly smaller than that of the bulk LA phonons traveling in the $\langle 001 \rangle$ direction [18]. The observed reduction in v_p of the HFPLW with the boron doping concentration points out that the phase velocity and correspondingly the group velocity of the respective LA phonon polarization branch experience similar softening. Such a reduction has important implications for the thermal and mechanical properties of boron-doped diamond. The phase velocity of SHW and HFPLW in diamond can be estimated from the equations $v_{SHW} = (c_{66}/\rho)^{1/2}$ and $v_{HFPLW} = (c_{11}/\rho)^{1/2}$, respectively, where ρ is the mass density [18]. Note that the phase velocities of SHW and HFPLW phonons depend only on one elasticity constant. Therefore, the elasticity parameters c_{66} and c_{11} can be directly related to the measured phase velocities of these surface acoustic waves. Assuming a constant mass density for the boron-doped diamond samples, one can infer that the elastic constants decrease with boron addition, in line with the previously reported values obtained by other techniques [39,40].

2.3.2 Modeling

Phonon band structure calculations were performed using the density functional theory (DFT) implemented in the Quantum Espresso 7.0 package [41] to investigate the effect of B-doping on the phonon energy dispersion in diamond. The details of the calculations can be found in the Methods section. A cube supercell containing eight atoms was used in the DFT calculations. For B-doped diamond, one of the C atoms was replaced by B, equivalent to the $\sim 2 \times 10^{22} \text{ cm}^{-3}$ doping concentration. The structure of the supercells for the pristine and B-doped diamond can be seen in Figure 17. To validate our modeling approach, the phonon dispersion of pure diamond was calculated using an FCC unit cell containing two carbon atoms with an experimental lattice constant of 3.57 Å. The computational results were compared with the experimental data from Ref [42]. The data presented in Figure 16 indicate an excellent agreement between the calculated and experimental phonon frequencies.

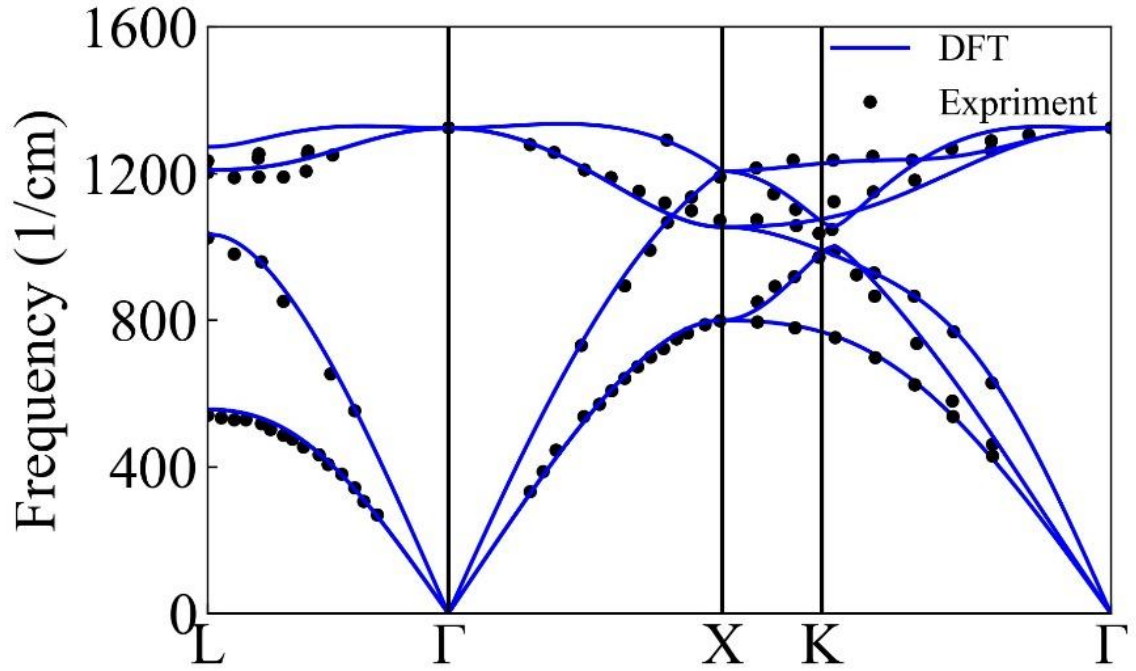


Figure 16: Phonon dispersion of pristine diamond calculated by density-functional-theory (DFT). The computational results are in excellent agreement with the experimental results (black dots) obtained by neutron scattering.⁴²

After relaxation, the optimized lattice constants were obtained to be 3.54 and 3.60 Å for pristine and B-doped diamond supercells, respectively. The obtained lattice constant of pristine diamond agrees well with the measured lattice constant of 3.57 Å [38]. The model of the supercell structure can be seen in Figure 17. Figure 19 shows the calculated phonon dispersion of pristine diamond in comparison with that of the B-doped diamond with a boron concentration of $\sim 2 \times 10^{22} \text{ cm}^{-3}$. Since the supercell and thus smaller Brillouin zone was used, all phonon bands are folded back in the reciprocal space. To make the phonon dispersion easier to understand, the supercell dispersion was unfolded using the phonon unfolding package [43]. As a result, the phonon dispersion of pristine diamond is

completely reproduced and the excess phonon modes at high-symmetry points for both pristine and B-doped diamond have been almost completely removed. As seen in Figure 18, both the LA and TA phonon modes undergo softening as a result of the doping. The group velocity of LA and TA phonons was calculated near the BZ center for the pristine diamond and several values of boron concentrations. Note that a higher boron concentrations was intentionally assumed in the simulations to keep the size of the supercell and the cost of calculations reasonable. The results are presented in Figure 19. The calculated phonon velocities in pristine diamond for LA and TA modes along the Γ -X direction and close to the BZ center are 17,494 and 12,388 ms^{-1} , respectively. The obtained values agree well with our experimental measurements for the undoped HPHT diamond. In the B-doped diamond, the velocity for the LA and TA phonons decreases substantially. The change in the group velocity of the LA polarization branch is more pronounced compared to that of the TA mode, which is in qualitative agreement with our experimental observation. Note that since 2-orders-of-magnitude higher boron concentration were considered in our simulations, a direct quantitative comparison of the velocities was not made.

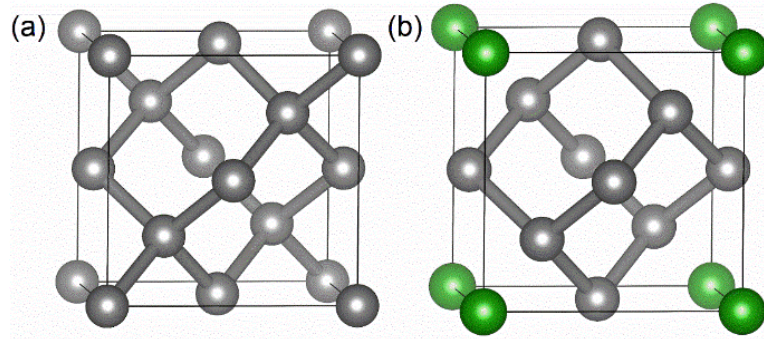


Figure 17: (a-b) The supercell structure of the pristine and the B-doped diamond. The grey and green spheres represent C and B atoms, respectively.

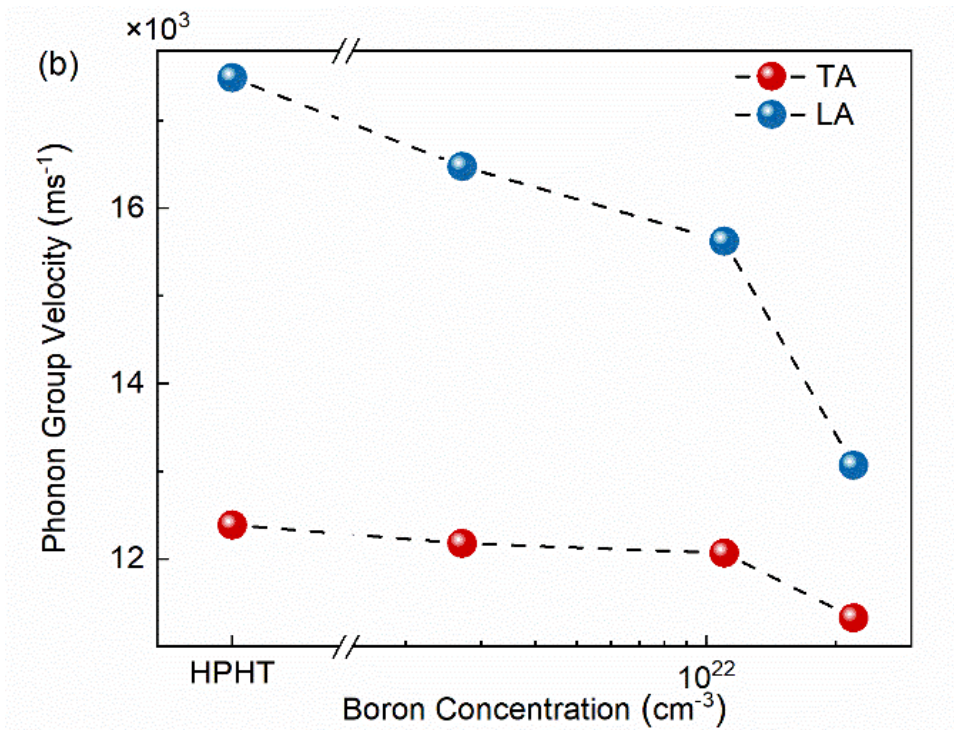


Figure 18: The phonon group velocity of TA and LA modes close to the BZ center for pristine and B-doped diamond as a function of the boron concentration. The softening of all acoustic phonon modes because of boron doping is clearly observed. Note that a substantially higher concentration of B atoms was intentionally assumed to keep the supercell reasonably small in the calculations. The figure is adapted from E. Guzman *et al.*, “Effects of Boron Doping on the Bulk and Surface Acoustic Phonons in Single-Crystal-Diamond”, ACS Appl. Mater. Interfaces 14(37) (2022) 42223-42231. Reprinted with permission from the American Chemical Society, Copyright © 2024

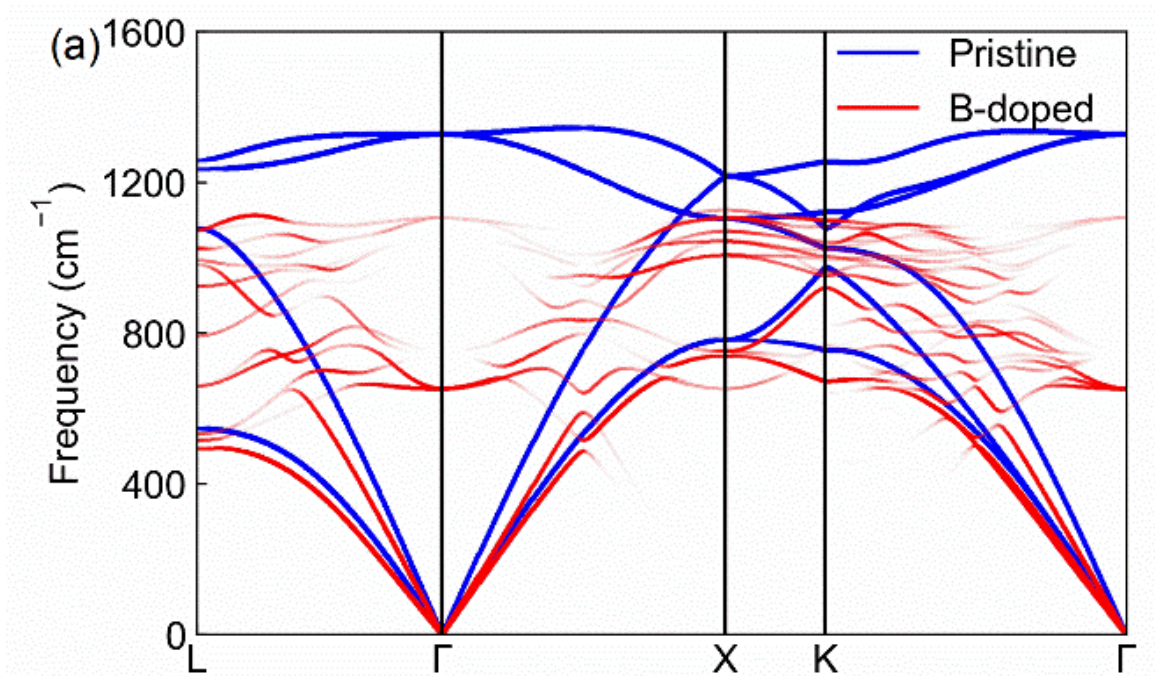


Figure 19: The calculated phonon band structure of the pristine (blue) and B-doped (red) diamond. The figure is adapted from E. Guzman *et al.*, “Effects of Boron Doping on the Bulk and Surface Acoustic Phonons in Single-Crystal-Diamond”, ACS Appl. Mater. Interfaces 14(37) (2022) 42223-42231. Reprinted with permission from the American Chemical Society, Copyright © 2024

2.4 Discussion

The phonon softening has interesting and important implications for thermal transport and related properties. Conventional theories of the thermal conductivity of semiconductor and insulating materials assume that doping does not modify the group velocity, v_g , of the acoustic phonons [44-46]. The dopants act as an extra point defect scattering centers for the acoustic phonons, which retain their properties the same as in the intrinsic material. However, if the phonon group velocity changes as a result of the doping, one needs to take it into account in the calculations [47]. In the kinetic theory, the phonon thermal conductivity can be expressed as $K = (1/3) C v_g \Lambda = (1/3) C v_g^2 \tau$, where C is the volumetric heat capacity, v_g is the average phonon group velocity, Λ is the phonon “gray” mean-free path, and τ is the combined phonon relaxation time, i.e., lifetime. The phonon relaxation time is defined by the scattering rate in different types of processes; it can be expressed as $\tau^{-1} = \tau_U^{-1} + \tau_d^{-1} + \tau_{e-ph}^{-1}$. Here, τ_U^{-1} , τ_d^{-1} , and τ_{e-ph}^{-1} are the phonon–phonon Umklapp scattering rate due to the crystal anharmonicity, phonon–defect scattering rate, and the electron–phonon scattering rate, respectively. The scattering rates are the function of both phonon frequency, ω , and phonon group velocity, v_g . The phonon–defect scattering, which includes scattering on dopant atoms, is the dominant mechanism at low temperatures [48]. Given the high Debye temperature of diamond ($\theta_D \sim 1870$ K), the phonon–defect scattering makes a significant contribution even at room temperature (RT). The phonon softening alters the thermal conductivity, K , not only via the combined relaxation time, τ , but also via the volumetric heat capacity, C , which is proportional to v_g^{-3} . The dependence on the

phonon group velocity is due to the phonon density of states. The previously reported data on the heat capacity of boron-doped single-crystal HPHT diamond support our arguments [49]. In this study, the doped diamond samples with higher boron concentration revealed higher heat capacity. The authors have interpreted their observation as a possible inclusion of metallic particles during the growth process and thus the dominance of electron heat capacity at low temperatures [49]. However, their data can also be explained by the lower phonon group velocity. One should remember that in the bulk crystals the phonon group velocity is the same as the phonon phase velocity, and the observed reduction in the phonon velocity is equivalent for both.

The strongest effect from the phonon softening on thermal conductivity near RT is expected via the changes in the phonon–defect scattering rate. The average phonon group velocity for all three acoustic polarization branches is given by the expression.

$$V_g = 3 \left[(1/v_{T,1}) + (1/v_{T,2}) + (1/v_L) \right]^{-1} \quad (1)$$

Here, $v_{T,1}$ and $v_{T,2}$ are the phonon group velocities for two TA phonon polarization branches, and v_L is the LA phonon group velocity. Given that in diamond transverse acoustic phonons along the $\langle 001 \rangle$ direction are degenerate, our experimental data show

that all velocities that enter Eq. (1) experience a reduction in their values. The phonon scattering rate on point defects, like dopant atoms, is given as [51,52]

$$\tau_P^{-1} = (V_0 \Gamma \omega^4 / 4\pi v_g^3) \quad (2)$$

Here, V_0 is the volume per atom, and Γ is the scattering parameter, which depends linearly on the defect concentration. Γ is a measure of the point defect scattering strength [53,54]. If the properties of phonons had not changed, the increase in this scattering rate would be only due to the increase in the concentration of dopant atoms. As a result of the reduction in the phonon velocity, v_g , the effect of the doping becomes stronger and likely dependent on the crystallographic direction.

It is also illustrative to consider the effect of the acoustic phonon softening for dislocation scattering. At a high density of doping, the dopant atoms may form clusters of atoms that act similar to dislocation lines. The phonon scattering rate on dislocation lines is given as [50,55]:

$$\tau_E^{-1} = (2^{1.5} / 3^{3.5}) \eta N_D^E b_E^2 \gamma^2 \omega \{ (1/2) + (1/24) \times \\ \times [(1 - 2\nu)/(1 - \nu)]^2 [1 + \sqrt{2}(v_L/v_T)^2]^2 \} \quad (3)$$

Here, N_D^E and b_E are the density and magnitude of Burgers vectors for the edge dislocations, respectively, η accounts for the orientation of the dislocation lines with respect to the direction of temperature gradient. γ and ν are the Grüneisen anharmonicity parameter and Poisson ratio, respectively. One can see from eq 3 that even a relative reduction in the phonon velocity for the LA and TA phonons can play a role since the scattering rate depends on $\sim(v_L/v_T)^4$. The discussed dependencies result in intricate effects of phonon softening on heat conduction in diamond. They can lead to a stronger reduction in the thermal conductivity than the predictions of simple theory that does not account for the changes in the phonon velocity or more pronounced anisotropy in thermal conductivity if the dopant atoms have some preferential arrangements.

The effects of phonon softening on thermal conductivity are not limited to acoustic phonons alone. Indeed, the contribution of the optical phonons to the phonon thermal conductivity of diamond is negligible owing to their high frequency and small group velocity [56,57]. However, optical phonons provide scattering channels for the acoustic phonon branches [9]. The broadening of the ZCP peak in the highly doped diamond sample indicates a shortened phonon lifetime due to the increased contribution of boron atoms to the phonon scattering processes via point defects and electron–phonon processes. One can estimate the decay rate of the longitudinal optical (LO) phonons at the Brillouin zone center ($q = 0$) using Klemens' formula $\tau^{-1} \sim \delta\omega$, where τ is the phonon lifetime and $\delta\omega$ is the FWHM of the Raman ZCP peak [57,58]. The estimated values of τ for the undoped HPHT and the low- and medium-doped diamond samples are ~ 11 ps, which is close to the measured lifetime of phonons in single-crystal diamond using other techniques [59]. Our

data show that this value decreases to ~ 3.7 ps for the highly doped sample, significantly lower than that of the HPHT and other lightly doped diamond samples. This reduction can be correlated well with the measured reduction in thermal conductivity.

2.5 Conclusions

The bulk and surface acoustic phonons were investigated in the boron-doped single-crystal diamond films using the Brillouin–Mandelstam light scattering spectroscopy. It was found that the frequency and the group velocity of acoustic phonons decrease nonmonotonically with the increasing boron doping concentration, revealing pronounced phonon softening. As a result of boron doping, the velocity of the bulk longitudinal and transverse acoustic phonons decreased correspondingly. The frequency of the optical phonons was unaffected at low boron concentration but experienced a strong decrease at the high doping level. Density functional theory was also performed to calculate the phonon band structure for the pristine and highly doped diamond. The theoretical results qualitatively confirm the phonon softening in both optical and acoustic polarization branches. The strong softening of the acoustic phonons – the main heat carriers in diamond – has important implications for thermal transport in such materials. Our results also demonstrate that the intensity ratio of the LA and TA phonons can be used to monitor the boron concentration in diamond.

2.6 References

- (1) Malakoutian, M.; Field, D. E.; Hines, N. J.; Pasayat, S.; Graham, S.; Kuball, M.; Chowdhury, S. Record-Low Thermal Boundary Resistance between Diamond and GaN-on-SiC for Enabling Radiofrequency Device Cooling. *ACS Applied Materials and Interfaces* **2021**, *13* (50), 60553–60560. <https://doi.org/10.1021/acscami.1c13833>.
- (2) Surdi, H.; Thornton, T.; Nemanich, R. J.; Goodnick, S. M. Space Charge Limited Corrections to the Power Figure of Merit for Diamond. *Applied Physics Letters* **2022**, *120* (22), 223503. <https://doi.org/10.1063/5.0087059>.
- (3) Ghosh, S.; Surdi, H.; Kargar, F.; Koeck, F. A.; Rumyantsev, S.; Goodnick, S.; Nemanich, R. J.; Balandin, A. A. Excess Noise in High-Current Diamond Diodes. *Applied Physics Letters* **2022**, *120* (6), 062103. <https://doi.org/10.1063/5.0083383>.
- (4) Tsao, J. Y.; Chowdhury, S.; Hollis, M. A.; Jena, D.; Johnson, N. M.; Jones, K. A.; Kaplar, R. J.; Rajan, S.; van de Walle, C. G.; Bellotti, E.; Chua, C. L.; Collazo, R.; Coltrin, M. E.; Cooper, J. A.; Evans, K. R.; Graham, S.; Grotjohn, T. A.; Heller, E. R.; Higashiwaki, M.; Islam, M. S.; Juodawlkis, P. W.; Khan, M. A.; Koehler, A. D.; Leach, J. H.; Mishra, U. K.; Nemanich, R. J.; Pilawa-Podgurski, R. C. N.; Shealy, J. B.; Sitar, Z.; Tadjer, M. J.; Witulski, A. F.; Wraback, M.; Simmons, J. A. Ultrawide-Bandgap Semiconductors: Research Opportunities and Challenges. *Advanced Electronic Materials* **2018**, *4* (1), 1600501. <https://doi.org/10.1002/aelm.201600501>.
- (5) Donato, N.; Rouger, N.; Pernot, J.; Longobardi, G.; Udrea, F. Diamond Power Devices: State of the Art, Modelling, Figures of Merit and Future Perspective. *Journal of Physics D: Applied Physics* **2019**, *53* (9), 093001. <https://doi.org/10.1088/1361-6463/AB4EAB>.
- (6) Surdi, H.; Koeck, F. A. M.; Ahmad, M. F.; Thornton, T. J.; Nemanich, R. J.; Goodnick, S. M. Demonstration and Analysis of Ultrahigh Forward Current Density Diamond Diodes. *IEEE Transactions on Electron Devices* **2022**, *69* (1), 254–261. <https://doi.org/10.1109/TED.2021.3125914>.
- (7) Wei, L.; Kuo, P. K.; Thomas, R. L.; Anthony, T. R.; Banholzer, W. F. Thermal Conductivity of Isotopically Modified Single Crystal Diamond. *Physical Review Letters* **1993**, *70* (24), 3764–3767. <https://doi.org/10.1103/PhysRevLett.70.3764>.
- (8) Olson, J. R.; Pohl, R. O.; Vandersande, J. W.; Zoltan, A.; Anthony, T. R.; Banholzer, W. F. Thermal Conductivity of Diamond between 170 and 1200 K and the Isotope Effect. *Physical Review B* **1993**, *47* (22), 14850–14856. <https://doi.org/10.1103/PhysRevB.47.14850>.
- (9) Ward, A.; Broido, D. A.; Stewart, D. A.; Deinzer, G. Ab Initio Theory of the Lattice Thermal Conductivity in Diamond. *Physical Review B - Condensed Matter and Materials Physics* **2009**, *80* (12), 125203. <https://doi.org/10.1103/PhysRevB.80.125203>.

- (10) Kalish, R. Doping of Diamond. *Carbon N Y* **1999**, *37* (5), 781–785. [https://doi.org/10.1016/S0008-6223\(98\)00270-X](https://doi.org/10.1016/S0008-6223(98)00270-X).
- (11) Mandal, S.; Yuan, C.; Massabuau, F.; Pomeroy, J. W.; Cuenca, J.; Bland, H.; Thomas, E.; Wallis, D.; Batten, T.; Morgan, D.; Oliver, R.; Kuball, M.; Williams, O. A. Thick, Adherent Diamond Films on AlN with Low Thermal Barrier Resistance. *ACS Applied Materials and Interfaces* **2019**, *11* (43), 40826–40834. <https://doi.org/10.1021/acsami.9b13869>.
- (12) Prikhodko, D.; Tarelkin, S.; Bormashov, V.; Golovanov, A.; Kuznetsov, M.; Teteruk, D.; Volkov, A.; Buga, S. Thermal Conductivity of Synthetic Boron-Doped Single-Crystal HPHT Diamond from 20 to 400 K. *MRS Communications* **2016**, *6* (2), 71–76. <https://doi.org/10.1557/MRC.2016.12>.
- (13) Prikhodko, D.; Tarelkin, S.; Bormashov, V.; Golovanov, A.; Kuznetsov, M.; Teteruk, D.; Kornilov, N.; Volkov, A.; Buga, A. Low Temperature Thermal Conductivity of Heavily Boron-Doped Synthetic Diamond: Influence of Boron-Related Structure Defects. *Journal of Superhard Materials* *2019* *41:1* **2019**, *41* (1), 24–31. <https://doi.org/10.3103/S1063457619010039>.
- (14) Williams, G.; Calvo, J. A.; Faili, F.; Dodson, J.; Obeloer, T.; Twitchen, D. J. Thermal Conductivity of Electrically Conductive Highly Boron Doped Diamond and Its Applications at High Frequencies. *Proceedings of the 17th InterSociety Conference on Thermal and Thermomechanical Phenomena in Electronic Systems, ITherm 2018* **2018**, 235–239. <https://doi.org/10.1109/ITHERM.2018.8419493>.
- (15) Ding, M.; Liu, Y.; Lu, X.; Li, Y.; Tang, W. Boron Doped Diamond Films: A Microwave Attenuation Material with High Thermal Conductivity. *Applied Physics Letters* **2019**, *114* (16), 162901. <https://doi.org/10.1063/1.5083079>.
- (16) Kargar, F.; Balandin, A. A. Advances in Brillouin–Mandelstam Light-Scattering Spectroscopy. *Nature Photonics* **2021**, *15* (10), 720–731. <https://doi.org/10.1038/s41566-021-00836-5>.
- (17) Djemia, P.; Tallaire, A.; Achard, J.; Silva, F.; Gicquel, A. Elastic Properties of Single Crystal Diamond Made by CVD. *Diamond and Related Materials* **2007**, *16* (4–7), 962–965. <https://doi.org/10.1016/J.DIAMOND.2006.11.029>.
- (18) Djemia, P.; Dugautier, C.; Chauveau, T.; Dogheche, E.; de Barros, M. I.; Vandembulcke, L. Mechanical Properties of Diamond Films: A Comparative Study of Polycrystalline and Smooth Fine-Grained Diamonds by Brillouin Light Scattering. *Journal of Applied Physics* **2001**, *90* (8), 3771–3779. <https://doi.org/10.1063/1.1402667>.
- (19) Grimsditch, M. H.; Ramdas, A. K. Brillouin Scattering in Diamond. *Physical Review B* **1975**, *11* (8), 3139–3148. <https://doi.org/10.1103/PhysRevB.11.3139>.
- (20) Jiang, X.; Harzer, J. v.; Hillebrands, B.; Wild, Ch.; Koidl, P. Brillouin Light Scattering on Chemical-Vapor-Deposited Polycrystalline Diamond: Evaluation of the

Elastic Moduli. *Applied Physics Letters* **1991**, *59* (9), 1055–1057. <https://doi.org/10.1063/1.106343>.

(21) Xie, Y. R.; Ren, S. L.; Gao, Y. F.; Liu, X. L.; Tan, P. H.; Zhang, J. Measuring Bulk and Surface Acoustic Modes in Diamond by Angle-Resolved Brillouin Spectroscopy. *Science China: Physics, Mechanics and Astronomy* **2021**, *64* (8), 287311. <https://doi.org/10.1007/s11433-020-1710-6>.

(22) Turin, V. O.; Balandin, A. A. Electrothermal Simulation of the Self-Heating Effects in GaN-Based Field-Effect Transistors. *Journal of Applied Physics* **2006**, *100* (5), 054501. <https://doi.org/10.1063/1.2336299>.

(23) Ramamurti, R.; Becker, M.; Schuelke, T.; Grotjohn, T. A.; Reinhard, D. K.; Asmussen, J. Deposition of Thick Boron-Doped Homoepitaxial Single Crystal Diamond by Microwave Plasma Chemical Vapor Deposition. *Diamond and Related Materials* **2009**, *18* (5–8), 704–706. <https://doi.org/10.1016/J.DIAMOND.2009.01.031>.

(24) Demlow, S. N.; Rechenberg, R.; Grotjohn, T. The Effect of Substrate Temperature and Growth Rate on the Doping Efficiency of Single Crystal Boron Doped Diamond. *Diamond and Related Materials* **2014**, *49*, 19–24. <https://doi.org/10.1016/J.DIAMOND.2014.06.006>.

(25) Mortet, V.; Gregora, I.; Taylor, A.; Lambert, N.; Ashcheulov, P.; Gedeonova, Z.; Hubik, P. New Perspectives for Heavily Boron-Doped Diamond Raman Spectrum Analysis. *Carbon N Y* **2020**, *168*, 319–327. <https://doi.org/10.1016/J.CARBON.2020.06.075>.

(26) Praver, S.; Nemanich, R. J. Raman Spectroscopy of Diamond and Doped Diamond. *Philosophical Transactions of the Royal Society of London. Series A: Mathematical, Physical and Engineering Sciences* **2004**, *362* (1824), 2537–2565. <https://doi.org/10.1098/RSTA.2004.1451>.

(27) Ferrari, A. C.; Robertson, J. Resonant Raman Spectroscopy of Disordered, Amorphous, and Diamondlike Carbon. *Physical Review B* **2001**, *64* (7), 075414. <https://doi.org/10.1103/PhysRevB.64.075414>.

(28) Mortet, V.; Živcová, Z. V.; Taylor, A.; Davydová, M.; Frank, O.; Hubik, P.; Lorincik, J.; Aleshin, M. Determination of Atomic Boron Concentration in Heavily Boron-Doped Diamond by Raman Spectroscopy. *Diamond and Related Materials* **2019**, *93*, 54–58. <https://doi.org/10.1016/j.diamond.2019.01.028>.

(29) Menéndez, J.; Cardona, M. Temperature Dependence of the First-Order Raman Scattering by Phonons in Si, Ge, and -Sn: Anharmonic Effects. *Physical Review B* **1984**, *29* (4), 2051–2059. <https://doi.org/10.1103/PhysRevB.29.2051>.

(30) Balkas, C.; Shin, H.; Davis, R.; Nemanich, R. Raman Analysis of Phonon Lifetimes in AlN and GaN of Wurtzite Structure. *Physical Review B N*. **1999**, *59* (20), 12977–12982. <https://doi.org/10.1103/PhysRevB.59.12977>.

- (31) Piscanec, S.; Cantoro, M.; Ferrari, A. C.; Zapien, J. A.; Lifshitz, Y.; Lee, S. T.; Hofmann, S.; Robertson, J. Raman Spectroscopy of Silicon Nanowires. *Physical Review B - Condensed Matter and Materials Physics* **2003**, *68* (24), 241312–242003. <https://doi.org/10.1103/PhysRevB.68.241312>.
- (32) Kargar, F.; Debnath, B.; Kakko, J.-P.; Saÿnätjoki, A.; Lipsanen, H.; Nika, D. L.; Lake, R. K.; Balandin, A. A. Direct Observation of Confined Acoustic Phonon Polarization Branches in Free-Standing Semiconductor Nanowires. *Nature Communications* **2016**, *7*, 13400. <https://doi.org/10.1038/ncomms13400>.
- (33) Huang, C. Y. T.; Kargar, F.; Debnath, T.; Debnath, B.; Valentin, M. D.; Synowicki, R.; Schoeche, S.; Lake, R. K.; Balandin, A. A. Phononic and Photonic Properties of Shape-Engineered Silicon Nanoscale Pillar Arrays. *Nanotechnology* **2020**, *31* (30), 30LT01. <https://doi.org/10.1088/1361-6528/ab85ee>.
- (34) Sandercock, J. R. Trends in Brillouin Scattering: Studies of Opaque Materials, Supported Films, and Central Modes. In *Light Scattering in Solids III. Topics in Applied Physics*; Cardona, M., Güntherodt, G., Eds.; Springer: Berlin, Heidelberg, 1982; Vol. 51, pp 173–206. https://doi.org/10.1007/3540115137_6.
- (35) Zaitsev, A. M. *Optical Properties of Diamond*; Springer Berlin Heidelberg: Berlin, Heidelberg, 2001. <https://doi.org/10.1007/978-3-662-04548-0>.
- (36) Mutti, P.; Bottani, C. E.; Ghislotti, G.; Beghi, M.; Briggs, G. A. D.; Sandercock, J. R. Surface Brillouin Scattering—Extending Surface Wave Measurements to 20 GHz. In *Advances in Acoustic Microscopy*; Briggs, A., Ed.; Advances in Acoustic Microscopy; Springer: Boston, MA, 1995; Vol. 1, pp 249–300. https://doi.org/10.1007/978-1-4615-1873-0_7.
- (37) Kargar, F.; Penilla, E. H.; Aytan, E.; Lewis, J. S.; Garay, J. E.; Balandin, A. A. Acoustic Phonon Dispersion Engineering in Bulk Crystals via Incorporation of Dopant Atoms. *Applied Physics Letters* **2018**, *112* (19), 191902. <https://doi.org/10.1063/1.5030558>.
- (38) Brunet, F.; Germi, P.; Pernet, M.; Deneuille, A.; Gheeraert, E.; Laugier, F.; Burdin, M.; Rolland, G. The Effect of Boron Doping on the Lattice Parameter of Homoepitaxial Diamond Films. *Diamond and Related Materials* **1998**, *7* (6), 869–873. [https://doi.org/10.1016/s0925-9635\(97\)00316-6](https://doi.org/10.1016/s0925-9635(97)00316-6).
- (39) Liu, X.; Chang, Y. Y.; Tkachev, S. N.; Bina, C. R.; Jacobsen, S. D. Elastic and Mechanical Softening in Boron-Doped Diamond. *Scientific Reports* **2017**, *7* (1), 42921. <https://doi.org/10.1038/srep42921>.
- (40) Wang, X.; Shen, X.; Sun, F.; Shen, B. Influence of Boron Doping Level on the Basic Mechanical Properties and Erosion Behavior of Boron-Doped Micro-Crystalline Diamond (BDMCD) Film. *Diamond and Related Materials* **2017**, *73*, 218–231. <https://doi.org/10.1016/J.DIAMOND.2016.09.025>.

- (41) Giannozzi, P.; Baroni, S.; Bonini, N.; Calandra, M.; Car, R.; Cavazzoni, C.; Ceresoli, D.; Chiarotti, G. L.; Cococcioni, M.; Dabo, I.; Dal Corso, A.; de Gironcoli, S.; Fabris, S.; Fratesi, G.; Gebauer, R.; Gerstmann, U.; Gougoussis, C.; Kokalj, A.; Lazzeri, M.; Martin-Samos, L.; Marzari, N.; Mauri, F.; Mazzarello, R.; Paolini, S.; Pasquarello, A.; Paulatto, L.; Sbraccia, C.; Scandolo, S.; Sclauzero, G.; Seitsonen, A. P.; Smogunov, A.; Umari, P.; Wentzcovitch, R. M. QUANTUM ESPRESSO: A Modular and Open-Source Software Project for Quantum of Materials. *Journal of Physics: Condensed Matter* **2009**, *21* (39), 395502. <https://doi.org/10.1088/0953-8984/21/39/395502>.
- (42) Warren, J. L.; Yarnell, J. L.; Dolling, G.; Cowley, R. A. Lattice Dynamics of Diamond. *Physical Review* **1967**, *158* (3), 805–808. <https://doi.org/https://doi.org/10.1103/PhysRev.158.805>.
- (43) Zheng, F.; Zhang, P. Phonon Unfolding: A Program for Unfolding Phonon Dispersions of Materials. *Computer Physics Communications* **2017**, *210*, 139–144. <https://doi.org/10.1016/J.CPC.2016.09.005>.
- (44) Klemens, P. G. Thermal Conductivity and Lattice Vibrational Modes; Seitz, F., Turnbull, D., Eds.; Solid State Physics; Academic Press, 1958; Vol. 7, pp 1–98. [https://doi.org/http://dx.doi.org/10.1016/S0081-1947\(08\)60551-2](https://doi.org/http://dx.doi.org/10.1016/S0081-1947(08)60551-2).
- (45) Han, Y. J.; Klemens, P. G. Anharmonic Thermal Resistivity of Dielectric Crystals at Low Temperatures. *Physical Review B* **1993**, *48* (9), 6033–6042. <https://doi.org/10.1103/PhysRevB.48.6033>.
- (46) Callaway, J. Model for Lattice Thermal Conductivity at Low Temperatures. *Physical Review* **1959**, *113* (4), 1046. <https://doi.org/10.1103/PhysRev.113.1046>.
- (47) Balandin, A.; Wang, K. L. Significant Decrease of the Lattice Thermal Conductivity Due to Phonon Confinement in a Free-Standing Semiconductor Quantum Well. *Physical Review B* **1998**, *58* (3), 1544. <https://doi.org/10.1103/PhysRevB.58.1544>.
- (48) Liu, W. L.; Shamsa, M.; Calizo, I.; Balandin, A. A.; Ralchenko, V.; Popovich, A.; Saveliev, A. Thermal Conduction in Nanocrystalline Diamond Films: Effects of the Grain Boundary Scattering and Nitrogen Doping. *Applied Physics Letters* **2006**, *89* (17), 171915. <https://doi.org/10.1063/1.2364130>.
- (49) Tarelkin, S.; Bormashov, V.; Kuznetsov, M.; Buga, S.; Terentiev, S.; Prikhodko, D.; Golovanov, A.; Blank, V. Heat Capacity of Bulk Boron-Doped Single-Crystal HPHT Diamonds in the Temperature Range from 2 to 400 K. *Journal of Superhard Materials* **2016**, *38* (6), 412–416. <https://doi.org/10.3103/S1063457616060058>.
- (50) Zou, J.; Kotchetkov, D.; Balandin, A. A.; Florescu, D. I.; Pollak, F. H. Thermal Conductivity of GaN Films: Effects of Impurities and Dislocations. *Journal of Applied Physics* **2002**, *92* (5), 2534–2539. <https://doi.org/10.1063/1.1497704>.
- (51) Klemens, P. G. Heat Conduction in Solids by Phonons. *Thermochimica Acta* **1993**, *218*, 247–255. [https://doi.org/10.1016/0040-6031\(93\)80426-B](https://doi.org/10.1016/0040-6031(93)80426-B).

- (52) Liu, W.; Balandin, A. A. Thermal Conduction in Al_xGa_{1-x}N Alloys and Thin Films. *Journal of Applied Physics* **2005**, *97* (7), 073710. <https://doi.org/10.1063/1.1868876>.
- (53) Herring, C. Role of Low-Energy Phonons in Thermal Conduction. *Physical Review* **1954**, *95* (4), 954–965. <https://doi.org/10.1103/PhysRev.95.954>.
- (54) Slack, G. A. Effect of Isotopes on Low-Temperature Thermal Conductivity. *Physical Review* **1957**, *105* (3), 829–831. <https://doi.org/10.1103/PhysRev.105.829>.
- (55) Kotchetkov, D.; Zou, J.; Balandin, A. A.; Florescu, D. I.; Pollak, F. H. Effect of Dislocations on Thermal Conductivity of GaN Layers. *Applied Physics Letters* **2001**, *79* (26), 4316–4318. <https://doi.org/10.1063/1.1427153>.
- (56) Sparavigna, A. Influence of Isotope Scattering on the Thermal Conductivity of Diamond. *Physical Review B* **2002**, *65* (6), 064305. <https://doi.org/10.1103/PhysRevB.65.064305>.
- (57) Liu, M. S.; Bursill, L. A.; Prawer, S.; Beserman, R. Temperature Dependence of the First-Order Raman Phonon Line of Diamond. *Physical Review B* **2000**, *61* (5), 3391–3395. <https://doi.org/10.1103/PhysRevB.61.3391>.
- (58) Solin, S. A.; Ramnas, A. K. Raman Spectrum of Diamond. *Physical Review B* **1970**, *1* (4), 1687–1698. <https://doi.org/10.1103/PhysRevB.1.1687>.
- (59) Lee, K. C.; Sussman, B. J.; Nunn, J.; Lorenz, V. O.; Reim, K.; Jaksch, D.; Walmsley, I. A.; Spizzirri, P.; Prawer, S. Comparing Phonon Dephasing Lifetimes in Diamond Using Transient Coherent Ultrafast Phonon Spectroscopy. *Diamond and Related Materials* **2010**, *19* (10), 1289–1295. <https://doi.org/10.1016/J.DIAMOND.2010.06.002>.
- (60) Perdew, J. P.; Burke, K.; Ernzerhof, M. Generalized Gradient Approximation Made Simple. *Physical Review Letters* **1996**, *77* (18), 3865–3868. <https://doi.org/10.1103/PhysRevLett.77.3865>.
- (61) Baroni, S.; de Gironcoli, S.; Dal Corso, A.; Giannozzi, P. Phonons and Related Crystal Properties from Density-Functional Perturbation Theory. *Reviews of Modern Physics* **2001**, *73* (2), 515–562. <https://doi.org/10.1103/RevModPhys.73.515>.

CHAPTER 3 – OPTICAL AND ACOUSTIC PHONONS IN TURBOSTRATIC AND CUBIC BORON NITRIDE THIN FILMS ON DIAMOND SUBSTRATES

3.1 Introduction

Ultra-wide bandgap (UWBG) semiconductors are attracting increasing attention owing to their potential for applications in high-power electronics and deep ultra-violet (UV) photonics [1–8]. Materials in the UWBG category have electronic bandgaps greater than that of GaN, typically > 4 eV [1,2]. Among these materials, *c*-BN has one of the highest breakdown fields projected to be more than 8 MV cm^{-1} [9,10], a large electronic bandgap of ~ 6.4 eV [11], and high thermal conductivity of $\sim 1600 \text{ Wm}^{-1}\text{K}^{-1}$, reaching 75% of that for diamond [12]. Only diamond outperforms *c*-BN in terms of electronic, thermal, and mechanical characteristics. Intrinsic UWBGs are electrical insulators and must be doped to be used in electronic devices. Diamond has limitations with regard to doping – it can be consistently *p*-doped, but achieving reliable *n*-type doping remains challenging [1]. In contrast, *c*-BN can be conveniently doped to become an *n*-type or *p*-type semiconductor [5,9,10]. The remaining critical issue with *c*-BN is the synthesis of single- or polycrystalline thin films of phase-pure *c*-BN [13]. This task is difficult since the material favors the formation of the hexagonal sp^2 -bonded phase, either in hexagonal, *h*-BN, or turbostratic, *t*-BN forms, depending on the growth process [14,15]. The in-plane crystal structure of the *t*-BN is similar to that of *h*-BN with the difference being loss of some or all order in the out-of-plane direction [16–18]. The *t*-BN planes are stacked and rotated in

random directions along the c -axis and the interplanar distance becomes larger than that of h -BN. The planes may even have some tilt angle with respect to the plane normal [16–18]. The properties of the t -BN phase are less characterized compared to other BN phases and require in-depth investigations. There have been recent advances in the growth of c -BN thin films with high phase purity. Attempts so far have been directed towards the growth of c -BN on several substrates such as Si, Cu, Ni, and SiC/Si [15,19]. Growth of c -BN on different substrates typically requires a rather thick intermediate layer, such as h -BN or diamond, due to the lattice mismatch of the c -BN film with the underlying substrate [2]. An alternative approach is the synthesis of c -BN films directly on diamond substrates, considering the small lattice mismatch of only $\sim 1.4\%$ [20]. Recent studies have demonstrated that direct growth of c -BN on diamond substrates reduces the thickness of the h -BN intermediate phase, and in some cases, eliminates it entirely [20].

Another important advantage of the direct coupling of c -BN thin films with diamond substrates lies in their closely matched acoustic impedance, simple unit cell structures, vibrational similarity at the interface, and aligned phonon density of states [21,22]. These characteristics are crucial for efficient heat transport across adjoining interfaces which is defined by thermal boundary conductance [21]. Conventionally, the thermal boundary conductance at the interfaces is expressed using the acoustic mismatch model (AMM) or the diffuse mismatch model (DMM), respectively, in the low- and high-temperature ranges [23,24]. The acoustic impedance is defined as $\zeta = \rho v_s$ where ρ and v_s are the mass density and average phonon group velocity, respectively [24]. According to AMM, in

heterostructures with ideal interfaces, the acoustic impedance mismatch of the constituent layers determines the thermal boundary conductance at the interface [24]. The smaller the acoustic mismatch of the constituents in layered structures, then the lower will be the temperature rise at the interface for a given heat flux. Based on AMM, since the acoustic mismatch of *c*-BN with diamond is negligibly small, heat transfers efficiently at the interface with little temperature rise from the *c*-BN layer to the underlying diamond substrate [22]. However, recent studies show that thermal boundary conductance is mostly affected by the bonding strength of constituent materials at the interface and the nature of the interfacial disorder. Owing to the small lattice mismatch of *c*-BN and diamond, one expects forming strong and highly structured interfaces that enhance heat transport across their interface. In fact, theoretical studies show that the interfacial thermal conductance at *c*-BN/diamond interface can reach ten times higher than that for the Si/diamond heterostructure [22]. In this sense, the premise of the direct coupling of diamond and *c*-BN layers, which are the two UWBG materials with the highest thermal conductivity, has important implications for the ongoing challenge of efficient thermal management of high-power UWBG-based electronic devices [25].

Acoustic phonons are the main heat carriers in both *c*-BN and diamond. The phonon properties of thin films can deviate significantly from theoretical predictions depending on the film phase purity, film/substrate interfacial structure, and atomic rearrangement within the film. Moreover, the phonon dispersion can change due to phonon confinement effects in thin film structures [26,27]. The latter results in the appearance of additional phonon

modes other than the acoustic and optical phonon polarization branches in bulk materials. The contribution of these phonon modes to heat transport in thin film materials or at the interface of heterostructures is still a topic for debate [28,29]. From a theoretical perspective, the conventional AMM and DMM models typically consider only the average bulk phonon group velocity of each medium and do not account for possible effects of confined, guided, or interfacial phonon modes [30]. Recent studies have shown that interfacial phonon modes play an important role in heat conductance across the interfaces [29,31]. More importantly, the DMM fails to accurately predict the thermal conductance at the interface when two identical surfaces interface with each other [24,30]. In this case, one would expect the phonon transmission coefficient to approach one where the DMM predicts the phonon transmissivity to be 0.5 [30]. Given the negligible difference in the acoustic impedance and small lattice mismatch of *c*-BN and diamond, this pair of materials provides a convenient experimental system to investigate fundamental questions of heat transfer in thin films and across interfaces in low and high-temperature ranges. This task requires a thorough understanding of the bulk and surface phonon states of the *c*-BN films and their correlation with the film morphology, phase purity, and interlayer structure of the synthesized film on the diamond substrate.

Brillouin-Mandelstam light scattering spectroscopy (BMS) is a nondestructive optical technique that has been widely used for the detection of low-energy bulk and surface acoustic phonons in different material systems, including thin films [32–35]. This technique can determine the energy of bulk longitudinal acoustic (LA) and transverse

acoustic (TA) phonons in the vicinity of the Brillouin-zone (BZ) center. The information obtained allows for the extraction of the phonon group velocity, *i.e.*, the sound velocity of LA and TA modes which can then be used to experimentally estimate the phonon transmissivity using the acoustic mismatch or diffuse mismatch models. Moreover, the method provides the additional benefit of obtaining the dispersion of surface phonon states close to the BZ center in the specific case of thin films or opaque materials [32–34]. Together with Raman spectroscopy, the BMS technique presents a comprehensive picture of the energy distribution of both optical and acoustic phonons close to the BZ center. To the best of our knowledge, there have been no previous studies of the bulk and surface phonon states of the *t*-BN and *c*-BN phases on diamond substrates.

In this work, the visible Raman and BMS spectroscopies were used to investigate the bulk optical and acoustic phonons, as well as surface acoustic phonons, in thin films of *t*-BN grown on B-doped polycrystalline diamond, and *c*-BN films grown on B-doped single-crystalline (001) and (111) diamond substrates. The thickness and the atomic structure of the samples were first characterized using high-resolution transmission electron microscopy (HRTEM). The TEM results were correlated with the data obtained from Raman and BMS experiments. The TEM analyses show that both boron nitride thin films grown on diamond substrates contain a mixture of *c*-BN and *t*-BN phases, with the *c*-BN being the dominant phase. Our results demonstrate that while visible Raman can be used to characterize the *t*-BN phase on diamond, it does not offer sufficient information for the *c*-BN phase either due to the high concentration of defects or the overlapping of its Raman

features with that of the underlying B-doped diamond substrates. BMS, on the other hand, provides distinguishable peaks associated with the bulk longitudinal acoustic phonons of the *c*-BN phase on diamond substrates. The spectra of our angle-dependent surface Brillouin-Mandelstam scattering experiments on *c*-BN thin films exhibit peaks associated with the so-called Rayleigh surface acoustic waves. The phase velocity of Rayleigh modes is substantially higher for the *c*-BN samples on diamond (111) assessing its higher *c*-BN phase content, in agreement with the analyses acquired from HRTEM images. Our findings regarding the characteristics of surface and bulk phonons provide valuable insights into the thermal transport properties across *c*-BN and diamond interfaces, which have crucial implications for their applications in UWBG-based device applications.

3.2 Materials & Methods

The *t*-BN and *c*-BN films in this study were grown by the electron cyclotron resonance plasma-enhanced chemical vapor deposition (ECR PECVD) method [36] on various B-doped diamond substrates purchased from TISNCM and E6 vendors. The boron concentration in the substrates is estimated to be greater than 10^{20} cm⁻³. Three heterostructure samples including a *t*-BN film on polycrystalline diamond, *c*-BN film on diamond (001), and *c*-BN film on diamond (111) were investigated in this study. For simplicity, these samples are referred to as *t*-BN, *c*-BN-1, and *c*-BN-2, respectively. The *t*-BN film on the B-doped polycrystalline diamond substrate was grown with a gas flow ratio of H₂:BF₃ of 4:4 (gas flow ratio in standard cubic centimeters per minute or SCCM) at a

temperature of 735 °C for 2 hours and 30 min. The *c*-BN-1 film was grown with a ratio of H₂:BF₃ of 2:2 SCCM at a temperature of 675 °C for 2 hours and 30 min. The *c*-BN-2 film was prepared with an H₂:BF₃ ratio of 1.5:2 for 44 min and then with an H₂:BF₃ ratio of 2:2 SCCM for 2 hours and 16 min at a temperature of 735 °C for a total of 3 hours. The details of the growth process have been reported elsewhere [36].

Samples suitable for TEM observation were prepared using focused-ion-beam milling with a Thermo Fisher Helios G5-UX dual-beam system. Cross-sectional TEM images were taken using a Phillips-FEI CM-200F operated at 200 kV and an FEI Titan 80-300 operated at 300 kV.

Raman spectroscopy was conducted in the conventional backscattering configuration using a blue laser with an excitation wavelength of 488 nm. The power on the samples was 5 mW during all measurements. The laser spot diameter on the sample was ~1 μm. BMS experiments were performed in the backscattering geometry using a continuous-wave solid-state diode-pumped laser operating at the excitation wavelength of $\lambda = 532$ nm. The incident light was *p*-polarized whereas the polarization of the scattered light was not analyzed. The laser light was focused using a lens with a numerical aperture of NA=0.24. The scattered light was collected using the same lens and directed to the high-resolution high-contrast 3+3 tandem Fabry-Perot interferometer (The Table Stable, Switzerland), detector, and spectrum analyzer. To probe surface acoustic waves, samples were rotated so

the angle of the incident light can be varied between 30° to 70° with respect to the sample's surface normal.

To interpret the BMS data, one needs to determine the index of refraction, n , of the thin films at BMS laser excitation wavelength. Measurements of the refractive index were made using a Filmetrics F40-UV microscope-based spectrometer. Light with wavelengths in the range of 190 – 1100 nm was used to measure the sample reflectance. The average spot size of the light on the sample was $\sim 35 \mu\text{m}$. The thickness and optical constants of the thin films were extracted by fitting the reflectance data using the governing equations.

3.3 Results and Discussion

3.3.1 TEM Analysis

Figure 18 shows TEM images of the *t*-BN thin film on the B-doped polycrystalline diamond at different magnifications. Figure 20 (b) exhibits the atomic configuration of the *t*-BN film in more detail. As visible in most regions, the sp^2 -bonded *h*-BN sheets of *t*-BN grew close to the vertical direction with their *c*-axis roughly parallel to the sample surface (see the yellow traces in Figure 20 (b)). However, in a few regions, the *t*-BN planes are also tilted (see the red traces in Figure 20 (b)). The total thickness of the *t*-BN film was estimated to be in the range of 240 ± 10 nm.

Figure 21 presents TEM images of the *c*-BN-1 sample. The dark line at the center of Figure 21 (a) is the interface between the film and the diamond substrate which contains significant hydrogen defects due to the substrate cleaning procedure using H_2 -plasma. It is estimated that the hydrogen is penetrated as much as ~ 10 nm into the diamond substrate thus reducing the interface quality. As visible in Figure 21 (b), the boron nitride film in this sample is a mixture of *t*-BN and *c*-BN phases. The *c*-BN regions, depicted by yellow rectangles, are the lighter clustered regions, while the *t*-BN spots, shown by red

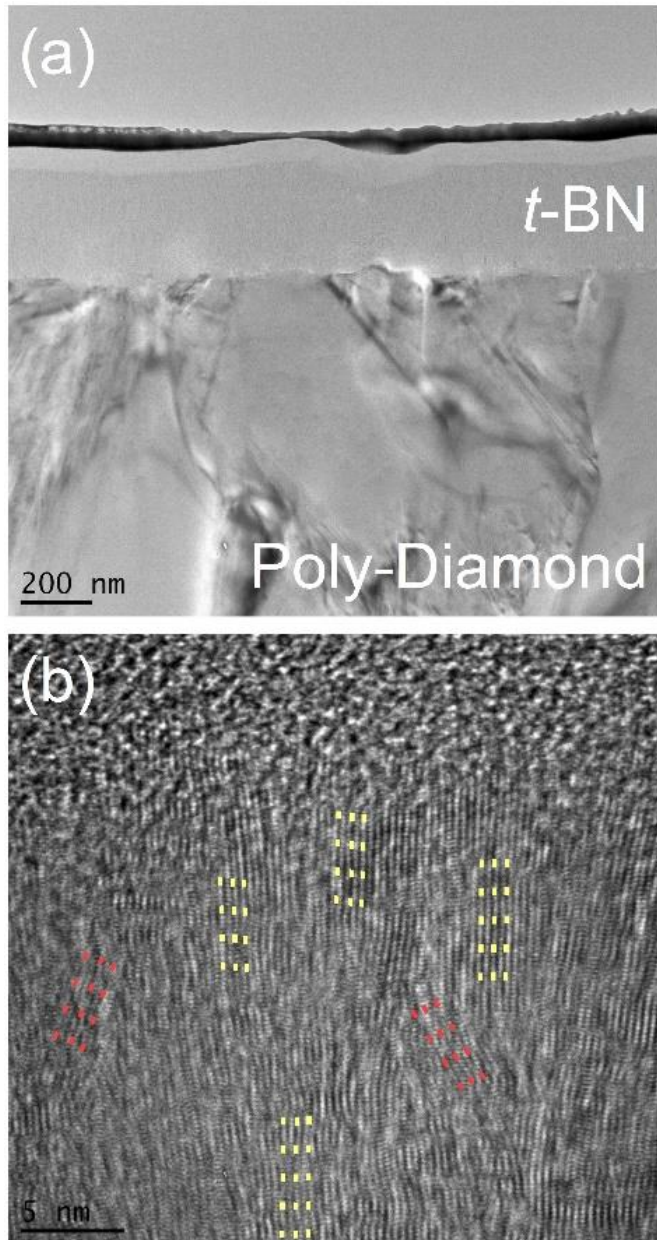


Figure 20: TEM images of the *t*-BN film grown on the B-doped polycrystalline diamond substrates. (a) Lower magnification view. (b) Higher magnification image of the *t*-BN film showing the arrangement of the BN sheets. The yellow traces exhibit the vertically aligned sp^2 -bonded BN sheets whereas the red traces show some regions where the BN planes are tilted slightly. The figure is adapted from E. Guzman *et al.*, “Optical and acoustic phonons in turbostratic and cubic boron nitride thin films on diamond substrates”. *Diamond and Related Materials*, 140 (2023) 110452. Reprinted with permission from Elsevier B.V, Copyright © 2024

rectangles, look like clear parallel lines with various tilt angles. The *t*-BN phase is predominant at the substrate/interface and in the intermediate regions. The top surface of the film is terminated with mostly the *c*-BN phase, although the *t*-BN phase was also detected in some regions. The *c*-BN regions are oriented randomly with grain sizes of ~5-10 nm. The total thickness of the film was estimated to be 168 ± 18 nm.

The structure and morphology of the *c*-BN-2 film are shown in Figure 20. This sample has the higher phase purity of the *c*-BN regions with no signs of the *t*-BN phase at the top surface. The *c*-BN and *t*-BN regions are depicted by yellow and red rectangles in Figure 22 (b). A careful analysis of the film interface with the underlying diamond (111) substrate confirms the existence of a mixture of *h*-BN, *w*-BN, and *t*-BN phases with varying thicknesses. The film is predominantly constituted of *c*-BN grains, randomly oriented in different crystallographic planes. The total thickness of the film is 157 ± 6 nm. This film is essentially epitaxially oriented, phase pure *c*-BN at the diamond interface. Towards the surface, small *t*-BN domains are evident, and the *c*-BN regions show increased orientational randomness.

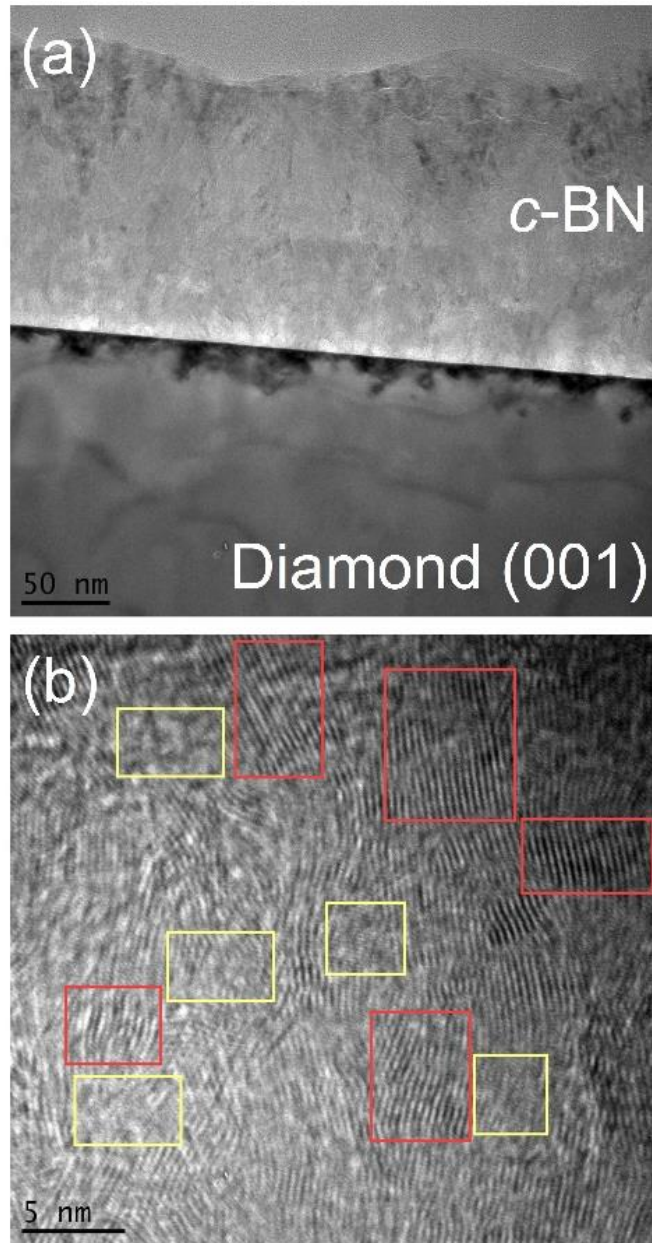


Figure 21: TEM images of the *c*-BN-1 film, interface, and the underlying (001) single-crystal diamond substrate. (a) The dark line shows the interface of the film and the substrate, damaged by hydrogen. (b) Enlarged image of the BN film structure confirming the presence of a mixture of *t*-BN and *c*-BN phases, surrounded by red and yellow rectangles, respectively. The figure is adapted from E. Guzman *et al.*, “Optical and acoustic phonons in turbostratic and cubic boron nitride thin films on diamond substrates”. *Diamond and Related Materials*, 140 (2023) 110452. Reprinted with permission from Elsevier B.V, Copyright © 2024

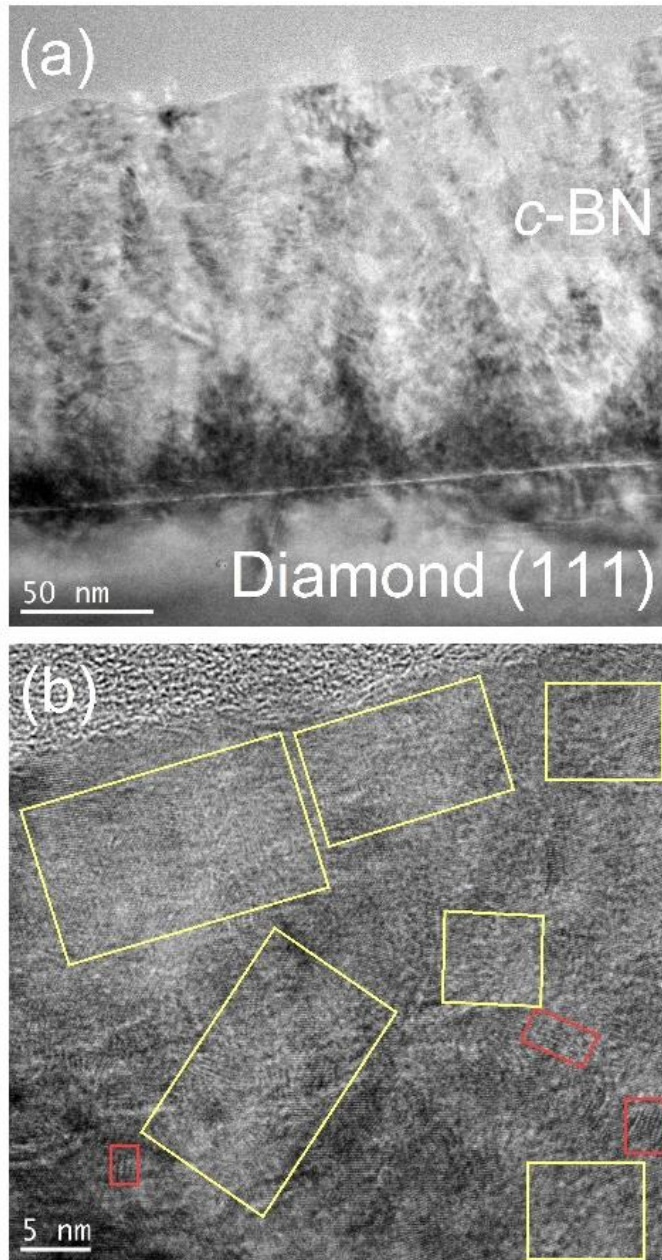


Figure 22: TEM images of the *c*-BN-2 film grown on a (111) single crystal diamond substrate. (a) Lower magnification image. (b) High-resolution image of the *c*-BN-2 sample confirming the dominant *c*-BN phase (yellow zones) compared to the *t*-BN phase (red zones). The *c*-BN regions near the surface show increased orientation randomness. The figure is adapted from E. Guzman *et al.*, “Optical and acoustic phonons in turbostratic and cubic boron nitride thin films on diamond substrates”. *Diamond and Related Materials*, 140 (2023) 110452. Reprinted with permission from Elsevier B.V, Copyright © 2024

3.3.2 Raman Analysis

A series of Raman experiments were conducted on the BN thin films and their respective underlying substrates. To cross-check the results obtained, the same experiments were carried out on bulk single-crystal *c*-BN as the reference sample. Figure 23 presents the Raman spectra of the *t*-BN film (red line) and its underlying B-doped polycrystalline substrate (black line). The sharp peak observed at $\sim 1330\text{ cm}^{-1}$ in both spectra is associated with the zone center Raman peak (ZCP) of the diamond substrate. The ZCP of the undoped diamond is located at 1332 cm^{-1} which in our samples downshifted by 2 cm^{-1} which is attributed to the phonon softening because of the heavy boron doping and clustering [37–39]. The presence of this peak in both spectra confirms that a significant fraction of the incident light interacts with the diamond substrate even though the light is focused on the top surface of the *t*-BN layer. Below the ZCP, the pristine B-doped polycrystalline diamond exhibit broad features at $\sim 607\text{ cm}^{-1}$, 897 cm^{-1} , and 1042 cm^{-1} . These three peaks are the Raman-forbidden bands of diamond which are activated due to the presence of boron dopants [40–42]. The spectrum of the *t*-BN film on the B-doped polycrystalline diamond exhibits quite different features (see the red curve in Figure 23). Except for the strong ZCP, other Raman features, present in the substrate, are not visible in the *t*-BN spectrum, but

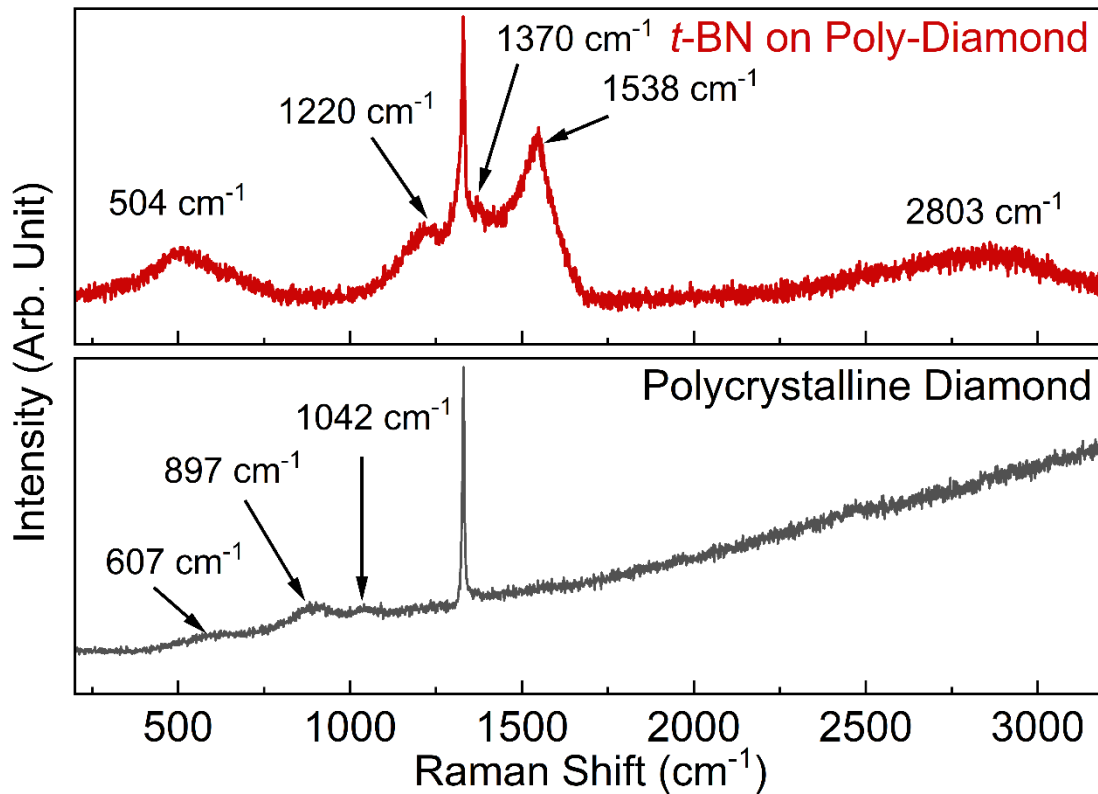


Figure 23: Raman spectra of the *t*-BN film on B-doped polycrystalline diamond substrate under a 488 nm excitation laser. The figure is adapted from E. Guzman *et al.*, “Optical and acoustic phonons in turbostratic and cubic boron nitride thin films on diamond substrates”. *Diamond and Related Materials*, 140 (2023) 110452. Reprinted with permission from Elsevier B.V, Copyright © 2024

new Raman peaks located at 504 cm⁻¹, 1220 cm⁻¹, 1370 cm⁻¹, 1538 cm⁻¹, and 2803 cm⁻¹ are detected. The weak feature at 1370 cm⁻¹ is attributed to the *t*-BN phase [17,18] which is almost hidden due to the sharp ZCP feature and the high background signal from the substrate. The nature of this peak can be thought of as an upshifted single-crystal *h*-BN peak which is expected to be observed at ~1364 cm⁻¹ [43–45]. The peaks at 1220 cm⁻¹ and 1538 cm⁻¹ most likely originate from the maximum phonon density of states of *t*-BN, assuming its crystal similarity with *h*-BN [45]. Other peaks are all associated with the B-

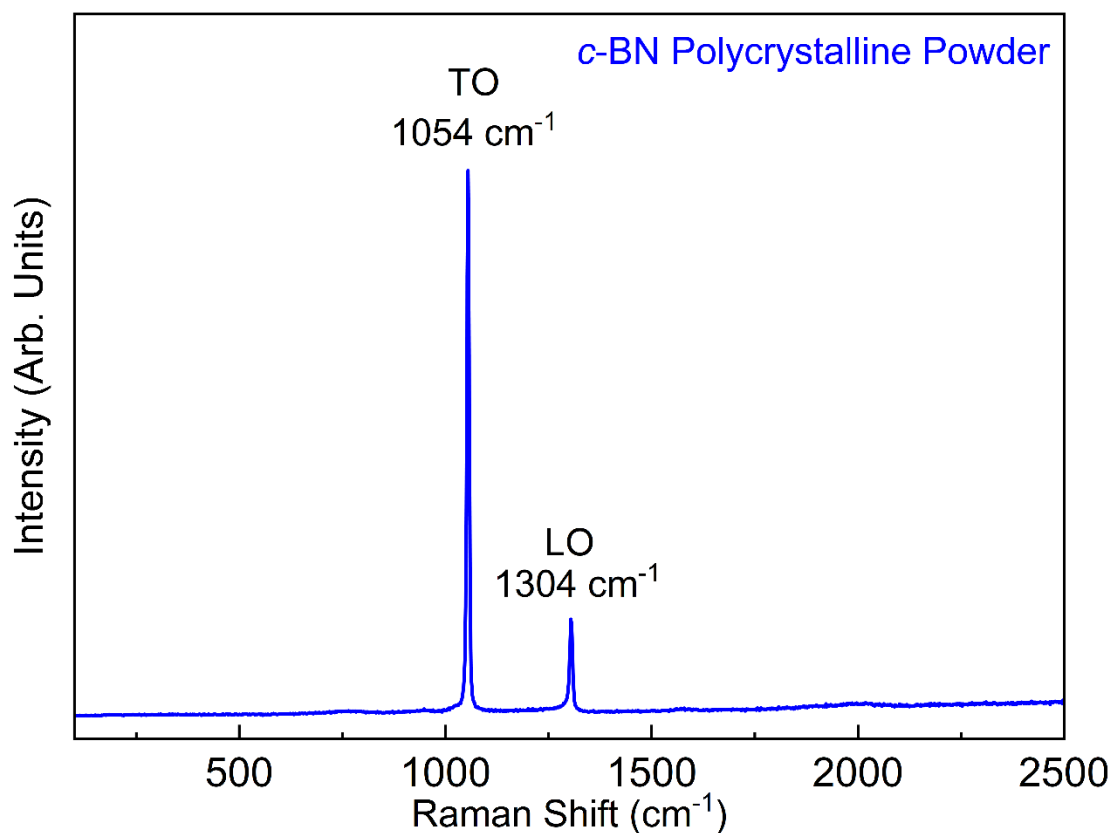


Figure 24: Raman spectra of the bulk single-crystal *c*-BN under a 488 nm excitation laser. The figure is adapted from E. Guzman *et al.*, “Optical and acoustic phonons in turbostratic and cubic boron nitride thin films on diamond substrates”. *Diamond and Related Materials*, 140 (2023) 110452. Reprinted with permission from Elsevier B.V, Copyright © 2024

doped diamond substrate. The peak at 504 cm^{-1} is likely the same as the 607 cm^{-1} peak observed in the substrate. It is redshifted to lower wavenumbers presumably due boron clustering in the heavily B-doped substrate. This peak is associated with the maximum phonon density of states of diamond and is reported to downshift as the boron concentration increases [40]. The broad peak found at $\sim 2803\text{ cm}^{-1}$ has been observed previously in Raman of *h*-BN [45], but no obvious assignment of this peak has been reported or could be made here.

Now, moving to the Raman characteristics of bulk single-crystal *c*-BN and *c*-BN thin films on diamond substrates. The bulk single-crystal *c*-BN samples were outsourced from Hyperion Materials and Technology, the USA. Samples were in powder form with average size of $\sim 300\ \mu\text{m}$ to $\sim 600\ \mu\text{m}$. The Raman spectrum of the polycrystalline *c*-BN powder is presented in Figure 24. The spectrum shows two peaks attributed to the TO and LO modes, respectively, at $1054\ \text{cm}^{-1}$ and $1304\ \text{cm}^{-1}$. The spectral position of these peaks is in excellent agreement with previously reported values [45–47]. Figure 25 shows the results of Raman measurements on the *c*-BN-1 thin film (red curve), and the B-doped single-crystal diamond (001) substrate without *c*-BN film (black curve). Interestingly, no signatures of the TO and LO peaks of *c*-BN were detected in this sample. One may assume that these peaks may have been buried under the intense Raman features coming from the substrate. Given that the TO Raman peak of *c*-BN at $1054\ \text{cm}^{-1}$ should be intense (see Figure 24) and there are no significant diamond features at that wavenumber, this seems less likely. An alternative explanation is that the TO and LO Raman bands in *c*-BN are not detectable due to the presence of high-density defects and the consequent relaxation of Raman selection rules. The latter causes weak scattering from optical phonon modes with

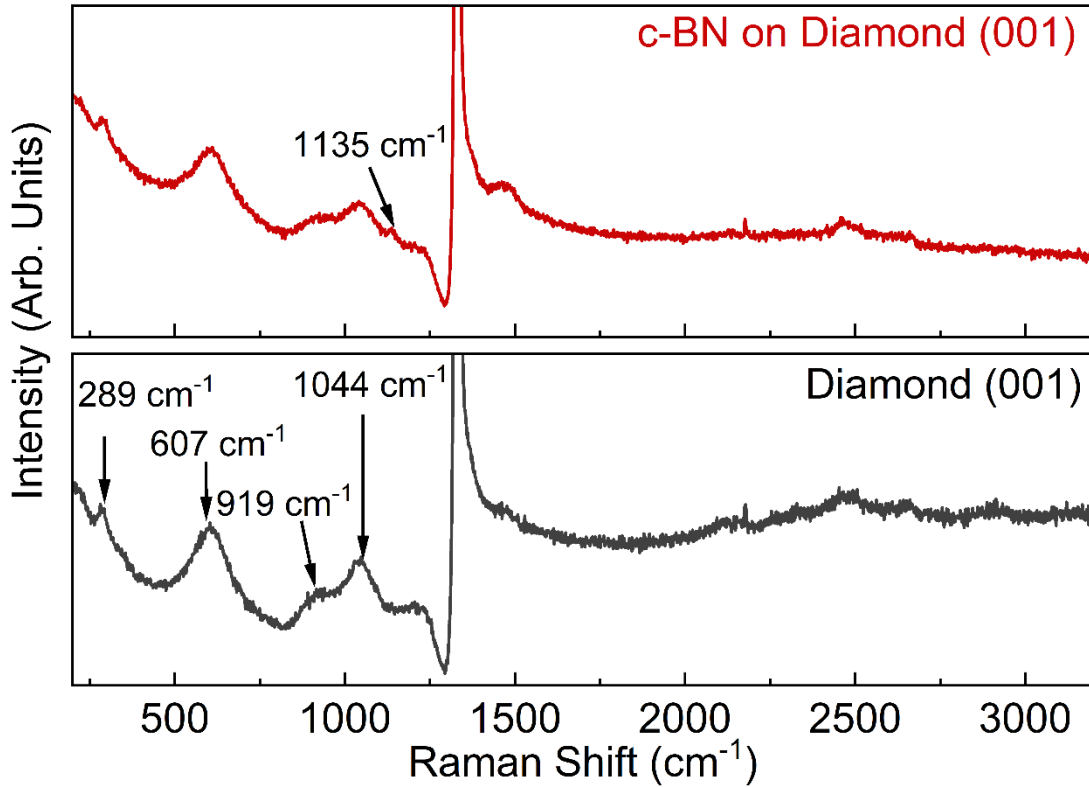


Figure 25: Raman spectra of the *c*-BN film on B-doped single-crystal diamond (001), diamond substrate under a 488 nm excitation laser. The figure is adapted from E. Guzman *et al.*, “Optical and acoustic phonons in turbostratic and cubic boron nitride thin films on diamond substrates”. *Diamond and Related Materials*, 140 (2023) 110452. Reprinted with permission from Elsevier B.V, Copyright © 2024

different wavevectors. This explanation seems more in line with the characteristics of our samples. The only difference in the two spectra obtained from the film and substrate is the presence of a weak Raman feature at 1135 cm^{-1} that could be related to the second-order Raman scattering from the zone-edge LO(L) or LO(X) modes [45]. Figure 26 presents the Raman spectra of the *c*-BN-2 thin film grown on the single-crystal diamond (111) substrate. The two spectra are almost identical, and no peaks associated with the *c*-BN layer could be detected.

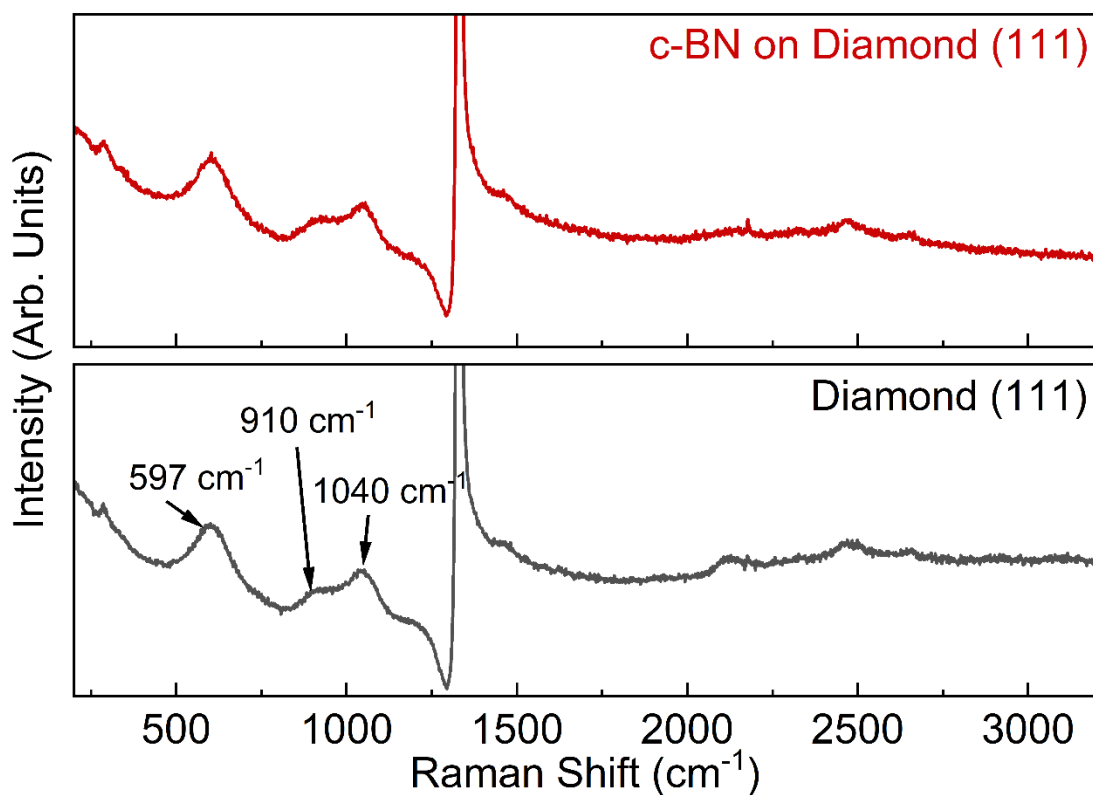


Figure 26: Raman spectra of the *c*-BN film on B-doped single-crystal diamond (111) substrate under a 488 nm excitation laser. The figure is adapted from E. Guzman *et al.*, “Optical and acoustic phonons in turbostratic and cubic boron nitride thin films on diamond substrates”. *Diamond and Related Materials*, 140 (2023) 110452. Reprinted with permission from Elsevier B.V, Copyright © 2024

3.3.3 BMS Results

Now the main element of this work – the observation of acoustic phonons in boron nitride films using the BMS technique. 7 shows the results of the BMS measurements of bulk phonons in the single crystal *c*-BN and the three BN thin films in the frequency range of 25 GHz to 175 GHz. Symmetric peaks on each side of the spectra are associated with the Stokes and Anti-Stokes scattering processes. The spectral positions of the observed peaks, f , were determined accurately by fitting the experimental data with individual Lorentzian functions. In BMS, the phonon wave vector of bulk phonon modes that contribute to light scattering is $q_B = 4\pi n/\lambda$, where $\lambda = 532$ nm is the laser excitation wavelength and n is the refractive index of the medium at λ [32]. The refractive indices of *t*-BN on polycrystalline diamond and *c*-BN on diamond (001) samples could not be measured due to their rough surfaces. To calculate the BMS phonon wavevector, previously reported values of n were used for the *t*-BN and *c*-BN-1 as 1.870 and 2.117, respectively [48]. Note that one should use these values with caution to calculate the BMS phonon wave vector. *t*-BN is a disordered form of *h*-BN along the *c*-axis stacking direction. *h*-BN sheets are optically anisotropic and given that in our *t*-BN film, its constituent *h*-BN sheets are lined up in different orientations close to vertical, taking the reported value for the index of

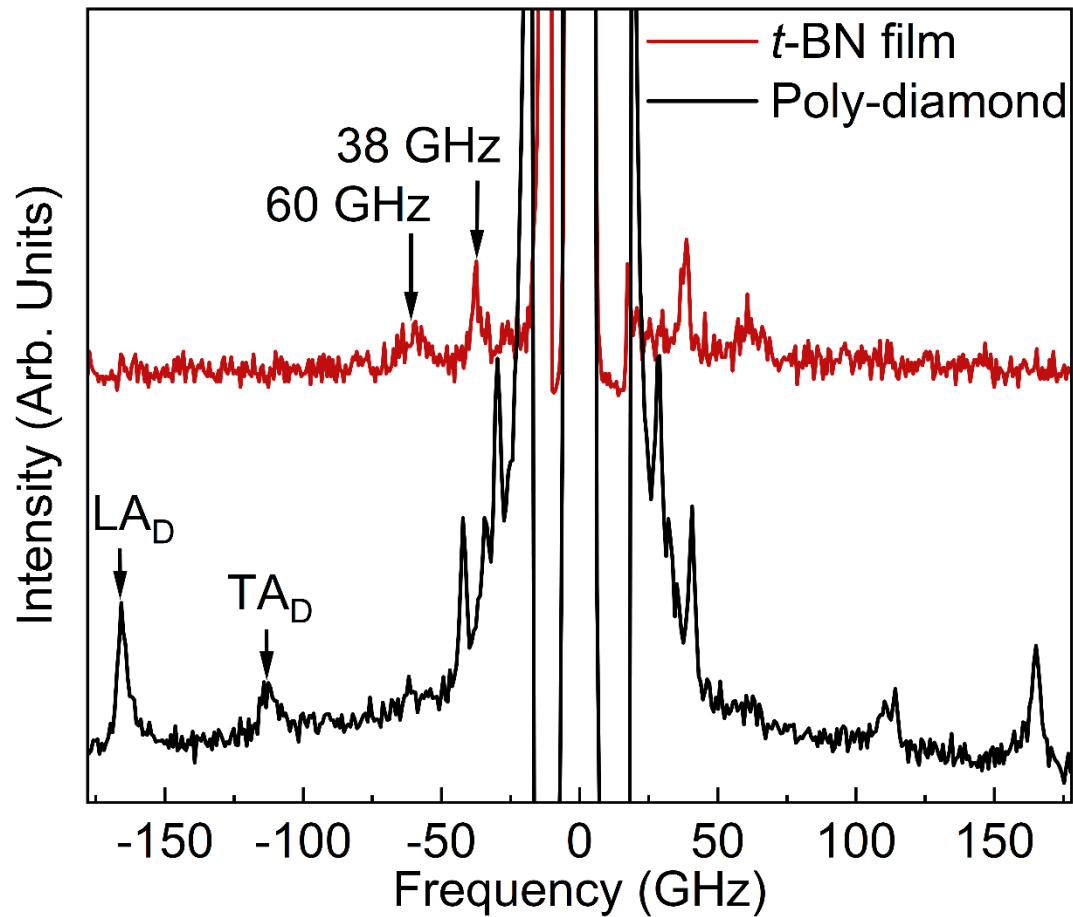


Figure 27: Brillouin light scattering spectra of bulk phonon modes in *t*-BN thin film on B-doped polycrystalline diamond. The peaks labeled as “LA” and “TA” correspond to the longitudinal and transverse acoustic bulk phonons, respectively. The subscript “D” represents “diamond”. The figure is adapted from E. Guzman *et al.*, “Optical and acoustic phonons in turbostratic and cubic boron nitride thin films on diamond substrates”. *Diamond and Related Materials*, 140 (2023) 110452. Reprinted with permission from Elsevier B.V, Copyright © 2024

refraction could impose significant errors. The *c*-BN film on diamond (001) also contains mixed phases of *c*-BN and *t*-BN. The phase proportions in these samples could not be identified from TEM images, and the correct value of n thus remains unclear. The refractive index of the *c*-BN on diamond (111) substrate was measured as $n = 2.12 \pm 0.21$

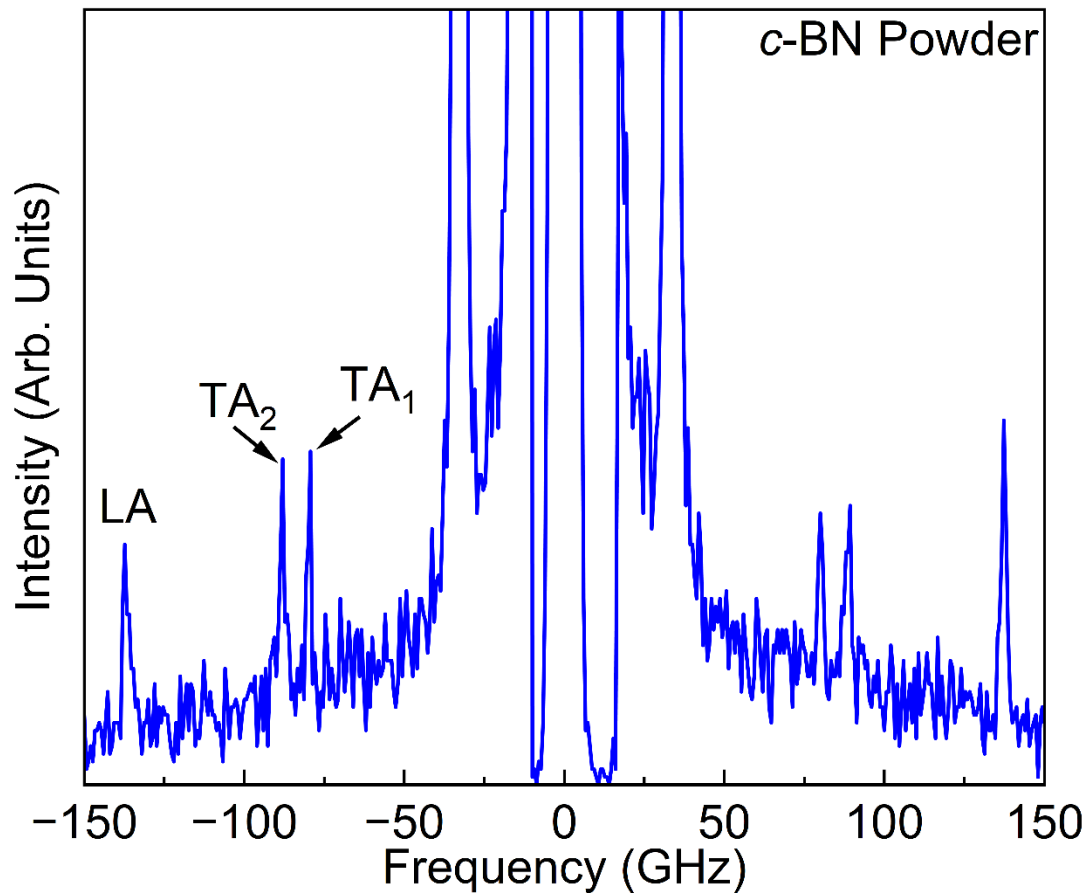


Figure 28: Brillouin light scattering spectra of bulk phonon modes in bulk single-crystal *c*-BN. The figure is adapted from E. Guzman *et al.*, “Optical and acoustic phonons in turbostratic and cubic boron nitride thin films on diamond substrates”. *Diamond and Related Materials*, 140 (2023) 110452. Reprinted with permission from Elsevier B.V, Copyright © 2024

which agrees well with the available data [48,49]. Figure 27 exhibits the BMS spectra of the polycrystalline diamond substrate (black line) and the *t*-BN thin film (red line). Two peaks labeled as “ LA_D ” and “ TA_D ” at $f \sim 165$ GHz and $f \sim 112$ GHz, correspond to the longitudinal and transverse acoustic phonons, respectively, of the polycrystalline diamond. The spectral positions of the LA and TA peaks agree well with the previously reported data [50]. The *t*-BN thin film exhibits two distinct broad peaks at 38 GHz and 60 GHz. The

peak at 60 GHz is detectable only in the p - p or s - s incident-scattered light polarization configuration which is a characteristic of the bulk LA phonons in BMS experiments. The peak at 38 GHz is visible in the cross-polarization configuration (p - s), a property of TA phonons (see Supplementary Information). Thereby, these peaks are attributed to t -BN's transverse acoustic and longitudinal acoustic phonon branches, respectively. Assuming the refractive index of $n = 1.870$, one can extract the phase velocity of these phonon branches according to $v = 2\pi f/q_B = \lambda f/2n$. It should be noted that in the region near the center of the Brillouin Zone (BZ), the dispersion of acoustic phonons follows a linear relationship. Thus, the phase velocity of these phonon branches is equal to their group velocity or “sound velocity”. The calculated phonon group velocities for the TA and LA phonons in the t -BN film are $v_{TA} = 5,405 \text{ ms}^{-1}$ and $v_{LA} = 8,535 \text{ ms}^{-1}$, respectively. It is worthwhile comparing the spectral positions of these peaks with those reported for h -BN. The significance of comparing t -BN results with those for h -BN lies in the fact that as stated previously, the t -BN phase constitutes from tilted disorder h -BN sheets with slightly increased interlayer distance [16–18].

The previous reports on the Brillouin light spectroscopy measurements of bulk h -BN show LA phonon peaks at ~ 28 GHz and ~ 112 GHz with phonon wave vector along and

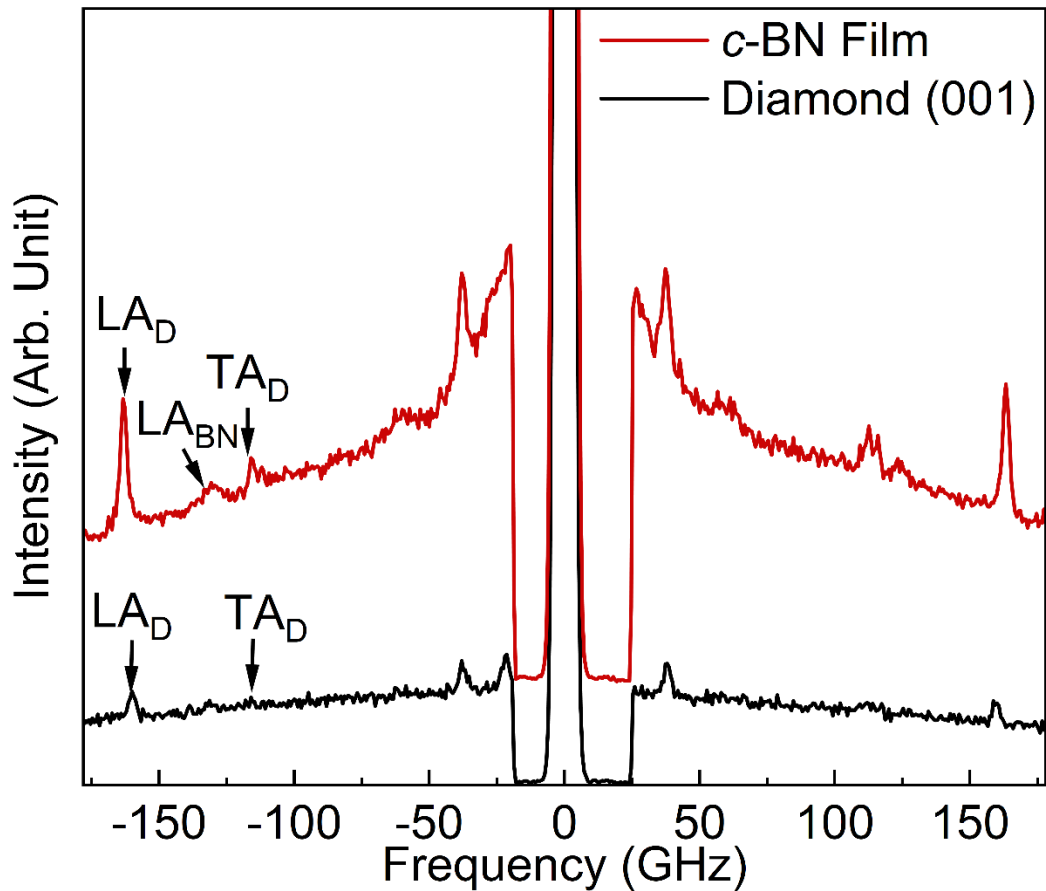


Figure 29: Brillouin light scattering spectra of bulk phonon modes in *c*-BN thin film on diamond (001). The peaks labeled as “LA” and “TA” correspond to the longitudinal and transverse acoustic bulk phonons, respectively. The subscripts “D” and “BN” represent “diamond” and “boron nitride”. The figure is adapted from E. Guzman *et al.*, “Optical and acoustic phonons in turbostratic and cubic boron nitride thin films on diamond substrates”. *Diamond and Related Materials*, 140 (2023) 110452. Reprinted with permission from Elsevier B.V, Copyright © 2024

perpendicular to the *c*-axis of *h*-BN, respectively [51]. This is expected due to the large anisotropy in elastic properties of *h*-BN, with a slow LA phonon velocity of $\sim 3,279 \text{ ms}^{-1}$ along the *c*-axis compared to a fast LA phonon velocity of $18,595 \text{ ms}^{-1}$ perpendicular to the *c*-axis. In our experiments, the examined phonon wave vector was close to the surface

normal of the film. Given most of its *h*-BN sheets in the *t*-BN film are aligned vertically (see Figure 20 (a)), it is reasonable to observe LA phonon velocity at some weighted average frequency of LA phonons propagating along and perpendicular to *h*-BN *c*-axis.

To characterize the acoustic phonon properties of *c*-BN films, BMS experiments were first conducted on bulk single-crystal *c*-BN as the reference sample. Figure 28 shows the accumulated BMS spectra. Three sharp peaks at 79.6 GHz, 88.1 GHz, and 137.1 GHz are attributed to two TA and one LA phonon modes. The Brillouin phonon wave vector in these experiments is $q_B = 50.01 \mu\text{m}^{-1}$, assuming $n = 2.117$ at $\lambda = 532 \text{ nm}$ for *c*-BN [48,49]. The corresponding phonon group velocities for LA and TA phonons in single-crystal *c*-BN are calculated as $17,225 \text{ ms}^{-1}$, $11,069 \text{ ms}^{-1}$, and $10,000 \text{ ms}^{-1}$, respectively. The obtained values for the bulk *c*-BN were used as a reference for the characteristics of *c*-BN thin films on diamond substrates.

Figure 29 shows the spectra for the *c*-BN thin film on diamond (001). The black and red curves are the spectra for the pristine diamond and the thin film, respectively. As seen, in the diamond substrate, two peaks were detected at 116.6 GHz and 159.4 GHz, corresponding to the TA and LA phonon branches along the diamond [100] crystallographic direction. The BMS spectrum for the *c*-BN shows an additional broad and

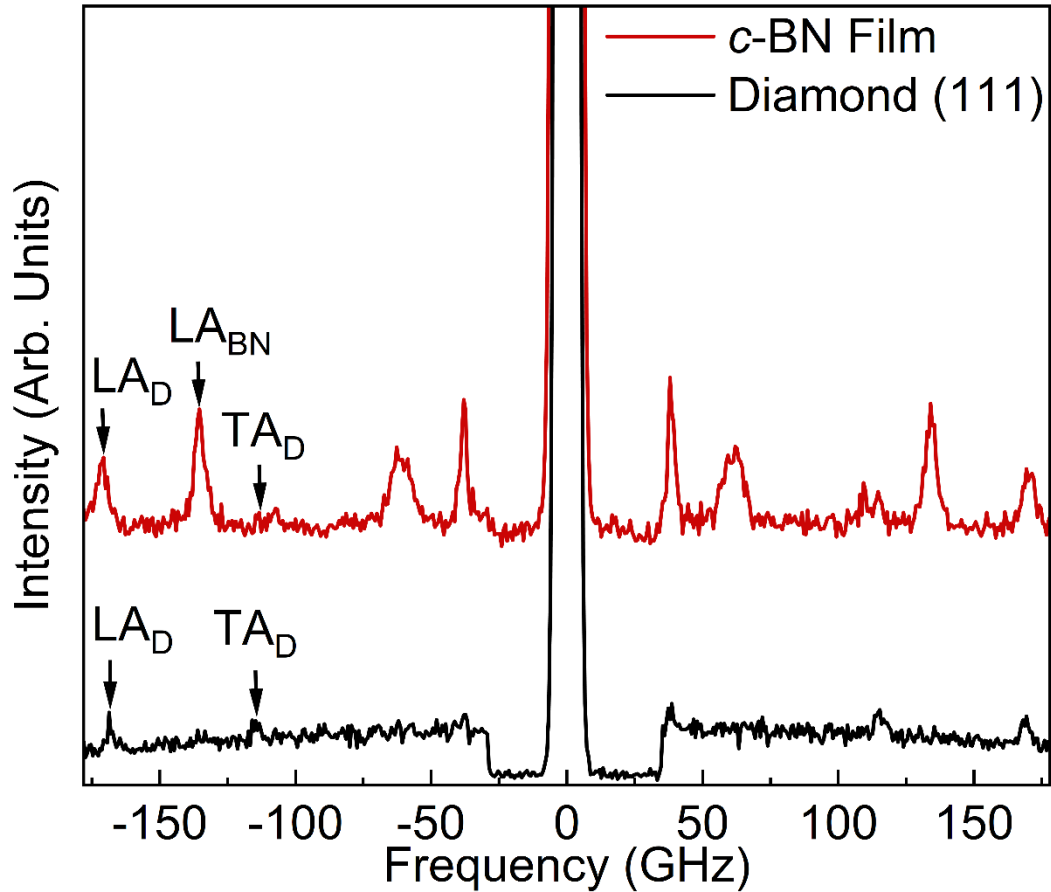


Figure 30: Brillouin light scattering spectra of bulk phonon modes in *c*-BN thin film on diamond (111). The peaks labeled as “LA” and “TA” correspond to the longitudinal and transverse acoustic bulk phonons, respectively. The subscripts “D” and “BN” represent “diamond” and “boron nitride”. The figure is adapted from E. Guzman *et al.*, “Optical and acoustic phonons in turbostratic and cubic boron nitride thin films on diamond substrates”. *Diamond and Related Materials*, 140 (2023) 110452. Reprinted with permission from Elsevier B.V, Copyright © 2024

weak peak located at 129.2 GHz. This peak is attributed to the LA_{BN} phonon of *c*-BN. The spectral position of this peak is ~ 8 GHz lower than that for the LA peak of the bulk single-crystal *c*-BN, presumably due to the existence of some *t*-BN regions mixed with the dominant *c*-BN phase. Assuming $n = 2.117$, one would extract a phonon group velocity

of $v_{LA} = 16,234 \text{ ms}^{-1}$, almost 6% lower than that for the single-crystal *c*-BN sample. The presence of a small fraction of *t*-BN mixed phase manifests itself in a slower phonon group velocity compared to that of the pure phase *c*-BN. Figure 30 presents the BMS spectra for the *c*-BN film on a diamond (111) substrate. The TA_D and LA_D peaks for the diamond with phonon wave vector along [111] direction appear at 114.4 GHz and 168.5 GHz, respectively (black curve). The spectrum for the *c*-BN film exhibits a sharp and well-defined Lorentzian peak at 135.4 GHz which is attributed to the LA_{BN} phonon branch. As seen, the spectral position of this peak is only ~ 1.7 GHz lower than the single-crystal bulk *c*-BN sample. Using the measured refractive index of $n = 2.12$, the phonon group velocity is calculated to be $v_{LA} = 16,989 \text{ ms}^{-1}$ which is only 1.4% lower than that for the single-crystal bulk *c*-BN. The latter confirms that the *c*-BN on diamond (111) sample has a higher order of *c*-BN phase purity. These findings align with the TEM results indicating higher content of *c*-BN phase in thin films grown on diamond (111) substrate compared to that of the diamond (001). Other peaks that appeared at much lower frequencies are associated with the scattering of light by surface phonons, or surface acoustic waves, which are discussed in the following.

In our experiments, the BMS spectra revealed several peaks in the low-frequency range. These features are related to the scattering of light by surface ripples created by surface acoustic waves propagating along the film layer. The phonon wave vector associated with these surface phonons in the backscattering geometry is $q_s = 4\pi \sin(\theta) / \lambda$ in which θ is the incident angle and λ is the laser excitation wavelength [32–34]. The direction of the surface phonon wave vector lies in the scattering plane parallel to the film surface plane.

The magnitude of q_s only depends on the incident angle, θ , and is no longer a function of the refractive index, n . Therefore, one can obtain the dispersion of surface phonons, *i.e.*, f as a function of q_s , by changing the incident angle. Note that the types of surface acoustic phonons which can be detected via BMS in the supported thin films strongly depend on the transparency, thickness, crystal structure, relative acoustic velocity of the film with respect to its underlying substrate, and its displacement vibrational profile [52]. Cubic BN is among the materials with extraordinarily high acoustic phonon velocities. However, compared to diamond, acoustic phonons travel at slower velocities. In the case of slow films on fast substrates, discrete phonon modes associated with Rayleigh and Sezawa waves may appear in the BMS spectra, depending on the thickness of the films [52,53].

The surface Brillouin light scattering experiments were restricted to the *c*-BN thin films on diamond substrates. The surface of the *t*-BN sample was rather rough making it impossible to accumulate data within a reasonable accumulation time. The incident angle, θ , was varied to select the q_s , and the spectral position of the BMS peaks were plotted as a function of q_s to obtain the phonon dispersion. The phase velocity of the peaks was extracted

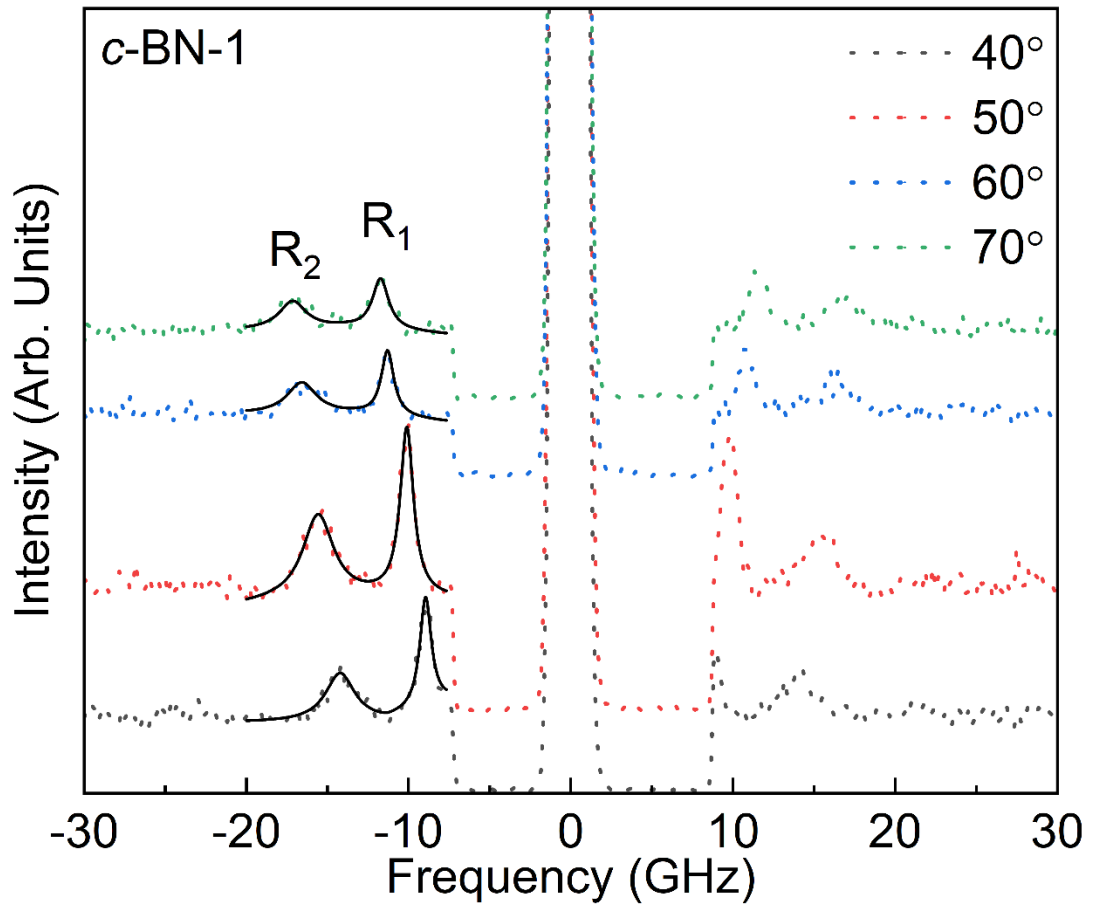


Figure 31: Brillouin spectra of the *c*-BN thin film on the diamond (001) substrate. Peaks denoted by “R” represent Rayleigh acoustic waves. Raw data is presented as dotted lines and the fitted data is shown as solid black lines. The figure is adapted from E. Guzman *et al.*, “Optical and acoustic phonons in turbostratic and cubic boron nitride thin films on diamond substrates”. *Diamond and Related Materials*, 140 (2023) 110452. Reprinted with permission from Elsevier B.V, Copyright © 2024

according to $v_s = \omega/q_s = 2\pi f/q_s$. Note that surface phonons in layered structures are dispersive, *i.e.*, the phase velocity of phonons is no longer equal to their group velocity.

Figures 31-32 present the results of the surface Brillouin scattering measurements performed on the *c*-BN thin film grown on diamond (001) and diamond (111), respectively.

The raw data is presented as scattered dots, and the peaks were fitted using individual

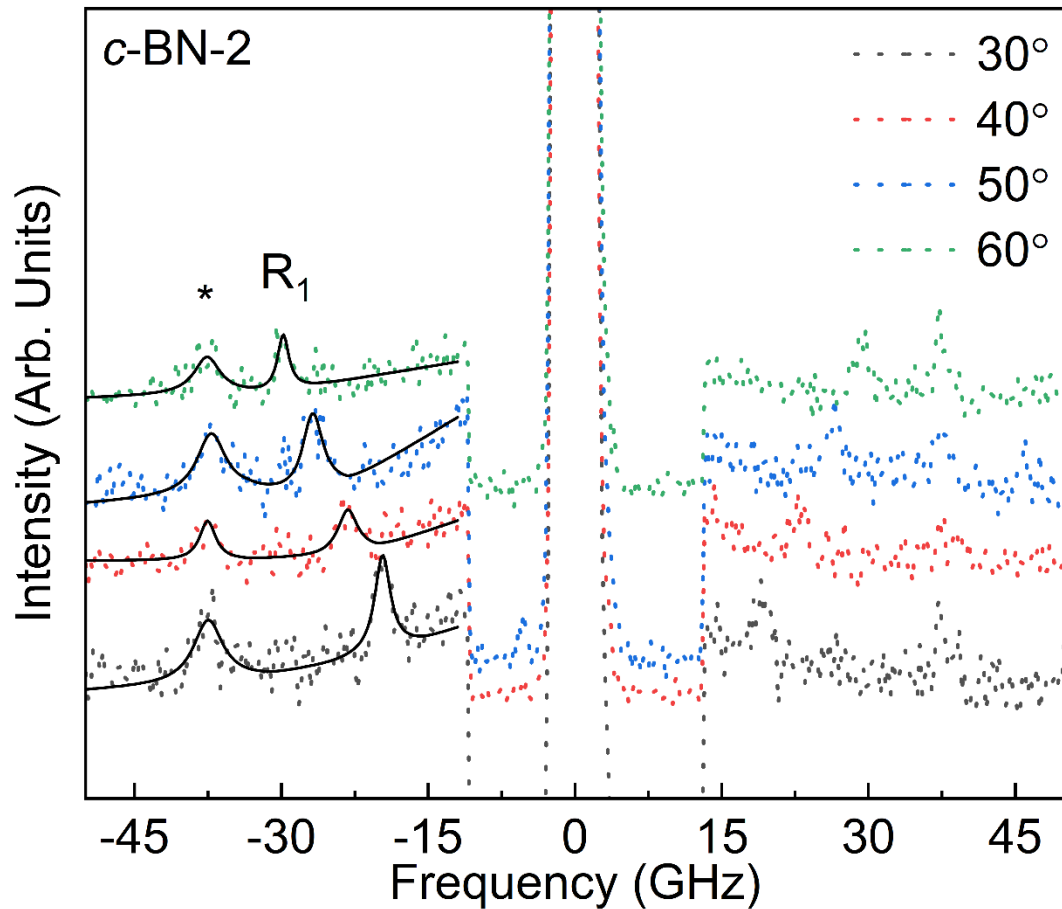


Figure 32: Brillouin spectra of the *c*-BN thin film on the diamond (111) substrate. Peaks denoted by “R” represent Rayleigh acoustic waves. The nature of the peak labeled with an “*” is unclear. Raw data is presented as dotted lines and the fitted data is shown as solid black lines. The figure is adapted from E. Guzman *et al.*, “Optical and acoustic phonons in turbostratic and cubic boron nitride thin films on diamond substrates”. *Diamond and Related Materials*, 140 (2023) 110452. Reprinted with permission from Elsevier B.V, Copyright © 2024

Lorentzian functions (solid lines). The *c*-BN film on diamond (001) exhibits two peaks, marked as R₁ and R₂, which are attributed to the first and higher-order Rayleigh waves, respectively. The frequency of these peaks increases with increasing θ and thus, q_s . In the case of *c*-BN on diamond (111) presented in Figure 32, the data shows two peaks as well. The spectral position of the peak at the lower frequency range changes with varying q_s .

This peak is denoted as R_1 and is associated with the Rayleigh acoustic wave. However, the frequency of the peak labeled with an ‘*’ and located at 38 GHz remains constant. The origin of this ‘spurious’ peak is unclear. The peak at 38 GHz was occasionally observed in the data presented for the diamond substrate as well, and it is possible that this peak originated from the substrate as *c*-BN is transparent in the visible light region. Since the frequency of the Rayleigh peaks in thin film structures depend on the film thickness, it is conventional to present the spectral position of the surface acoustic Rayleigh waves as a function of the nondimensional parameter $q_s h$ (Figure 33). The average thickness of the samples, h , for the *c*-BN-1 and *c*-BN-2 samples are 168 ± 18 nm and 157 ± 6 nm. These values are based on measurements of the TEM images shown in Figure 20-22.

Figure 34 shows the calculated phase velocity as a function of $q_s h$. As expected, the phase velocity of the Rayleigh waves decreases with increasing $q_s h$ confirming its dispersive nature in thin film structures. Notably, the phase velocity of these modes is more than two times higher in the *c*-BN thin film on diamond (111), compared to that of the film on the diamond (001) substrate. The dispersion and velocity of Rayleigh waves in thin film structures depend on the thickness, the elastic coefficients of the substrate and the film, and

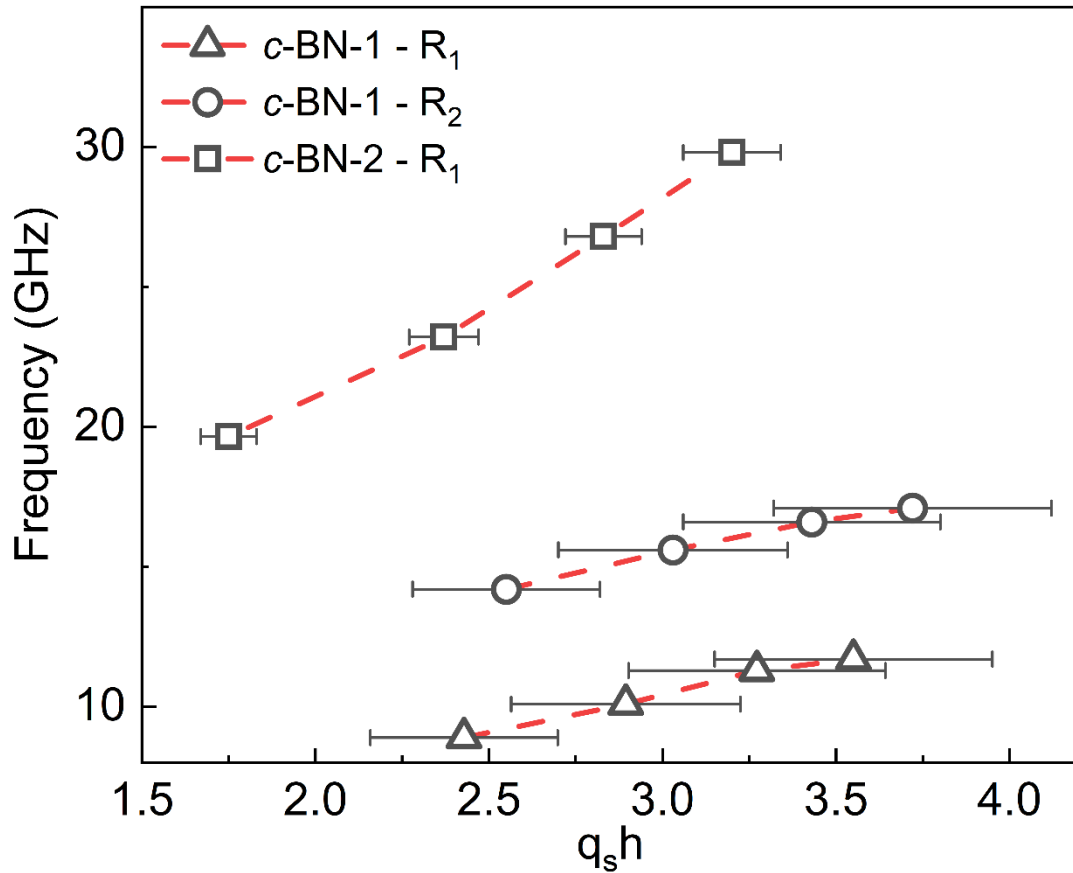


Figure 33: Spectral position and the calculated phase velocity of the surface phonons of the *c*-BN film on the diamond (001) substrate. The figure is adapted from E. Guzman *et al.*, “Optical and acoustic phonons in turbostratic and cubic boron nitride thin films on diamond substrates”. *Diamond and Related Materials*, 140 (2023) 110452. Reprinted with permission from Elsevier B.V, Copyright © 2024

the quality of bonding at the interface [54,55]. Due to the dissimilar crystallographic directions of the substrates used and the different thicknesses of the films, a reasonable comparison of the Rayleigh wave characteristics in these samples is not feasible. However, such a significant disparity in phase velocities were not expected for first-order Rayleigh waves (R1, in Figure 34) in two samples. The latter is most likely attributed to the better

phase purity and interface quality of the films grown on diamond (111) sample, which agrees with the TEM measurements.

To estimate the thermal interface conductance of *c*-BN on diamond samples, it is worth calculating the phonon transmissivity across the interfaces based on the BMS results using the acoustic mismatch model. The TA peaks could not be observed in the BMS measurements of *c*-BN thin films and thus, the analysis is limited to the calculation transmissivity coefficient of LA phonon branches. According to AMM, at normal incidence, the transmission coefficient from the film to the substrate is described as, $\tau_{f \rightarrow s} = 1 - R_{f \rightarrow s}$, in which the reflectivity, $R_{f \rightarrow s}$ is a function of acoustic impedances of the two media, $R_{f \rightarrow s} = |(\zeta_f - \zeta_s)/(\zeta_f + \zeta_s)|^2$. Table 1 summarizes the experimental bulk phonon velocities of the films and their respective substrates obtained from BMS experiments and the phonon transmission coefficient for the LA branch at the interface. As seen, the transmissivity coefficient for the *c*-BN on diamond samples reaches almost unity demonstrating that the thermal boundary resistance in these heterostructures could be among the lowest in UWBG heterostructures. The latter has important implications in the efficient thermal management of high-power UWBG-based heterostructure devices in which effective heat dissipation remains a formidable challenge.

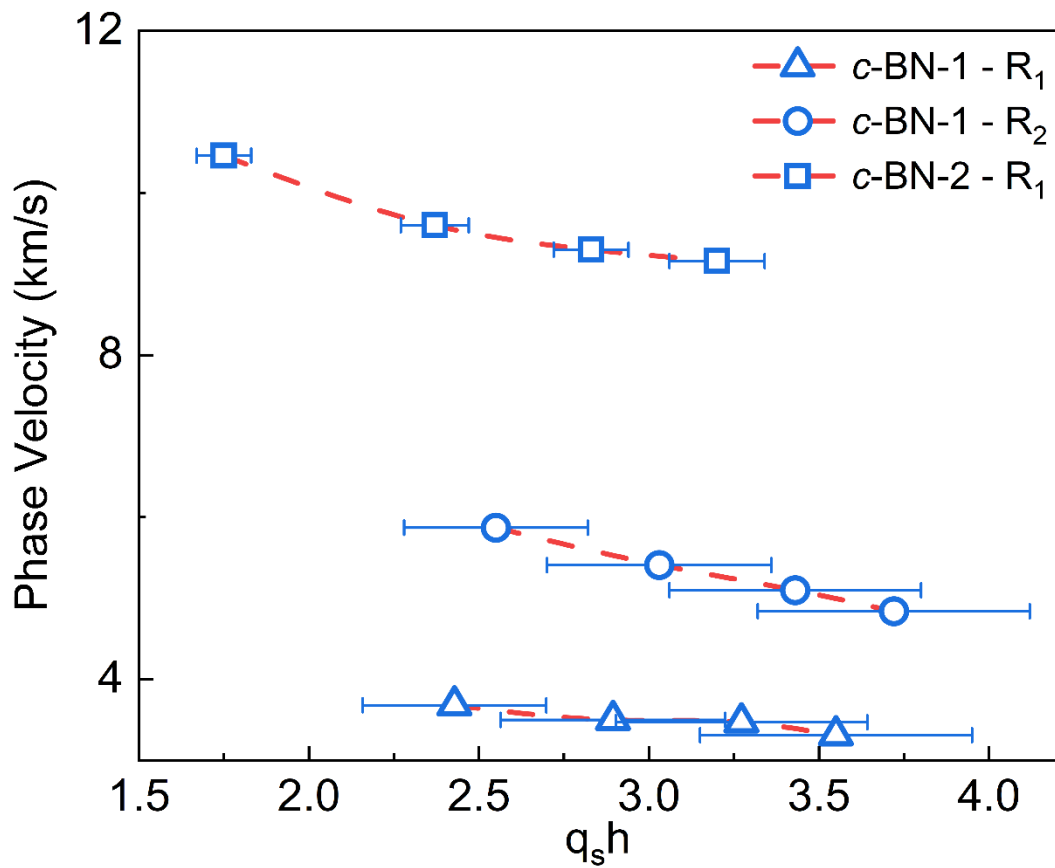


Figure 34: Spectral position and the calculated phase velocity of the surface phonons of the *c*-BN film on the diamond (111) substrate. The figure is adapted from E. Guzman *et al.*, “Optical and acoustic phonons in turbostratic and cubic boron nitride thin films on diamond substrates”. *Diamond and Related Materials*, 140 (2023) 110452. Reprinted with permission from Elsevier B.V, Copyright © 2024

Table 4: Calculated and reported values for refractive index, density, bulk phonon velocity, acoustic impedance, and transmission coefficient of the relevant boron nitride and diamond films

Sample	n	ρ [kgm^{-3}]	v_{TA1} [ms^{-1}]	v_{TA2} [ms^{-1}]	v_{LA} [ms^{-1}]	ζ [$MPa.s.m^{-3}$]	$\tau_{f \rightarrow s}$ (%)
Bulk single-crystal c-BN	2.117	3450	10,002	11,070	17,227	59.43	NA
t-BN	1.87	2100	5,405		8,535	17.92	68.5
Polycrystalline diamond	2.43	3530	12,260		18,062	63.76	
c-BN-1	2.117	3450			16,234	56.00	99.7
Diamond (001)	2.43	3530	12,764		17,449	61.59	
c-BN-2	2.117	3450			16,989	58.61	99.7
Diamond (111)	2.43	3530	12,523		18,445	65.11	

3.4 Conclusions

The bulk and surface phonons in *t*-BN and *c*-BN thin films grown on diamond substrates have been investigated using visible Raman and Brillouin-Mandelstam light scattering spectroscopy. The results were correlated with the phase purity and film-substrate interface quality analyses of samples obtained from the corresponding high-resolution transmission electron microscopy images of the same films. Raman characterization did not provide sufficient information about the *c*-BN thin films; either due to the presence of defects or because of strong Raman features of the underlying B-doped diamond substrates. In contrast, the bulk and surface BMS measurement revealed well-distinguished peaks associated with the BN thin films. It was found that bulk acoustic phonons appeared at higher energies in BMS spectra for the *c*-BN thin film grown on diamond (111) compared to that of the film grown on diamond (001). The spectral position of the longitudinal acoustic phonons in the *c*-BN film on diamond (111) was close to that of the bulk single-crystal *c*-BN confirming its higher *c*-BN phase purity. Additionally, the results of the surface Brillouin scattering experiments revealed more than two times faster phase velocity for Rayleigh acoustic waves in the *c*-BN film on diamond (111) sample, which can be attributed to its higher phase purity and better film-interface quality. These findings agree well with the results of our TEM analyses. Our findings attest to the BMS as a powerful tool in the characterization of phonon properties in ultra-wide bandgap heterostructures. The information about the acoustic bulk and surface phonon properties in *c*-BN thin films has important implications in evaluating the thermal interfacial conductance in layered structures.

3.5 References

- (1) Tsao, J. Y.; Chowdhury, S.; Hollis, M. A.; Jena, D.; Johnson, N. M.; Jones, K. A.; Kaplar, R. J.; Rajan, S.; Van de Walle, C. G.; Bellotti, E.; Chua, C. L.; Collazo, R.; Coltrin, M. E.; Cooper, J. A.; Evans, K. R.; Graham, S.; Grotjohn, T. A.; Heller, E. R.; Higashiwaki, M.; Islam, M. S. Ultrawide-Bandgap Semiconductors: Research Opportunities and Challenges. *Advanced Electronic Materials* **2017**, *4* (1), 1600501. <https://doi.org/10.1002/aelm.201600501>.
- (2) Wong, M. H.; Bierwagen, O.; Kaplar, R. J.; Umezawa, H. Ultrawide-Bandgap Semiconductors: An Overview. *Journal of Materials Research* **2021**, *36* (23), 4601–4615. <https://doi.org/10.1557/s43578-021-00458-1>.
- (3) Soltani, A.; Barkad, H. A.; Mattalah, M.; Benbakhti, B.; De Jaeger, J. C.; Chong, Y. K.; Zou, Y.; Zhang, W.; Lee, S. H.; Benmoussa, A.; Giordanengo, B.; Hochedez, J. F. 193nm Deep-Ultraviolet Solar-Blind Cubic Boron Nitride Based Photodetectors. *Applied Physics Letters* **2008**, *92* (5), 053501–053501. <https://doi.org/10.1063/1.2840178>.
- (4) Zou, Y.; Zhang, Y.; Hu, Y.; Gu, H. Ultraviolet Detectors Based on Wide Bandgap Semiconductor Nanowire: A Review. *Sensors* **2018**, *18* (7), 2072. <https://doi.org/10.3390/s18072072>.
- (5) Noor Mohammad, S. Electrical Characteristics of Thin Film Cubic Boron Nitride. *Solid-State Electronics* **2002**, *46* (2), 203–222. [https://doi.org/10.1016/s0038-1101\(01\)00160-5](https://doi.org/10.1016/s0038-1101(01)00160-5).
- (6) Taniguchi, T.; Koizumi, S.; Watanabe, K.; Sakaguchi, I.; Sekiguchi, T.; Yamaoka, S. High Pressure Synthesis of UV-Light Emitting Cubic Boron Nitride Single Crystals. *Diamond and Related Materials* **2003**, *12* (3-7), 1098–1102. [https://doi.org/10.1016/s0925-9635\(02\)00330-8](https://doi.org/10.1016/s0925-9635(02)00330-8).
- (7) Turiansky, M. E.; Wickramaratne, D.; Lyons, J. L.; Van de Walle, C. G. Prospects for N-Type Conductivity in Cubic Boron Nitride. *Applied Physics Letters* **2021**, *119* (16), 162105. <https://doi.org/10.1063/5.0069970>.
- (8) Auciello, O.; Sumant, A. V. Status Review of the Science and Technology of Ultrananocrystalline Diamond (UNCDTM) Films and Application to Multifunctional Devices. *Diamond and Related Materials* **2010**, *19* (7-9), 699–718. <https://doi.org/10.1016/j.diamond.2010.03.015>.
- (9) Zhang, W.; Chong, Y. M.; He, B.; Bello, I.; Lee, S. T. Cubic Boron Nitride Films. *Comprehensive hard Materials* **2014**, *3*, 607–639. <https://doi.org/10.1016/b978-0-08-096527-7.00061-1>.
- (10) Izyumskaya, N.; Demchenko, D. O.; Das, S.; Özgür, Ü.; Avrutin, V.; Morkoç, H. Recent Development of Boron Nitride towards Electronic Applications. *Advanced Electronic Materials* **2017**, *3* (5), 1600485. <https://doi.org/10.1002/aelm.201600485>.
- (11) Chrenko, R. M. Ultraviolet and Infrared Spectra of Cubic Boron Nitride. *Solid State Communications* **1974**, *14* (6), 511–515. [https://doi.org/10.1016/0038-1098\(74\)90978-8](https://doi.org/10.1016/0038-1098(74)90978-8).

- (12) Chen, K.; Song, B.; Ravichandran, N. K.; Zheng, Q.; Chen, X.; Lee, H.; Sun, H.; Li, S.; Udalamatta Gamage, G. A. G.; Tian, F.; Ding, Z.; Song, Q.; Rai, A.; Wu, H.; Koirala, P.; Schmidt, A. J.; Watanabe, K.; Lv, B.; Ren, Z.; Shi, L. Ultrahigh Thermal Conductivity in Isotope-Enriched Cubic Boron Nitride. *Science* **2020**, *367* (6477), 555–559. <https://doi.org/10.1126/science.aaz6149>.
- (13) Samantaray, C. B.; Singh, R. N. Review of Synthesis and Properties of Cubic Boron Nitride (C-BN) Thin Films. *International Materials Reviews* **2005**, *50* (6), 313–344. <https://doi.org/10.1179/174328005x67160>.
- (14) Zhang, X.; Meng, J. Recent Progress of Boron Nitrides. *Materials Today* **2019**, 347–419. <https://doi.org/10.1016/b978-0-12-815468-7.00004-4>.
- (15) Mirkarimi, P. B.; McCarty, K. F.; Medlin, D. L. Review of Advances in Cubic Boron Nitride Film Synthesis. *Materials Science and Engineering: R: Reports* **1997**, *21* (2), 47–100. [https://doi.org/10.1016/s0927-796x\(97\)00009-0](https://doi.org/10.1016/s0927-796x(97)00009-0).
- (16) Zhang, X. W.; Boyen, H. G.; Yin, H.; Ziemann, P.; Banhart, F. Microstructure of the Intermediate Turbostratic Boron Nitride Layer. *Diamond and Related Materials* **2005**, *14* (9), 1474–1481. <https://doi.org/10.1016/j.diamond.2005.03.002>.
- (17) Zhong, B.; Zhang, T.; Huang, X. X.; Wen, G. W.; Chen, J. W.; Wang, C. J.; Huang, Y. D. Fabrication and Raman Scattering Behavior of Novel Turbostratic BN Thin Films. *Materials Letters* **2015**, *151* (151), 130–133. <https://doi.org/10.1016/j.matlet.2015.03.059>.
- (18) Jähnichen, T.; Hojak, J.; Bläker, C.; Christoph Pasel; Mauer, V.; Zittel, V.; Denecke, R.; Bathen, D.; Enke, D. Synthesis of Turbostratic Boron Nitride: Effect of Urea Decomposition. *PubMed Central* **2022**, *7* (37), 33375–33384. <https://doi.org/10.1021/acsomega.2c04003>.
- (19) Mirkarimi, P. B.; McCarty, K. F.; Cardinale, G. F.; Medlin, D. L.; Ottesen, D. K.; Johnsen, H. A. Substrate Effects in Cubic Boron Nitride Film Formation. *Journal of Vacuum Science & Technology A Vacuum Surfaces and Films* **1996**, *14* (1), 251–255. <https://doi.org/10.1116/1.579928>.
- (20) Zhang, W. J.; Bello, I.; Lifshitz, Y.; Chan, K. M.; Wu, Y.; Chan, C. Y.; Meng, X. M.; Lee, S. T. Thick and Adherent Cubic Boron Nitride Films Grown on Diamond Interlayers by Fluorine-Assisted Chemical Vapor Deposition. *Applied Physics Letters* **2004**, *85* (8), 1344–1346. <https://doi.org/10.1063/1.1784545>.
- (21) Khan, S.; Angeles, F.; Wright, J.; Saurabh Vishwakarma; Ortiz, V. H.; Guzman, E.; Fariborz Kargar; Balandin, A. A.; Smith, D. J.; Jena, D.; H. Grace Xing; Wilson, R. Properties for Thermally Conductive Interfaces with Wide Band Gap Materials. *ACS Applied Materials & Interfaces* **2022**, *14* (31), 36178–36188. <https://doi.org/10.1021/acsomega.2c01351>.
- (22) Huang, X.; Guo, Z. High Thermal Conductance across C-BN/Diamond Interface. *Diamond and Related Materials* **2020**, *108*, 107979. <https://doi.org/10.1016/j.diamond.2020.107979>.

- (23) Little, W. A. The Transport of heat between Dissimilar Solids at Low Temperatures. *Canadian Journal of Physics* **1959**, *37* (3), 334–349. <https://doi.org/10.1139/p59-037>.
- (24) Swartz, E. T.; Pohl, R. O. Thermal Boundary Resistance. *Reviews of Modern Physics* **1989**, *61* (3), 605–668. <https://doi.org/10.1103/revmodphys.61.605>.
- (25) Feng, T.; Zhou, H.; Cheng, Z.; Leighann Sarah Larkin; Neupane, M. R. A Critical Review of Thermal Boundary Conductance across Wide and Ultrawide Bandgap Semiconductor Interfaces. *ACS applied materials & interfaces* **2023**, *15* (25), 29655–29673. <https://doi.org/10.1021/acsami.3c02507>.
- (26) Kargar, F.; Debnath, B.; Kakko, J.-P.; Säynätjoki, A.; Lipsanen, H.; Nika, D. L.; Lake, R. K.; Balandin, A. A. Direct Observation of Confined Acoustic Phonon Polarization Branches in Free-Standing Semiconductor Nanowires. *Nature Communications* **2016**, *7* (1). <https://doi.org/10.1038/ncomms13400>.
- (27) Balandin, A. A.; Nika, D. L. Phononics in Low-Dimensional Materials. *Materials Today* **2012**, *15* (6), 266–275. [https://doi.org/10.1016/s1369-7021\(12\)70117-7](https://doi.org/10.1016/s1369-7021(12)70117-7).
- (28) Morita, M.; Takuma Shiga. Surface Phonons Limit Heat Conduction in Thin Films. *Physical Review B* **2021**, *103* (19). <https://doi.org/10.1103/physrevb.103.195418>.
- (29) Qi, R.; Shi, R.; Li, Y.; Sun, Y.; Wu, M.; Li, N.; Du, J.; Liu, K.; Chen, C.; Chen, J.; Wang, F.; Yu, D.; Wang, E.-G.; Gao, P. Measuring Phonon Dispersion at an Interface. *Nature* **2021**, *599* (7885), 399–403. <https://doi.org/10.1038/s41586-021-03971-9>.
- (30) Chen, G. *Nanoscale Energy Transport and Conversion: A Parallel Treatment of Electrons, Molecules, Phonons, and Photons*; Oxford University Press, 2005.
- (31) Cheng, Z.; Li, R.; Yan, X.; Jernigan, G.; Shi, J.; Liao, M. E.; Hines, N. J.; Gadre, C. A.; Idrobo, J. C.; Lee, E.; Hobart, K. D.; Goorsky, M. S.; Pan, X.; Luo, T.; Graham, S. Experimental Observation of Localized Interfacial Phonon Modes. *Nature Communications* **2021**, *12* (1), 6901. <https://doi.org/10.1038/s41467-021-27250-3>.
- (32) Kargar, F.; Balandin, A. A. Advances in Brillouin–Mandelstam Light-Scattering Spectroscopy. *Nature Photonics* **2021**, *15* (10), 720–731. <https://doi.org/10.1038/s41566-021-00836-5>.
- (33) Sandercock, J. R. Trends in Brillouin Scattering: Studies of Opaque Materials Supported Films and Central Modes. **1982**, 173–206. https://doi.org/10.1007/3540115137_6.
- (34) Mutti, P.; Bottani, C. E.; G. Ghislotti; M. Beghi; Briggs, D.; Sandercock, J. R. Surface Brillouin Scattering—Extending Surface Wave Measurements to 20 GHz. *Springer eBooks* **1995**, *1*, 249–300. https://doi.org/10.1007/978-1-4615-1873-0_7.
- (35) Ebrahim Nataj, Z.; Xu, Y.; Wright, D.; Brown, J. O.; Garg, J.; Chen, X.; Kargar, F.; Balandin, A. A. Cryogenic Characteristics of Graphene Composites—Evolution from Thermal Conductors to Thermal Insulators. *Nature Communications* **2023**, *14* (1). <https://doi.org/10.1038/s41467-023-38508-3>.

- (36) Vishwakarma, S.; Brown, J. M.; Patel, A.; McCartney, M. R.; Nemanich, R. J.; Smith, D. J. Growth and Characterization of Boron Nitride/Diamond Heterostructures. *Microscopy and Microanalysis* **2022**, *28* (S1), 2830–2831. <https://doi.org/10.1017/s1431927622010662>.
- (37) Guzman, E.; Kargar, F.; Angeles, F.; Meidanshahi, R. V.; Grotjohn, T.; Hardy, A.; Muehle, M.; Wilson, R. B.; Goodnick, S. M.; Balandin, A. A. Effects of Boron Doping on the Bulk and Surface Acoustic Phonons in Single-Crystal Diamond. *ACS Applied Materials & Interfaces* **2022**, *14* (37), 42223–42231. <https://doi.org/10.1021/acsami.2c10879>.
- (38) Praver, S.; Nemanich, R. J. Raman Spectroscopy of Diamond and Doped Diamond. *Philosophical Transactions of the Royal Society of London. Series A: Mathematical, Physical and Engineering Sciences* **2004**, *362* (1824), 2537–2565. <https://doi.org/10.1098/rsta.2004.1451>.
- (39) Mortet, V.; Vlčková Živcová, Z.; Taylor, A.; Davydova, M.; Frank, O.; Hubík, P.; Lörinčík, J.; M. Aleshin. Determination of Atomic Boron Concentration in Heavily Boron-Doped Diamond by Raman Spectroscopy. *Diamond and Related Materials* **2019**, *93*, 54–58. <https://doi.org/10.1016/j.diamond.2019.01.028>.
- (40) Mortet, V.; Gregora, I.; Taylor, A.; Lambert, N.; Ashcheulov, P.; Gedeonova, Z.; Hubik, P. New Perspectives for Heavily Boron-Doped Diamond Raman Spectrum Analysis. *Carbon* **2020**, *168*, 319–327. <https://doi.org/10.1016/j.carbon.2020.06.075>.
- (41) Mermoux, M.; Marcus, B.; Swain, G. M.; Butler, J. E. A Confocal Raman Imaging Study of an Optically Transparent Boron-Doped Diamond Electrode. *The Journal of Physical Chemistry. B* **2002**, *106* (42), 10816–10827. <https://doi.org/10.1021/jp0202946>.
- (42) Crisci, A.; Mermoux, M.; Saubat-Marcus, B. Deep Ultra-Violet Raman Imaging of CVD Boron-Doped and Non-Doped Diamond Films. *Diamond and Related Materials* **2008**, *17* (7-10), 1207–1211. <https://doi.org/10.1016/j.diamond.2008.01.025>.
- (43) Nemanich, R. J.; Solin, S. A.; Martin, R. M. Light Scattering Study of Boron Nitride Microcrystals. *Physical Review* **1981**, *23* (12), 6348–6356. <https://doi.org/10.1103/physrevb.23.6348>.
- (44) Gorbachev, R. V.; Riaz, I.; Nair, R. R.; Jalil, R.; Britnell, L.; Belle, B. D.; Hill, E. W.; Novoselov, K. S.; Watanabe, K.; Taniguchi, T.; Geim, A. K.; Blake, P. Hunting for Monolayer Boron Nitride: Optical and Raman Signatures. *Small* **2011**, *7* (4), 465–468. <https://doi.org/10.1002/sml.201001628>.
- (45) Reich, S.; Ferrari, A. C.; Arenal, R.; Loiseau, A.; Bello, I.; Robertson, J. Resonant Raman Scattering in Cubic and Hexagonal Boron Nitride. *Physical Review B* **2005**, *71* (20). <https://doi.org/10.1103/physrevb.71.205201>.
- (46) Kutsay, O.; Yan, C.; Chong, Y. M.; Ye, Q.; Bello, I.; Zhang, W. J.; Zapien, J. A.; Zhou, Z. F.; Li, Y. K.; Garashchenko, V.; Gontar, A. G.; Novikov, N. V.; Lee, S. T. Studying Cubic Boron Nitride by Raman and Infrared Spectroscopies. *Diamond and Related Materials* **2010**, *19* (7-9), 968–971. <https://doi.org/10.1016/j.diamond.2010.02.033>.

- (47) Luo, K.; Zhang, Y.; Yu, D.; Li, B.; Hu, W.; Liu, Y.; Gao, Y.; Wen, B.; Nie, A.; Zhao, Z.; Xu, B.; Zhou, X.-F.; Tian, Y.; He, J. Small Onion-like BN Leads to Ultrafine-Twinned Cubic BN. *Science China Materials* **2019**, *62* (8), 1169–1176. <https://doi.org/10.1007/s40843-019-9409-1>.
- (48) Eremets, M. I.; Gauthier, M.; Polian, A.; Chervin, J. C.; Besson, J. M.; Dubitskii, G. A.; Semenova, Y. Y. Optical Properties of Cubic Boron Nitride. *Physical review. B, Condensed matter* **1995**, *52* (12), 8854–8863. <https://doi.org/10.1103/physrevb.52.8854>.
- (49) Stenzel, O.; Hahn, J.; Roder, M.; Ehrlich, A.; Prause, S.; Richter, F. The Optical Constants of Cubic and Hexagonal Boron Nitride Thin Films and Their Relation to the Bulk Optical Constants. *Physica Status Solidi A* **1996**, *158* (1), 281–287. <https://doi.org/10.1002/pssa.2211580130>.
- (50) Jiang, X.; Harzer, J. V.; Hillebrands, B.; Wild, Ch.; Koidl, P. Brillouin Light Scattering on Chemical-Vapor-Deposited Polycrystalline Diamond: Evaluation of the Elastic Moduli. *Applied Physics Letters* **1991**, *59* (9), 1055–1057. <https://doi.org/10.1063/1.106343>.
- (51) R. J. Jiménez Riobóo; Lluís Artús; R. Cuscó; Taniguchi, T.; Guillaume Cassabois; Gil, B. In- and Out-of-Plane Longitudinal Acoustic-Wave Velocities and Elastic Moduli in *H*-BN from Brillouin Scattering Measurements. *Applied Physics Letters* **2018**, *112* (5). <https://doi.org/10.1063/1.5019629>.
- (52) Carlotti, G. Elastic Characterization of Transparent and Opaque Films, Multilayers and Acoustic Resonators by Surface Brillouin Scattering: A Review. *Applied sciences* **2018**, *8* (1), 124–124. <https://doi.org/10.3390/app8010124>.
- (53) Farnell, G. W.; Adler, E. L. Elastic Wave Propagation in Thin Layers. *Physical Acoustics* **1972**, *9*, 35–127. <https://doi.org/10.1016/b978-0-12-395670-5.50007-6>.
- (54) Du, J.; Tittmann, B. R.; Ju, H. S. Evaluation of Film Adhesion to Substrates by Means of Surface Acoustic Wave Dispersion. *Thin Solid Films* **2010**, *518* (20), 5786–5795. <https://doi.org/10.1016/j.tsf.2010.05.086>.
- (55) Xia, H.; Cheng, G. X.; Liu, G. G.; Zhang, W.; Chen, K. J.; Zhang, X. K. Brillouin Scattering Study of Interface Constituents in A-Si:H/A-SiNx:H Superlattices. *Solid State Communications* **1990**, *73* (9), 657–660. [https://doi.org/10.1016/0038-1098\(90\)90257-c](https://doi.org/10.1016/0038-1098(90)90257-c).

CHAPTER 4 – CONCLUSION

In the first work, I reported the results of the investigation of bulk and surface acoustic phonons in the undoped and boron-doped single-crystal diamond films using the Brillouin-Mandelstam light scattering spectroscopy. The evolution of the optical phonons in the same set of samples was monitored with Raman spectroscopy. It was found that the frequency and the group velocity of acoustic phonons decrease non-monotonically with the increasing boron doping concentration, revealing pronounced phonon softening. The change in the velocity of the shear horizontal and the high-frequency pseudo-longitudinal acoustic phonons in the degenerately doped diamond, as compared to the undoped diamond, was as large as $\sim 15\%$ and $\sim 12\%$, respectively. As a result of boron doping, the velocity of the bulk longitudinal and transverse acoustic phonons decreased correspondingly. The frequency of the optical phonons was unaffected at low boron concentration but experienced a strong decrease at the high doping level. The density-functional-theory calculations performed by Reza Meidanshahi in the Stephen Goodnick group at Arizona State University of the phonon band structure for the pristine and highly-doped sample confirm the phonon softening as a result of boron doping in diamond. The obtained results have important implications for thermal transport in heavily doped diamond, which is a promising material for ultra-wide-band-gap electronics.

In the second work, I reported an investigation of the bulk optical, bulk acoustic, and surface acoustic phonons in thin films of turbostratic boron nitride (*t*-BN) and cubic boron

nitride (*c*-BN) grown on B-doped polycrystalline and single-crystalline diamond (001) and (111) substrates. The characteristics of different types of phonons were determined using Raman and Brillouin-Mandelstam light scattering spectroscopies. The atomic structure of the films was determined using high-resolution transmission electron microscopy (HRTEM) which were taken by Saurabh Vishwakarma in the David Smith group at Arizona State University and correlated with the Raman and Brillouin-Mandelstam spectroscopy data. The HRTEM analysis revealed that the cubic boron nitride thin films consisted of a mixture of *c*-BN and *t*-BN phases, with *c*-BN being the dominant phase.

It was found that while visible Raman spectroscopy provided information for characterizing the *t*-BN phase, it faced challenges in differentiating the *c*-BN phase either due to the presence of high-density defects or the overlapping of the Raman features with those from the B-doped diamond substrates. In contrast, Brillouin-Mandelstam spectroscopy clearly distinguishes the bulk longitudinal and surface acoustic phonons of the *c*-BN thin films grown on diamond substrates. Additionally, the angle-dependent surface Brillouin-Mandelstam scattering data show the peaks associated with the Rayleigh surface acoustic waves, which have higher phase velocities in *c*-BN films on diamond (111) substrates. These findings provide valuable insights into the phonon characteristics of the *c*-BN and diamond interfaces and have important implications for the thermal management of electronic devices based on ultra-wide-band-gap materials.